1-1-2010

Solid particle erosion of materials for use in gas pipeline control valves

Ehsan Akbarzadeh
Ryerson University

SOLID PARTICLE EROSION OF MATERIALS FOR USE IN GAS PIPELINE CONTROL VALVES

By

Ehsan Akbarzadeh

B.Eng., Azad University, 2005

A Thesis

Presented to Ryerson University

In partial fulfillment of the requirement for the degree of

Master of Applied Science

In the program of

Mechanical Engineering

Toronto, Ontario, Canada, 2010

AUTHOR'S DECLARATION

I hereby declare that I am the sole author of this thesis report.

I authorize Ryerson University to lend this thesis to other institutions or individuals for the purpose of scholarly research.

I further authorize Ryerson University to reproduce this project by photocopying or by other means, in total or in part, at the request of other institutions or individuals for the purpose of scholarly research.

Ehsan Akbarzadeh
Department of Mechanical Engineering
Ryerson University

ABSTRACT

Solid Particle Erosion of Materials for Use in Gas Pipeline Control Valves

Ehsan Akbarzadeh, Master of Applied Science, 2010

Department of Mechanical Engineering, Ryerson University

To aid in the materials selection of gas control valves, the solid particle erosion behaviour of twelve metals was investigated using impinging jets of magnetite particles. The erosion rates were measured for two different particle sizes, two different velocities, and six different impingement angles. Scanning electron micrography and EDX (Energy Dispersive X-ray analysis) mapping was used to investigate the erosion mechanisms and the extent of particle embedding. There was no measurable erosion for the Tungsten Carbide samples, even for very long exposure times. For nickel plated steel, the plating was found to delaminate, resulting in a brittle erosive response. For all other tested materials, the measured erosion rates and scanning electron micrographs indicated a ductile erosion mechanism under all conditions considered. The erosion rates were found to fit a semi-empirical erosion model due to Oka et al. [1] well. The most erosion resistant materials were found to be the Solid tungsten carbide (WC) and Solid Stellite 12 and the least erosion resistant materials were A1018 carbon steel nickel plated and A240 Type 410 stainless steel plate.

With all other conditions being equal, a larger erosion rate was measured when utilizing the smaller particles, than when the large particles were used. This counter-intuitive result was demonstrated to be due to a combination of effects, including the formation of thicker hardened layer more embedded particles, and more particle fragmentation when utilizing the larger particles.

ACKNOWLEDGMENTS

I would like to sincerely thank my research supervisors Dr. M. Papini and Dr. J. K. Spelt, for their outstanding supervision and guidance. Their unconditional support, advice and constructive criticism throughout my studies have been invaluable.

The author would like to sincerely thank Dr. Ehab Elsaadawy and Dr. Abdelmounam Sherik from ARAMCO for their helpful assistance, guidance and encouragement throughout the completion of this thesis.

I would like to thank Dr. Greg Kawall, Director of Mechanical Engineering Graduate program, all the faculty members, technical officers and administrative staff members for their kind support and cooperation during my stay at Ryerson University.

I am also grateful to my mother Parvin and my father Asghar for their continued support, prayers and love. Deepest gratitude to my wife Ghazal who had to sacrifice her time and needs to support me to finish my studies successfully.

Finally, I am grateful to the Grace of God for the countless blessings I have received.

TABLE OF CONTENTS

LIST OF FIGURES

LIST OF TABLES

NOMENCLATURE

C	Erosion constant
d	Nozzle diameter
D	Standoff distance
E	Volumetric erosion rate (mm^3.g)
P	Air pressure
RMS	Root mean square
t	Blasting time
V	Target volume removed
v	Volume of crater on eroded material
α	Angle of impact
ρ	Density
d_p	Particle diameter
ξ_{90}	Erosion rate at normal impact angle
n1	Cutting exponent
n2	Repeated deforming exponent
n3	Velocity exponent
$\dot{m}$	Mass flow rate ($g.min^{-1}$)
m_t	Mass of target material removed
m_p	Mass of particles used
Rq	Surface roughness
A_{face}	Area of cell face used in CFD modeling

CHAPTER 1

INTRODUCTION

1.1 MOTIVATION

The damage due to the impact of particulates contained in the gas flow onto the internal surface of control valves is a very important problem in the gas pipeline industry. The predominant contaminant in natural gas transfer pipelines, gas compressor equipment, refineries, and gas storage reservoirs, is known as 'black powder'. Huge costs in money and time result from effects associated with the entrainment of black powder in the gas flow. For example, unplanned shutdowns can occur due to the clogging of instrumentation, the lowering of the efficiency of compressors [2-6], and the failure of control valves due to solid particle erosion, which is the problem addressed in the present work. Chemical analysis of black powder collected from gas pipelines at Saudi Aramco has revealed that it is mainly made up from iron oxides and a smaller amount of iron carbonates [7]. From the solid particle erosion point of view, the particulate iron oxides are likely the most aggressive material in black powder, owing to their high hardness.

A clear understanding of the relationship between the erosion rate of the materials used in control valves, their mechanical properties, and the process conditions such as erosive particle size, shape, velocity, angle of impact, and spatial distribution is required for an improved and cost effective materials selection for control valves.

1.2 OBJECTIVES

The ultimate objective of this thesis is to determine the solid particle erosion behaviour of a number of candidate materials which could be used in gas pipeline control valves in response to particulates and process condition similar to those found in gas pipelines. This will not only allow improved materials selection for the control valve materials, but also provide needed input data for future computational fluid dynamics simulations of eroded profiles. The work will be conducted in collaboration with an industrial partner having significant experience in this area. To achieve the ultimate objective, the following secondary objectives will be met:

- Design and construction of an experimental setup capable of measuring the solid particle erosion rate (volume of material removed per unit mass of blasted particle) of a number of different target materials in response to the impact of a jet of iron oxide (magnetite) particles.
- The sourcing and purchase of the twelve candidate materials, some of which are fairly rare metals, which require post processing to meet the specifications required by the industrial partner.
- The sourcing and purchase of magnetite erodent powder which is sufficiently similar in purity and size to what exists in the black powder found in gas pipelines.
- Conducting of erosion rate experiments for 12 candidate target materials suggested by the industrial partner, for two different particles size distributions, at six angles of attack, and at two different particle velocities. The tests will be based on ASTM standard G76-07 [8].

- Surface analysis and numerical curve fitting of the measured erosion rates to well-known erosion models, allowing for the identification of dominant erosion mechanisms.

1.3 THESIS OUTLINE

The thesis will be presented as follows:

- Chapter 2 reviews the relevant literature regarding the mechanisms leading to the erosion of the surface due to the impact of solid particles, and the different approaches to model these mechanisms.
- Chapter 3 describes the experimental apparatus, the preparation of the powder, and the experimental procedure.
- Chapter 4 explains the methodology for curve fitting of the measured erosion rates to a well known erosion model
- Chapter 5 reports the erosion rate results of the various experimental conditions, and evaluates and discusses the fit of the experimental data with the erosion model.
- Chapter 6 describes an investigation of the unusual particle size effect found in the erosion rate tests, and the dominant erosion mechanisms of the different materials.
- Chapter 7 presents the conclusions and discusses possible future work.

CHAPTER 2

LITERATURE REVIEW

This chapter will present literature review related to formation, characteristic and movement of the black powder in gas pipelines. It also includes details regarding the solid particle erosion mechanism and parameters involved in erosion.

2.1 BLACK POWDER

2.1.1 FORMATION AND CHARACTERISTICS OF BLACK POWDER

A chemical reaction between the pipeline material and contaminates results in the existence of black powder in the form of a very fine powder or a wet tar. After the reaction occurs, the probability of eliminating this powder is very low [9]; however, under normal conditions, a gas pipeline is under minimal corrosion risk [2]. Black powder originates in gas pipeline from mixture of sand, mill scale, several molecular and crystalline structures of iron and sulphur [6]. These are made from the corrosion of the wall of steel pipelines if the corrosive agent is present [2-6]. Condensed moisture, containing carbon dioxide (CO_2), oxygen (O_2), and hydrogen sulphide (H_2S) is considered the most corrosive initiator. Natural gas contains carbon dioxide, but oxygen can penetrate from leaks at places under low pressure in the pipeline system [2]. The amount of gaseous H_2S, CO_2 and O_2 in pipelines together with the presence of water causes significant internal corrosion and forms FeS and $FeCO_3$. These can be further converted to Fe_3O_4 in the presence of oxygen. Most of the transmission pipeline companies allow only a limited amount of oxygen inside their flow due to its very high corrosion and combustion

potential. Hydrogen Sulphide is found in natural gas or it can be made from a chemical reaction with anaerobic bacteria (SRBs).

Other contaminants that can be found in gas pipelines are water, liquid hydrocarbons, salts, chlorides, sulphates, sand, rouge, asphaltenes, and weld spatter. From the erosion point of view, iron oxides, such as magnetite are of importance, due to their relatively high hardness. Figure [2.1] shows images of magnetite having a 100 μm average particle size or smaller.

Direct oxidation of the wall of steel pipeline due to the existence of dissolved oxygen in wet-dry cylinder is the main source of iron oxide [2] according to:

$$Fe + H_2O + 1/2O_2 \rightarrow Fe(OH)_2 \quad (2.1)$$

$$2Fe(OH)_2 + 1/2O_2 + H_2O \rightarrow 2Fe(OH)_3 \quad (2.2)$$

In gas pipelines, magnetite is formed due to the instability of *Fe (OH)* in the presence of Fe and low concentrations of dissolved oxygen:

$$8FeO(OH) + Fe \rightarrow 3Fe_3O_4 + 4H_2O \quad (2.3)$$

The Fe_2O_3 also could form if the water is nearly saturated with dissolved oxygen. Other forms of iron oxide could form alternatively due to microbiologically induced corrosion (MIC) resulting from acid producing bacteria (APB) or iron oxidizing bacteria (IOB).

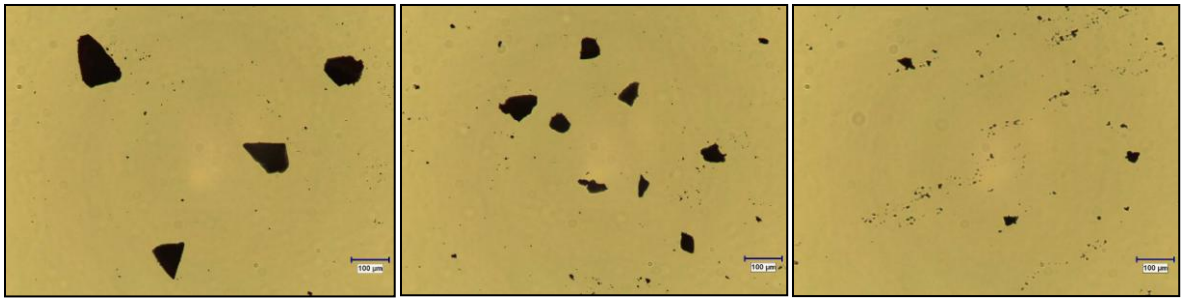

(a) (b) (c)

Figure 2- 1: Magnetite samples: (a) as received, (b) passing through 230 mesh and (c) passing through 325 mesh. Scale bar is 100 µm

2.1.2 BLACK POWDER MOVEMENT IN GAS PIPELINES

The particle flow in a gas pipeline depends on the gas velocity. The solid particle velocity depends on pipeline diameter, gas pressure, density, viscosity, and particle size [10]. The nature of particle motion depends on its shape and gravity. Only flow rate reduction or gas compression can stop particle movement in the flow. Continuous particle shattering due to inter-particle collisions makes their flow easier and hard to trap. For instance Keska [11] described the different forms of particle movement for different particle shapes; e.g., the long thin particles slide, the round particles roll, the flake-like particles fly like the movement of leaves in the wind, and the irregular shaped particles move in a combination of all above particle motions. In case of wet black powder deposition, pigging could be an initiative for powder movement. Deposition of black powder could lead to the blockage of a pipeline if the particle velocity is not high enough.

A minimum amount of drag force from the gas velocity transfers to the particle, causing it to fly [10]. Other sources of force, as proposed by Smarts [12], are gravity and buoyancy, which are constant, while lift and drag vary with flow and gas conditions. The black powder settles at the bottom of the pipeline to form a sediment layer if these movement motivators are

not adequate. The sediment layer will grow and act as a barrier for gas flow until the minimum velocity to cause movement of the particle along in the pipe is reached.

2.2 SOLID PARTICLE EROSION IN INDUSTRY

Erosion can be defined as "an abrasive wear process in which the repeated impact of small particles entrained in a moving fluid against a surface result in the removal of material from that surface" [13]. The erosion rate is defined as mass or volume of target material removed per mass of particles impacting the surface. Solid particle phenomena are associated with both constructive and destructive processes in industry. Examples of constructive applications include abrasive jet micro-machining of micro-fluidic components [14], abrasive jet machining [15], and blast cleaning [16-17]. On the other hand, the destructive effects of solid particle erosion are seen in the damage done to oil and gas transmission pipelines, in production facilities [18-20], in the erosion of turbine blades in power generation systems [21], in foreign object damage in the jet engine [22], and the erosion of heat exchangers in fluidized bed combustors [23].

In general, there are three well known scientific research methodologies for exploring and predicting the effects or equations relevant to erosion phenomena. The most common investigation method is to conduct several experimental erosion tests under specific and controlled conditions. Another method is developing numerical models to derive equations for predicting erosion rate or residual stress for various materials with different properties or for various impact conditions. The third method is to utilize computer simulations to model the erosion test conditions virtually.

2.3 EROSION DUE TO SINGLE PARTICLE IMPACT

The complexity of the erosion mechanism for a jet containing many particles has required research to focus on single particle investigation as a first step. Study of the fundamental material removal mechanisms evident in single particle impact has led to a number of erosion theories, which have been generalized for the multi-particle impact case. In constructing erosion models, researchers were able to make contributions to: (1) the understanding of the fundamental mechanisms of material loss due to erosion (cracking, ploughing, cutting etc.) [24-26] , (2) the understanding of the particle trajectory before and after impact, (3) the understanding of the particle flow conditions such as a flux effect, and (4) investigating effect of erosion process parameters in detail and generalizing them to multi-particle impact [1]. Single particle impact studies utilizing angular particles have shown that the dominant mechanism of erosion is cutting at shallow angles, and ploughing at higher angles of impact [1], [25-29]. In contrast, erosion due to spherical particles is dominated by ploughing at the both shallow and normal impacts, but Hutchings [28] mentioned that a critical particle velocity is required.

2.4 EROSION DUE TO MULTI-PARTICLE IMPACT

For multi-particle impacts due to a stream of flowing particles, the surface roughness of the target material plays a key role after early impacts, and this factor can have an effect on the generation of different erosion mechanisms [29]. The main issues preventing the accurate prediction of the erosion mechanisms are the high rate of collisions between particles either by other surrounding particles in the air flow, or between the incident and rebounding particles. Unlike a single particle for which the particle trajectory is predictable, for multiple particle flows, the particles in a jet strike the surface at a variety of incident angles. This is because the

particles entrained in the carrier gas form a cone shape jet after release from the nozzle [30]. This causes complications, for example, in specifying a particular desired impact angle at which the erosion rate might be measured.

2.5 SOLID PARTICLE EROSION MECHANISMS

A clear understanding of the relationship between the erosion rate of the materials, and the process conditions such as particle size, shape, properties, velocity, angle of impact, and their spatial distribution, and target properties is required for developing predictive equations for the mass of removed materials impacted by a stream of particles. Many researchers, e.g., [1], [31-33], have provided erosion models which result in predictive equations. Solid particle erosion has generally been classified into two distinct classes of behavior, for which erosion mechanism have been identified and modeled: brittle erosive, and ductile erosive systems.

In brittle erosion, the material is mostly removed by cracking and chip formation, and the maximum erosion occurs at a 90˚ impact angle (i.e. particles incident perpendicular to surface) [34]. Ductile erosion, on the other hand, is characterized by material removed due to a ploughing and cutting mechanism, and the maximum erosion occurs at a shallow (approximately 30˚) angle of impact. Since the large majority of the materials considered in the present work erode in a ductile manner, only ductile erosion will be considered in detail in this literature review.

2.6 MATERIAL REMOVAL MECHANISMS FOR DUCTILE EROSION

Forging and extrusion are the dominant mechanisms of material removal for ductile erosive systems. Material is first extruded the lips adjacent to the impact craters by the first series

of impacting particles. It is thought that these lips are forged by subsequent particle impacts. This mechanism of material removal is referred to as a 'platelet mechanism' for multi-particle impacts [35-36]. Particles hit the target continuously, so after these platelets cover all of the impact surface area, a stable stage of material removal (steady state erosion) occurs. Material removal occurs due to the high rate of plastic deformation that causes the material to be loosened leading to fractures by subsequent particle impacts.

Heat is generated when the particles impact the surface, due to friction. The heat transfer condition during the multi-impact process is basically adiabatic [37], due to very small area of contact between particle and target material and the very rapid transfer of the localized shear force from particle [38]. As an example, the work softening phenomenon occurs due to higher temperature imposed by the highly concentrated plastic deformation at the surface [39]. Because the heat generated due to the localized plastic deformation arising from a single impact can be significant, local melting [40] and work softening [41] may occur on the target surface.

To model material removal, a cutting model was proposed by Finnie [42]. Bitter introduced the deformation wear to Finnie's model but only for normal impact [43-44]. Hutchings modified Finnie's model later by using shape factor adjustment [45]. The effect of lip formation was reported in many experiments, and Christman and Shewmon studied the effect of strain hardening changes due to a large temperature gradient [46].

2.6.1 EFFECT OF PARTICLE SHAPE ON SOLID PARTICLE EROSION

Most of the previous development of analytical and numerical erosion models focused on particles with a spherical shape. For example, Bitter [43], in his predictive model, assumed that a

spherically shaped particle has a radius equal to the radius of curvature of the rounded edges of a small non-spherical particle. Hutchings [28] tried to compare the erosion rate of sand with flat-faced angular surfaces with particle having the spherical rounded surface. Investigation of the impacted surface in the work of Bitter and Hutchings showed a similar surface deformation, regardless of particle shape. In contrast, it has been found experimentally that there is a huge difference in the measured erosion rate between angular and spherical particles having a similar particle size [47] and impact angle [48].

Different particle characterization techniques have been developed to investigate the particle shape importance on erosion models [49-50]. For instance, the shape of particles can be easily compared by using photographic techniques, and this technique is one of the well-known procedures for distinguishing shape factors [51]. The deviation of an irregular particle from a known geometry like sphere or square particle shape is another commonly used technique to define particles shape, as is using the ratio of the perimeter to area of the particle [50].

2.6.2 EFFECT OF PARTICLE SIZE ON EROSION

Comparison of the erosion rate of materials using different particle sizes under the same experimental conditions (same mass of uniformly shaped erodent) can provide evidence of the particle size effects on the erosion mechanism. Variations in particle size can affect the geometric parameters of erosion such as particle shape, chip size, and crater volume. The more massive the particles, the higher the kinetic energy they carry, assuming an equal density and velocity. Many have reported that a higher erosion rate results when using a larger particle size, due to the higher energy transfer during the impact from particle to target material. Most of the ductile erosion models have focused on the effect of mass and velocity separately [42], [52].

They assumed the plastic deformation or target material removal occurred due do the energy transferred by mass and velocity of particles. They conducted theoretical analyses of the erosion for a number of steels in various heat-treated conditions. The specific erosion energies were calculated as the kinetic energy of the impinging particles per unit volume of metal removed.

For single particle impacts, Hutchings et al. [28] studied the effect of scaling. He found that pattern of deformation does not depend on the particle size, when they are in the range of 1 micrometer to 3 mm in diameter.

Dundar et. al. [53], reported a significant difference in plastic deformation of the target material of Cu–30% Zn and pure Ti when impacted with spherical particles varying in size from 2 to 25 μm, however, when using angular particles with similar size ranges, they did not find any change in deformation. They found both from, the absence of apparent slip in surface impacted by angular particles and formation of the smaller slips by sphere erodent particles, the total damage of erosion reduced.

Several other experiments using an air blaster for particle sizes ranging from 50 to 430 μm have confirmed the dependency of erosion rates on particle size [1], and others have found that, for particle sizes less than 100 μm in diameter, a significant reduction in erosion rate occurs due to more rapid energy dissipation [54].

An effect of particle size on surface properties such as the formation of a work hardened layer has also been found. Finnie et al. [52] reported the formation of a work hardened layer with a thickness range between 50 and 100 μm depending on the gold and silicon carbide particle size

on aluminum and copper, respectively. A micro-hardness test on the blasted surface confirmed the existence of a thicker hardened layer in the case of the larger particles.

2.6.3 EFFECTS OF PARTICLE VELOCITY ON EROSION

Particle velocity has a very large influence on the measured erosion rate of a material. In general, the higher the particle velocity, the higher is the expected erosion rate. The work of Stevenson and Hutchings [55], who found a good correlation between particle velocity, blasting pressure, and resulting erosion rate is of particular use. Most researchers use a power law to describe the effect of velocity on erosion rate, i.e. ($E \propto V^3$) in their erosion models. The velocity exponent (n_3) can vary in the range between 1.5 to 3 [56-57], depending on the target material, and the erodent particles.

2.6.4 EFFECT OF PARTICLE TRAJECTORY ON EROSION

The impact angle is defined as the angle between the trajectory of the particle and the target surface. Ductile metals usually exhibit a ductile erosion mechanism where the material removal rate reaches a maximum for impact angles from 15˚ to 30˚, and decreases by a factor of 2 to 3 at a normal (i.e. 90˚) impact angle [58]. A detailed study on material removal by particle impacts at normal incidence confirmed that material removal occurs because of overlapping craters on the substrate [59]. In this normal incidence case, for both angular and spherical particles, the formation and subsequent detachment of the platelets was the main mechanism of material removal. At shallow angles, a more efficient cutting and ploughing mechanism can occur, resulting in a significantly higher erosion rate.

A higher rate of particle fragmentation can also occur at normal impact when energy transfers normal to the surface are maximized, compared to at other angles. For friable erodent materials, this can further decrease the expected erosion rate at normal incidence, as much energy that could be used to damage the target is instead wasted in particle fracture energy.

Because the particle has a dynamic motion and velocity less than or equal to the flow velocity, computational-fluid-dynamics (CFD) based erosion models are usually used to simulate the particle trajectory. The CFD erosion model is constructed from three primary steps; 1) flow modeling using the fluid mechanics equations 2) particle tracking 3) applying empirical erosion equations [60].

2.6.5 MATERIAL HARDNESS AND EROSION

Hardness is measured as an average flow stress that is applied to an indenter during an indentation test; it is the resistance of the material to plastic deformation. Target material hardness is the mechanical property that has received the most attention by researchers studying solid particle erosion [61]. For example, in the experiment of [62], the hardness ratio (the ratio of the particle hardness to target hardness) was used to justify the same erosion rate values that were captured for different materials, e.g. glass, alumina, WC-7% Co and 304 stainless steel. However, in most other erosion models, the particles are assumed rigid, since their hardness value is much greater than the hardness of the target material. For example, an erosion model due to Oka et al.[1] uses the material hardness value to calculate the erosion rate for various testing conditions, without considering the particle hardness.

Three distinguishable hardness regimes have been observed beneath the eroded surface of the ductile materials. In order, from the top blasted surface through the bulk target material: 1) the platelet zone or soft surface zone, 2) Work hardened zone, 3) Unaffected zone or bulk material zone. Levy [63] also confirmed the existence of the area under the blasted surface of the target, which is formed as a result of the extensive plastic deformation, and which is the 'work-hardening region'. This region showed some elevation in temperature during impact resulting in some work hardening under the heated area. The investigation of the blasted substrate showed the hardness value graduation for the three zones. The hardness gradually increased from the subsurface to the work-hardened zone, and decreased from the work hardened zone to the base metal. The existence of a hardened layer can also act as an initiative for transferring a ductile erosion mechanism to a brittle mechanism [43].

2.6.6 PARTICLE FLUX RATE AND EROSION

A variation in particle flux can affect the solid particle erosion behavior by changing the collision rate between particles and surface, as well as the degree of interaction between rebounding particles and incident particles. Hutchings [64] determined the optimum particle flux value through erosion testing. Tilly [58] found an analytical expression for the optimum flux where particle collisions are negligible. The importance of particle flux rate in erosion has shown significant effect on simulation model for developing AJM (abrasive jet micro machining) profiles by Shafiei [65]. Her model introduced the particle flux effect on erosion by the tracking of individual particles, performing inter-particle and particle to surface collision detection, and implementing collision kinematics. In other effort Burzynski and Papini [66] proposed an analytical model that can be used to estimate interference effects at high flux, and to obtain the

critical flux below which a given level of particle interference will occur in a solid particle erosion test. Another effort by Ciampini et al. [67-68] used a computer model that was capable of examining the effect of the following parameters on the severity and frequency of inter-particle collisions: stream angle of incidence, nozzle divergence angle, incident particle velocity and flux, particle size, particle–particle and particle–surface impact parameters, and stand-off distance.

CHAPTER 3

EXPERIMENTAL APPARATUS AND PROCEDURE

This chapter describes the experimental apparatus and methodology used to perform the erosion rate testing. It also includes details regarding the target materials, the erodent powder preparation, and the measurement of the particle velocity.

3.1 EROSION TESTING APPARATUS

A photograph of the experimental setup is shown in Figure 3-1, which is also shown schematically in Figure 3-2. Wherever possible, the ASTM standard for erosion testing, ASTM G76-07 [8], was followed.

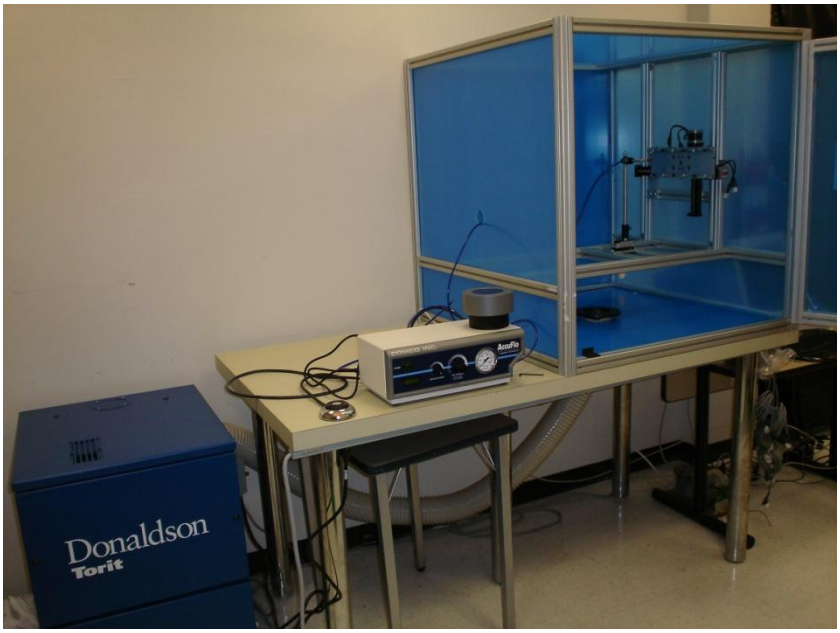

Figure 3- 1: Photograph of experimental setup

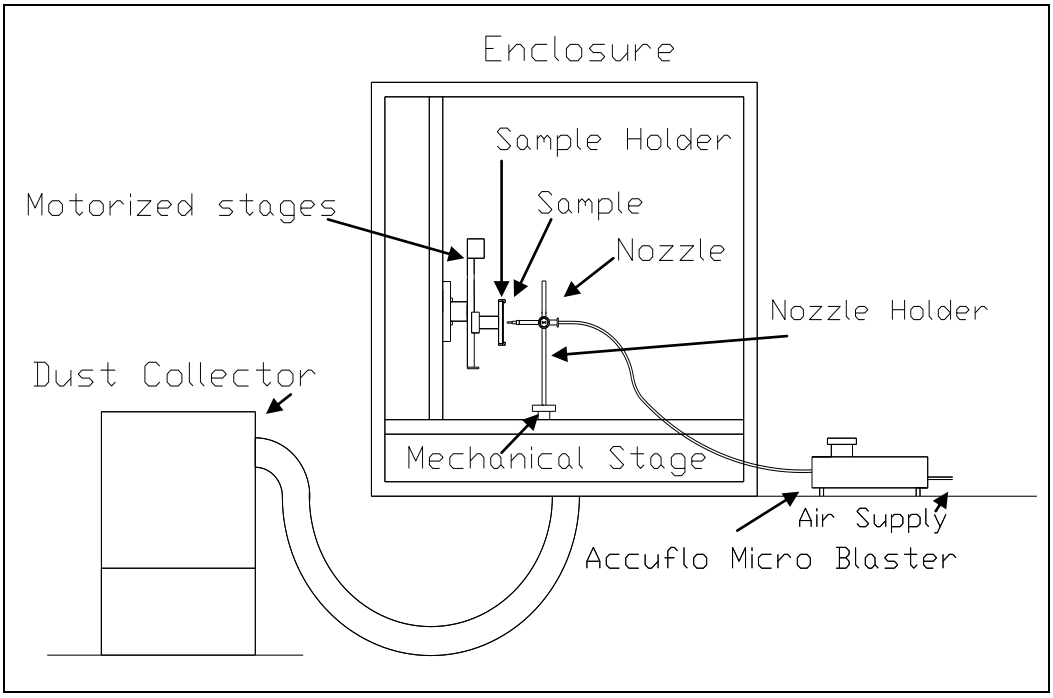

Figure 3- 2: Schematic of experimental setup

3.1.1 MICROBLASTER

An AccuFlo AF10 Micro Blaster manufactured by Comco Inc. (Burbank, CA, USA) was used in all solid particle erosion testing. The AccuFlo incorporates a powder modulator, an aerodynamically designed mixing chamber and a Powder Gate™ valve. These features allow it to have a higher degree of repeatability in abrasive mass flow rate than previous models. A 1.5 mm inner diameter (MB1520-35, Comco Inc.) high performance nozzle was utilized at a nozzle to target standoff distance of 10 mm, based on recommendations in ASTM G76-07 [8].

To maximize the uniformity of the powder flow an electric mixer (Figure 3-3 (a)) having a set of conical and square paddles (Figure 3-3 (b)) was incorporated into the powder reservoir. The shape of the paddles was carefully designed to conform to the powder reservoir shape in the vicinity of the powder orifice at its bottom. The mixer shaft passed through an opening in the pressurized powder reservoir which was sealed by a pressure rated O-ring.

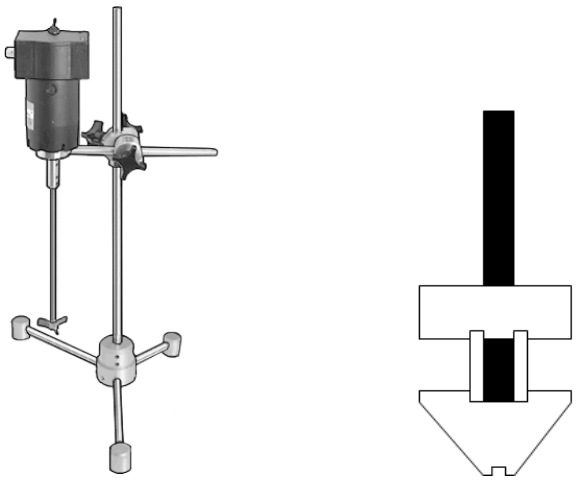

(a) (b)

Figure 3- 3: (a) mixer setup, (b) paddle setup

3.1.2 AIR DRYERS AND SUPPLY

Moisture or oil contamination in the air supply can prevent abrasive powder from flowing freely through the micro-abrasive blasting system; therefore, air dryers are necessary to prevent moisture from causing the nozzle to clog. To ensure a clean air supply, the laboratory air was passed through a refrigeration air dryer, and then a desiccant air dryer/oil prefilter (Model AD5100-4, Comco Inc.). The laboratory ambient air was routinely dehumidified to a maximum of approximately 40% RH.

3.1.3 DUST COLLECTOR

An industrial grade dust collection system was utilized to ensure an appropriate airflow through the work chamber while extracting the spent abrasive and returning clean air to the room. In the utilized system a DC-2000 (Comco Inc., USA), particles are trapped on the outer surface of the filter bags, which can be replaced when needed.

3.1.4 COMPUTER CONTROLLED STAGES

The samples were moved relative to the nozzle in order to automate the machining of three repeat holes per sample, required to evaluate the erosion rate of the candidate materials. A computer controlled two-dimensional motorized positioning stage system from Velmex Inc. (Bloomfield, NY, USA) was used to scan the target samples relative to the stationary nozzle. The samples were clamped to a 100 mm x 300 mm aluminum plate specimen holder that was capable of holding six samples at once. The stages were programmed to allow for machining multiple adjacent holes on each sample automatically. A mechanical positioning stage attached to the nozzle holder was allowed the nozzle-to-target standoff distance to be controlled accurately. The angle of impingement was controlled by rotating the nozzle.

The mechanical stages were protected from the abrasive erodent dust by the use of sealing bellows, and the entire setup was placed in a Plexiglas enclosure having a frame and internal mounting members made from aluminum extrusions. A hinged door allowed access to the setup. The computer, dust collector, AccuFlo, and stage control units were placed outside the enclosure, and the dust collector hose, translational stage wires, and abrasive flow tube were passed through holes in the enclosure wall. Standard laboratory safety protocols with respect to the use of safety glasses and particulate filter breathing masks (3M, model 8233 N100) were followed during all experiments.

3.2 IRON OXIDE POWDER BLASTING MEDIA

Two size distributions of magnetite powder (Fe_3O_4, 95.799% pure) having a Vickers hardness of 600 HV were used in the experiments. 325 (Grade 80) and 120 mesh (Grade 3105)

powders were obtained from Craigmont Mines (Merritt, BC, Canada) and Prince Minerals (New York, NY, USA), respectively. The powders were sieved using a Ro-Tap Test Sieve Shaker (W.S. Tyler Company, St. Catharines, Ontario, Canada) to obtain two different powder log-normal size distributions (Figure 3-4) having nominal spherical mean diameters of 6.9 μm and 30.4 μm. The shaker was capable of 278 oscillations per minute and tapping motions of 150 taps per minute. The powder obtained from Craigmont Mines was found to have significant moisture content, and it was thus dried to a constant mass (precision of 0.1%) in a desiccant filled oven at 110˚ C for 30 to 45 minutes before sieving.

3.2.1 GROSS SAMPLING AND SIEVING METHODOLOGY

The sieves were selected based on ASTM E-29 [69], which proposed that for graded materials with a narrow particle size range, such as magnetite, every sieve in the fourth root of two ratios in the series should be used. The sampling sizes of powder, and the shaking time required, were also based on procedures defined in ASTM E-29 [69] standard. Standard test sieves with brass frames and brass wire mesh were used to avoid the static magnetic field that could produce with steel sieves. Two sieves with size openings of 80 mesh and 270 mesh were used for 30.4 μm and 6.9 μm, respectively, in the magnetite powder preparation.

Great care was exercised to obtain gross samples, for sieving, that were closely representative of the batch, and that avoided stratification. ASTM E-29 [69] recommended that the first sampling of the 25 Kg bulk shipment of magnetite should be done using a sampling tube. Five or six insertions of the 1 cm inner diameter, of 25 cm long tube were used to take a sample of a 110 to 120 g from the naturally leveled powder in the container. The sieve shaking times were chosen based on a selection of four samples which were sieving for different times:

for the first, for 5 min, for the second for 10 min, for third for 15 min, and the fourth for 20 min. For most tests, a satisfactory end-point was considered to have been reached when an additional 1 min of sieving failed to change the weight on any of the sieves used by more than 1%. The final sieving times calculated in this manner were 20 min for the finer Craigmont Mines powder, and 15 minutes for coarser Prince Minerals powder.

3.2.2 REDUCTION OF GROSS SAMPLE TO TEST SIZE FOR PARTICLE SIZE ANALYSIS

After the gross sample was appropriately sieved, it was reduced to a suitable size for the particle size analysis test (i.e. a few g). To achieve this, the cone and quartering technique in ASTM E-29 [69] was followed. The gross sample was piled in a cone on a clean, dry smooth surface, by shoveling the power to the apex of the cone, and allowing it to run down equally in all directions. Then the sample was spread in the circle which was gradually widened with the shovel until the powder was spread to a uniform thickness. Finally, the flat pile was split into quarters, and two opposite quarters were rejected. The remaining sample was collected and mixed again into a conical pile. The procedure was repeated until the sample was reduced to the required size.

The particle size distributions of the resulting samples were measured using an optical particle analyzer (Clemex PS^3 Professional Research Particle Size and Shape Image Analysis system, Clemex Technologies Inc., Longueuil, Quebec, Canada).

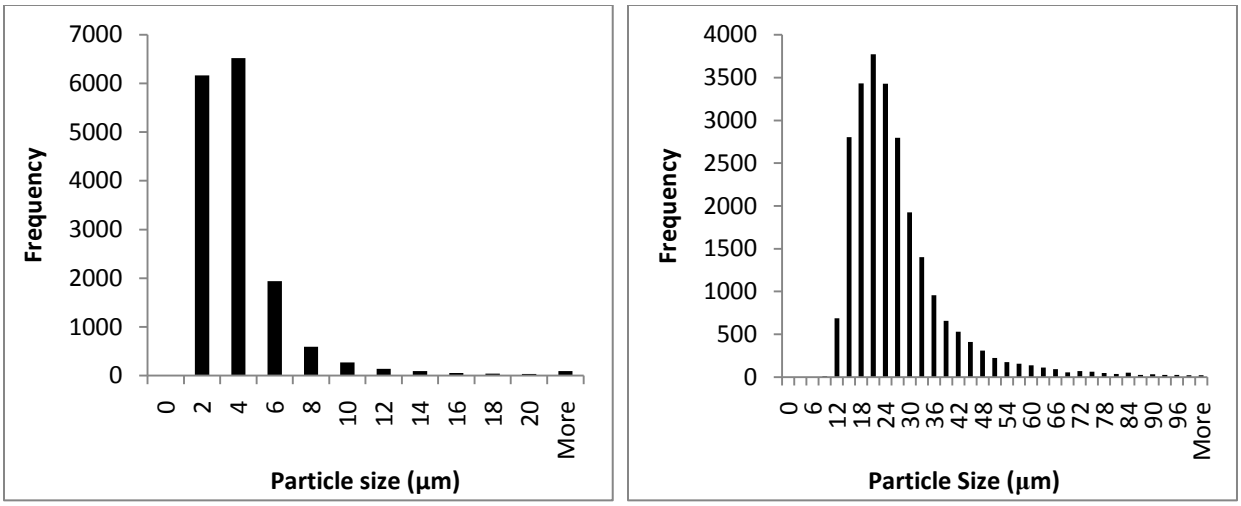

(a) (b)

Figure 3- 4: (a) particle size distribution of Craigmont Mines powder having a mean spherical diameter of 6.9 μm passing through 270 mesh sieve; (b) Particle size distribution of Grade 3105 Prince Mine magnetite powder having a mean spherical diameter of 30.4 μm passing through 80 mesh sieve

Although the particle analyzer image analysis routines allow for some automatic image separation of agglomerated particles, a high degree of agglomeration will affect the accuracy of the sizing results. Preventing particle agglomeration on the sampling slides proved challenging because of their magnetization. The standard procedures suggested by Clemex of suspending the particles in drops of water and alcohol did not solve the agglomeration problem. Scattering the powder samples over the slide by shaking them from a small piece of paper proved to be the best procedure for achieving adequate spacing of the larger particles and preventing agglomeration. Alcohol was suggested the best solvent for separating such and small particle size and sampling process. A droplet of mixture of alcohol and small particle and alcohol stationed between the slide and the cover slip, and consequently placed under microscope for particle sizing process. Figure 3-4 shows the final two magnetite powder size distributions used in the experiments. Figure 3-5 shows photographs of the two samples of magnetite powder.

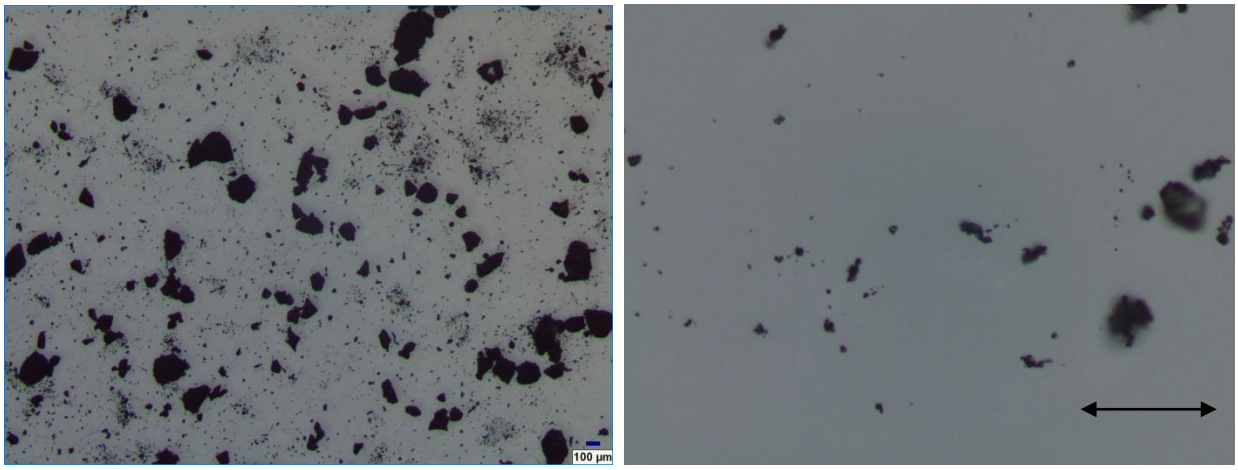

(a) (b)

Figure 3- 5: Black powder samples: (a) Craigmont mines passing through 270 mesh and (b) Prince minerals passing through 80 mesh. Scale bar is 100 µm

3.3 TARGET MATERIALS

The erosion experiments were performed on twelve different materials (Table 3-1), judged by an industrial partner as showing potential for application in new valve systems in the gas pipeline industry. The specifications of the materials can be found in Table A1 to Table A12 of Appendix A. The Tungsten carbide Grade (K3109) was made by sintering with 88% WC and 12% Cobalt binder. It was obtained Kennametal Inc. (Fort Mill, SC, USA). The A1018 steel was nickel plated (100 µm thickness) to a hardness of at least 60 HRC. Nickel plating performed by a vMetalon Technology Ltd. (Orangeville, Ontario). Stellite 6b and Stellite 12 plates were supplied by Deloro Stellite (Belleveille, Ontario). The remaining samples were obtained from Metal Samples Inc. (Munford, TN, USA).

All specimens were polished as per ASTM G76-07 [8] specifications to the recommended surface roughnesses of 1 µm RMS or smaller. All target samples were cut into 50.8 x 101.6 mm strips having thickness between 1.47 mm and 1.97 mm. The as received

hardness values were measured using a MACROVICKERS® 5100 Series (Buehler, Whitby, Ontario) hardness tester, and the surface roughness measured using a stylus profilometer (Taylorsurf 50, Taylor Hobson Precision Ltd., UK). Three repeat measurements of material surface roughness and material hardness were conducted (Table 3-1). To confirm that the specifications of the nickel plate coating were correct, six different incremental loads (10, 50, 100, 300, 500, 2000 gf) were used to measure the hardness, and particular attention was paid to ensure that the indentation depth was less than 15% of the coating thickness. A hardness of HV=745 (N=6) was obtained, equivalent to 62 HRC.

Table 3- 1: Surface roughness of candidate materials. The ± indicates standard deviation of three measurements.

Material	**Surface Roughness Rq (μm)**	**Density ρ (g/cm^3)**	**As-received Vickers Hardness(HV)**
A1018 Carbon Steel With Nickel Plating	0.249±0.04	8.83	746±1
A240 Type 2205 Duplex Stainless Steel	0.062±0.012	7.87	262±1
17-4 PH Stainless Steel	0.131±0.011	7.73	352±2
Type 316L Stainless Steel	0.057±0.005	7.87	164±1
A53 Gr. B Steel	0.138±0.04	7.83	157±2
A240 Type 410 Stainless Steel	0.407±0.007	7.77	152±2
A105 Carbon Steel Forging	0.141±0.025	7.84	161±1
A515 Gr. 70 Norm.	0.088±0.002	7.86	164±1
Alloy 625 plate	0.157±0.03	8.43	227±1
Solid Stellite 12	0.086±0.0008	8.38	492±6
Solid Stellite 6b	0.030±0.003	8.52	361±2
Solid Tungsten Carbide (WC)	0.431±0.001	14.2	1029±10

3.4 METHODOLOGY FOR MEASUREMENT OF EROSION RATE

3.4.1 DEFINITION OF VOLUMETRIC EROSION RATE

The erosion rate is defined in ASTM G76-07 [8] as the volume of target material removed; *V*, per unit mass of particle launched, m_p, and can be calculated from experimental data as follows:

$$E = \frac{V}{m_p} = \frac{V}{\dot{m}t} \tag{3.1}$$

where *V* is the volume of the erosion hole (crater), *t* is the blasting duration or dwell time, and $\dot{m}$ is the abrasive mass flow rate.

3.4.2 MEASUREMENT OF VOLUME OF MATERIAL REMOVED

ASTM G76-07 [8] outlines a procedure whereby measurements of target material mass loss after a certain blasting duration (dwell time) are used together with the material density to infer the volume of material removed, *V*. In the present work, more accurate volume removal measurements were obtained using a noncontact optical profilometer (Nanovea ST400 / 3D Non-Contact Profiler, Micro Photonics Inc., Allentown, PA) which directly measured the eroded volume. The device uses a chromatic aberration technique, and has a 150 mm range X and Y motorized translation stages for scanning specimens, and thus can give a full 3D representation of the eroded scars. By using a 130 µm maximum depth rating optical pen, the erosion scars can be measured with a depth resolution of 5 nm and with a volume measurement resolution of 75 nm^3.

3.4.3 MEASUREMENT OF ABRASIVE MASS FLOW RATE

The abrasive mass flow rate, $\dot{m}$ in eq. (3.1) was measured by blasting in a specially designed collection container with a particulate filter on it, allowing for unimpeded airflow, but limited particle escape. By measuring the weight of the powder that was collected in a given time, the mass flow rate could be calculated. A computer particle tracking simulation [67] indicated that abrasive mass flow rates <4 $g.min^{-1}$ would ensure that <90% of the launched particles would undergo inter-particle collisions.

For the experiments utilizing the 6.9 μm mean spherical diameter powder, the mass flow rate was measured after every third erosion crater was blasted. This precaution ensured that a more accurate measurement of the mass of abrasive was used to blast the holes, since the mass flow rate was found to fluctuate significantly over the course of a day of experiments (1.7 $g.min^{-1}$ to 2.4 $g.min^{-1}$). The mass flow rate fluctuations for this extremely fine powder were typically due to particle agglomeration and nozzle clogging. For experiments utilizing the coarser 30.4 μm mean spherical diameter powder, the mass flow rate was found to fluctuate much less (2.1 $g.min^{-1}$ to 2.55 $g.min^{-1}$), and it was thus only necessary to measure the abrasive mass flow rate every 9 erosion craters.

3.4.4 MEASUREMENT OF PARTICLE VELOCITY

A particle image velocimetry (PIV) system was used to measure the particle velocity at a 10 mm distance from the exit of the 1.5 mm nozzle, at blasting pressures of 100 and 200 kPa. The system (LaVision GmbH, Goettingen, Germany) utilizes a pulsed laser and high speed camera to obtain image pairs of the particles in flight. The laser was passed through a cylindrical

lens to form a light sheet which illuminated a plane of particles on the centerline of the jet. Two laser pulses of six ns duration separated by 100 ns were captured by the high speed camera, resulting in a pair of images of the particles in flight. One hundred such image pairs were collected and analyzed using particle tracking software, to obtain a particle vector velocity field.

The measured magnetite particle velocity profiles are shown in Figures 3-6 and 3-7 for the 6.9 μm particle size and Figures 3-8 and 3-9 for the 30.4 μm particle size. The velocities for 100 kPa and 200 kPa blasting pressures resulted in approximately linear particle velocity distributions, with peaks at approximately 90 and 130 $m.s^{-1}$, respectively. Such linear velocity profiles were consistent with previous measurements on micro-abrasive jets [70].

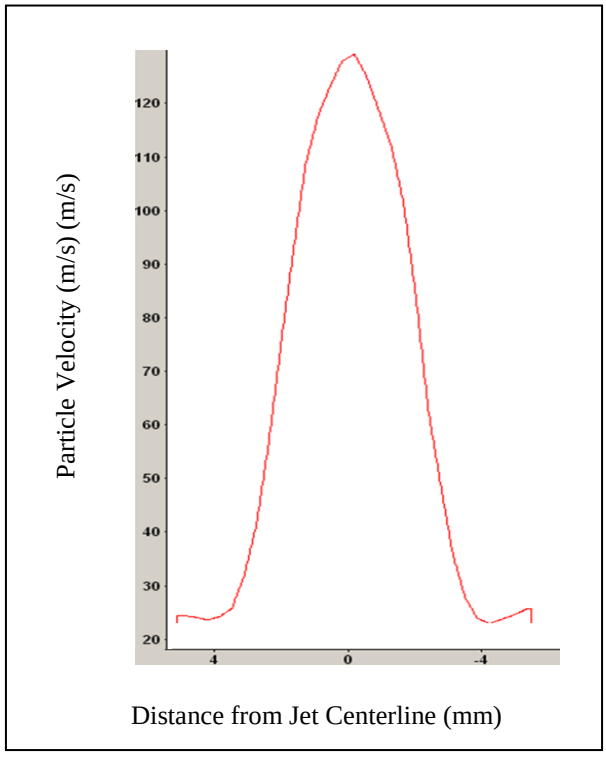

Figure 3- 6: Velocity profile of 6.9 μm particles 10 mm from the nozzle exit using a blasting pressure of P= 200 kPa

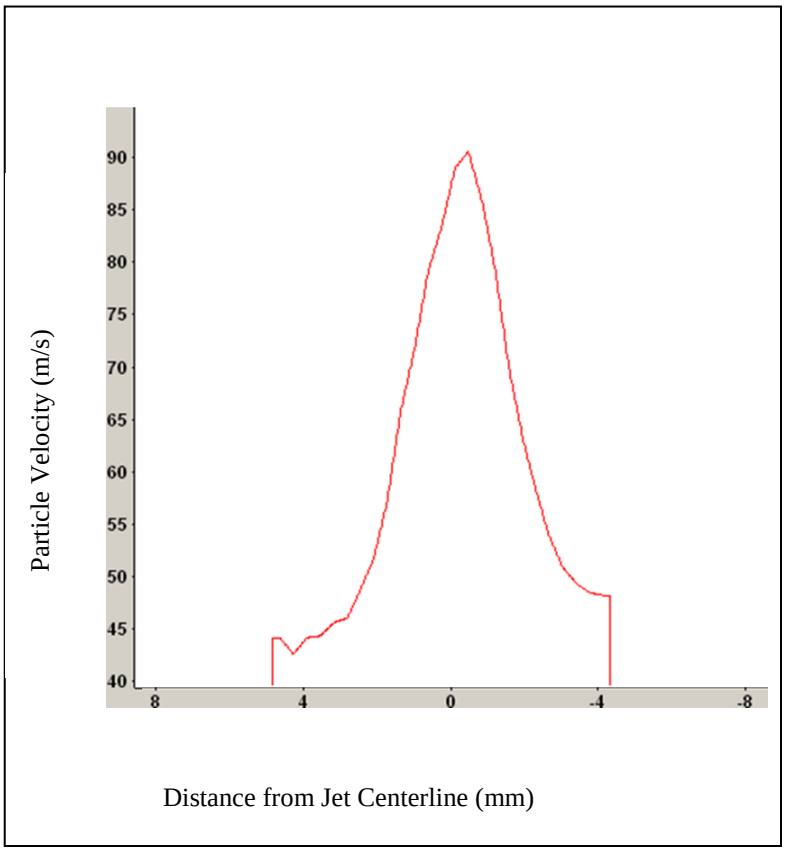

Figure 3- 7: Velocity profile of 6.9 µm particles 10 mm from the nozzle exit using a blasting pressure of P= 100 kPa

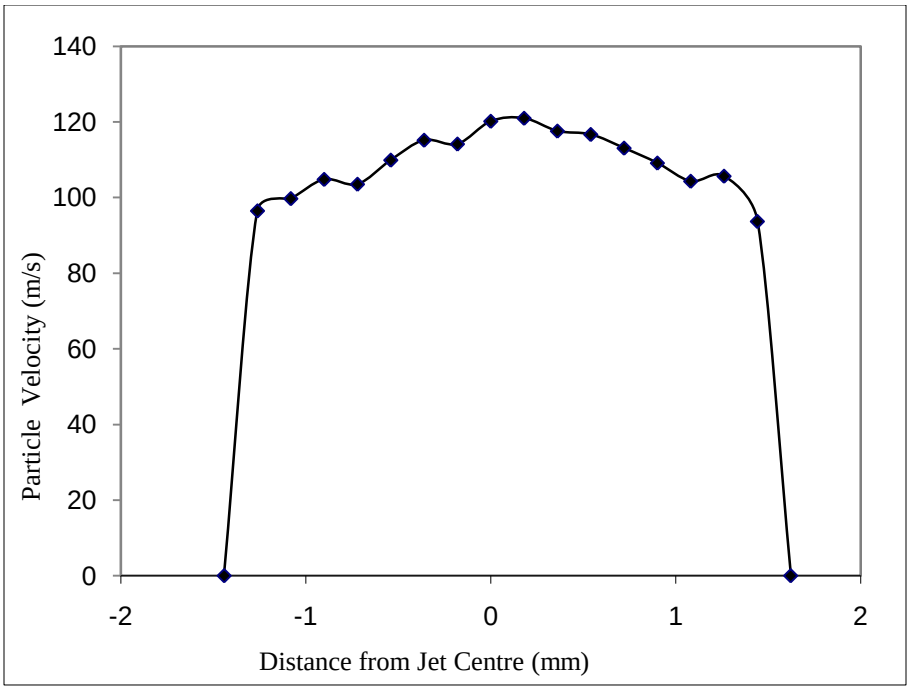

Figure 3- 8: Velocity profile of 30.4 µm particles 10 mm from the nozzle exit using a blasting pressure of P= 200 kPa

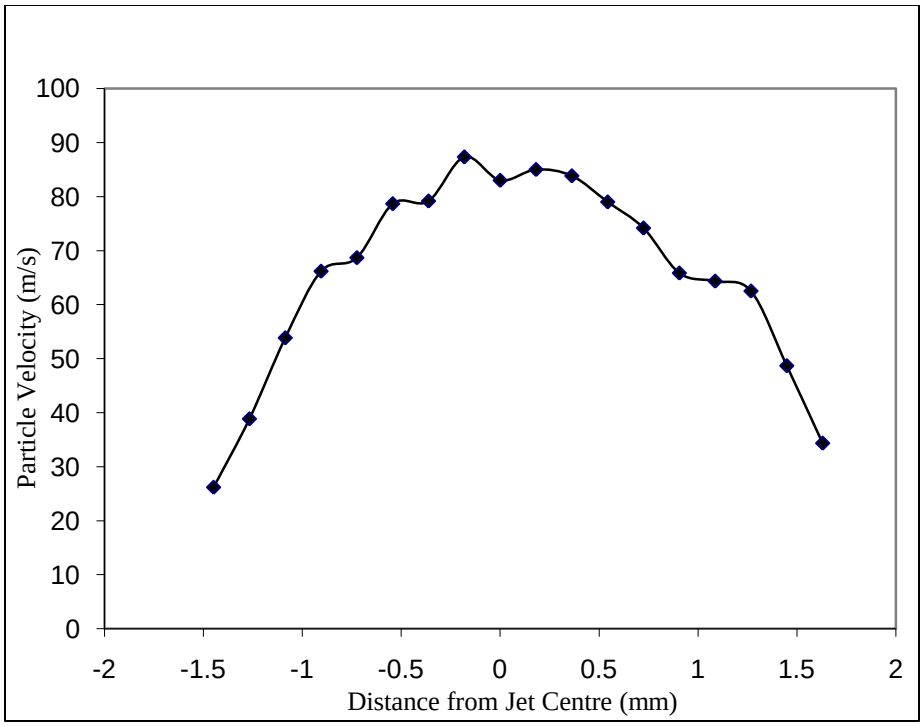

Figure 3- 9: Velocity profile of 30.4 µm particles 10 mm from the nozzle exit using a blasting pressure of P= 100 kPa

3.4.5 DETAILED PROCEDURE

The erosion rate experiments were conducted on the 12 candidate materials with two particle sizes, at two particle velocities (90 and 130 $m.s^{-1}$), and at six angles of impingement (15°, 30°, 45°, 60°, 75°, 90°). Three repeats of each measurement were made (i.e. at a given impingement angle, material, particle size, and particle velocity), each at a different dwell time. Thus the experimental plan called for 72 erosion measurements for each of the materials, giving a total of 792 individual erosion rate measurements (i.e. eroded craters).

The target samples were clamped to the specimen holder. The manual positioning stage of the target was used to ensure that the distance between the nozzle and the surface, along the axis of the nozzle, remained constant at 10 mm, regardless of the angle of attack. Based on preliminary measurements using a 1.5 mm nozzle at a 10 mm standoff distance (as per ASTM

G76-07 [8]), the largest erosion scar that was formed at 15º impingement angle was approximately 22 mm in length and 10 mm in width. Thus, the 50 x 100 mm plate dimension could easily accommodate three rows of three holes on each face of the sample, for a total of 18 holes per sample (Figure 3-10). Since each material would require two particle velocities, six angles of attack, and two particle sizes, each with three holes, for a total of 72 holes, a total of four specimens of each material were used.

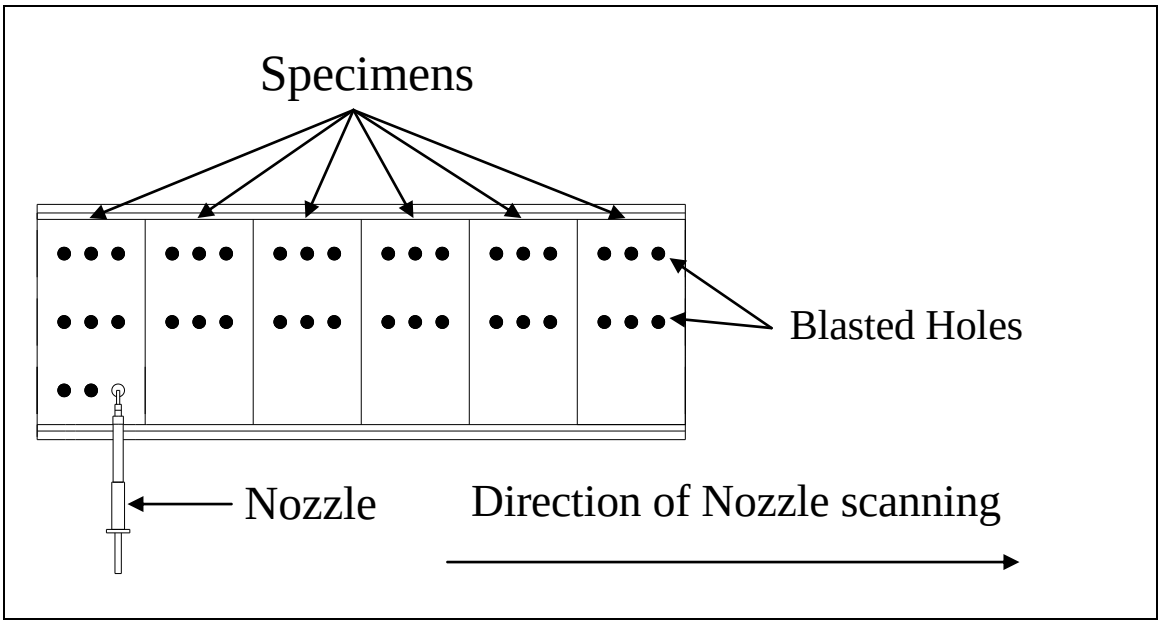

Figure 3-10: Configuration of nozzle and specimens while blasting the holes

In a single experimental run, a given particle size and velocity were held constant, and six samples of, each of a different material were placed side by side on the specimen holder. The nozzle was oriented at a given impingement angle, and the stages were programmed to blast three holes at different dwell times, evenly spaced on each sample. The stages were programmed such that the dwell time to blast the three holes was automatically changed when moving from one hole to another on each material. The minimum dwell time was chosen based on the minimum time required to reach steady-state erosion rate conditions (i.e. the ‘steady-state dwell

time'), and achieving a deep enough crater to ensure an accurate measurement of crater volume. This was determined for every material and using both particle sizes, for the high velocity experiments, at the 15˚ and 90˚ impingement angles. The angles represented the extremes, i.e. the 15˚ case resulted in the largest erosion scar, but the shallowest crater, and the 90˚ case had the smallest erosion scar, but the deepest crater.

By plotting the erosion rate as a function of dwell time, the minimum time required for a linear relationship was established. The two other dwell times to be used at each condition were chosen so as to ensure that the crater was no deeper than the 350 μm depth suggested in ASTM G76-07 [8]. For the low velocity experiments, the erosion rates were found to be between 40% and 55% of those obtained in the high velocity case and the dwell times were raised accordingly. The dwell times obtained in this manner are summarized in Tables 3-2 and 3-3.

Table 3- 2: Dwell times (s) chosen for three holes made at each condition. Experiments performed on 6.9 µm at 130 m/s and 90 m/s peak particle velocity, respectively

Material	Dwell Time (s)											
	$\alpha = 15^{\circ}$		$\alpha = 30^{\circ}$		$\alpha = 45^{\circ}$		$\alpha = 60^{\circ}$		$\alpha = 75^{\circ}$		$\alpha = 90^{\circ}$	
	130 m/s Vel.	90 m/s Vel.	130 m/s Vel.	90 m/s Vel.	130 m/s Vel.	90 m/s Vel.	130 m/s Vel.	90 m/s Vel.	130 m/s Vel.	90 m/s Vel.	130 m/s Vel.	90 m/s Vel.
A1018 Carbon Steel Nickel Plating	20 15 15	20 20 20	10 10 10	15 15 15	15 15 15	20 20 20	15 15 15	30 30 30	15 15 15	30 30 30	15 15 15	15 15 15
A240 Type 2205 Duplex Stainless Steel Plate	60 90 120	120 180 210	60 90 120	90 180 210	60 90 120	90 180 210	60 90 120	90 180 210	60 90 120	90 180 210	60 90 120	90 180 210
17-4 PH Stainless Steel Plate	60 90 120	120 180 210	60 90 120	90 180 210	60 90 120	90 180 210	60 90 120	90 180 210	60 90 120	90 180 210	60 90 120	90 180 210
Type 316L Stainless Steel	60 90 120	120 180 210	60 90 120	90 180 210	60 90 120	90 180 210	60 90 120	120 180 210	60 90 120	90 180 210	60 90 120	90 180 210
A53 Gr. B Steel	60 90 120	120 180 210	60 90 120	90 180 210	60 90 120	90 180 210	60 90 120	90 180 210	60 90 120	90 180 210	60 90 120	90 180 210
A240 Type 410 Stainless Steel plate	60 90 120	120 180 210	60 90 120	90 180 210	60 90 120	90 180 210	60 90 120	90 180 210	60 90 120	90 180 210	60 90 120	90 180 210
A105 Carbon Steel forging	60 90 120	120 180 210	60 90 120	90 180 210	60 90 120	90 180 210	60 90 120	90 180 210	60 90 120	90 180 210	60 90 120	90 180 210
A515-70- A515 Gr. 70 Norm. Plate	60 90 120	120 180 210	60 90 120	90 180 210	60 90 120	90 180 210	60 90 120	90 180 210	60 90 120	90 180 210	60 90 120	90 180 210

Table 3- 2(continue): Dwell times (s) chosen for three holes made at each condition. Experiments performed on 6.9 µm at 130 m/s and 90 m/s peak particle velocity, respectively

Material	Dwell Time (s)											
	$\alpha = 15^{\circ}$		$\alpha = 30^{\circ}$		$\alpha = 45^{\circ}$		$\alpha = 60^{\circ}$		$\alpha = 75^{\circ}$		$\alpha = 90^{\circ}$	
	130 m/s Vel.	90 m/s Vel.	130 m/s Vel.	90 m/s Vel.	130 m/s Vel.	90 m/s Vel.	130 m/s Vel.	90 m/s Vel.	130 m/s Vel.	90 m/s Vel.	130 m/s Vel.	90 m/s Vel.
Alloy 625 Plate	60 90 120	120 180 210	60 90 120	90 180 210	60 90 120	90 180 210	60 90 120	90 180 210	60 90 120	90 180 210	60 90 120	90 180 210
Solid Stellite 12	60 90 120	180 210 240	60 90 120	120 180 210	60 90 120	90 180 210	60 90 120	90 180 210	60 90 120	90 180 210	60 90 120	90 180 210
Solid Stellite 6b	66 99 120	120 180 210	60 90 120	120 180 210	60 90 120	120 180 210	60 90 120	120 180 210	60 90 120	120 180 210	60 90 120	120 180 210
Solid Tungsten Carbide	400	400	400	400	400	400	400	400	400	400	400	400

Table 3- 3: Dwell times (s) chosen for three holes made at each condition. Experiments performed on 30.4 µm at 130 m/s and 90 m/s peak particle velocity, respectively

Material	Dwell Time (s)											
	α = 15°		**α = 30°**		**α = 45°**		**α = 60°**		**α = 75°**		**α = 90°**	
	130 m/s Vel.	90 m/s Vel.	130 m/s Vel.	90 m/s Vel.	130 m/s Vel.	90 m/s Vel.	130 m/s Vel.	90 m/s Vel.	130 m/s Vel.	90 m/s Vel.	130 m/s Vel.	90 m/s Vel.
A1018 Carbon Steel Nickel Plating	60 60 60	90 90 90	10 10 10	90 90 90	30 30 30	30 30 30	30 30 30	30 30 30	15 15 15	30 30 30	15 15 15	30 30 30
A240 Type 2205 Duplex Stainless Steel Plate	120 150 180	300 330 360	120 150 180	300 330 360	150 180 210	210 240 270	120 150 180	210 240 270	90 120 150	120 150 180	90 120 150	210 240 270
17-4 PH Stainless Steel Plate	150 180 210	300 330 360	120 150 180	300 330 360	150 180 210	210 240 270	120 150 180	210 240 270	90 120 150	210 240 270	90 120 150	210 240 270
Type 316L Stainless Steel	150 180 210	300 330 360	120 150 180	300 330 360	150 180 210	210 240 270	120 150 180	210 240 270	90 120 150	210 240 270	90 120 150	210 240 270
A53 Gr. B Steel	150 180 210	300 330 360	120 150 180	300 330 360	150 180 210	210 240 270	120 150 180	210 240 270	90 120 150	210 240 270	90 120 150	210 240 270
A240 Type 410 Stainless Steel Plate	210 240 270	210 240 270	120 150 180	300 330 360	150 180 210	210 240 270	120 150 180	210 240 270	90 120 150	210 240 270	90 120 150	210 240 270
A105 Carbon Steel Forging	150 180 270	300 390 420	120 150 180	300 330 360	150 180 210	210 270 270	120 150 180	210 240 270	90 120 150	210 240 270	90 120 150	210 240 270
A515-70- A515 Gr. 70 Norm. Plate	150 180 210	360 390 420	120 150 180	300 330 360	150 180 210	210 240 270	120 150 180	210 240 270	120 150 180	210 240 270	90 120 150	210 240 270

Table 3- 3(continue): Dwell times (s) chosen for three holes made at each condition. Experiments performed on 30.4 μm at 130 m/s and 90 m/s peak particle velocity, respectively

Material	Dwell Time (s)											
	α= 15°		α= 30°		α= 45°		α= 60°		α= 75°		α= 90°	
	130 m/s Vel.	90 m/s Vel.	130 m/s Vel.	90 m/s Vel.	130 m/s Vel.	90 m/s Vel.	130 m/s Vel.	90 m/s Vel.	130 m/s Vel.	90 m/s Vel.	130 m/s Vel.	90 m/s Vel.
Alloy 625 Plate	210 240 270	300 330 360	120 150 180	360 390 420	150 180 210	210 240 270	120 150 180	210 240 270	90 120 150	210 240 270	90 120 150	210 240 270
Solid Stellite 12	210 240 270	360 390 420	180 210 240	360 390 420	180 210 240	270 300 330	180 210 240	270 300 330	180 210 240	270 300 330	150 180 210	270 300 330
Solid Stellite 6b	210 240 360	360 390 420	180 210 240	360 390 420	180 210 240	270 300 330	180 210 300	270 300 330	180 210 330	270 300 330	150 180 210	270 300 330
Tungsten Carbide	400	400	400	400	400	400	400	400	400	400	400	400

The stages were scanned at maximum speed between the holes (time period on the order of a few seconds), leaving an extremely shallow channel between the much deeper holes (on the order of a few minutes each). Since the erosion rate was measured on the basis of the volume of material removed in the blasted holes, these shallow channels did not affect the measurement. After each row of 18 holes spanning the specimens was completed, the nozzle was rotated about an axis parallel to the scanning direction to a different angle of attack (Figure 3-11). The sequence was repeated for the combinations of particle velocity and size, as shown in Figure 3-12.

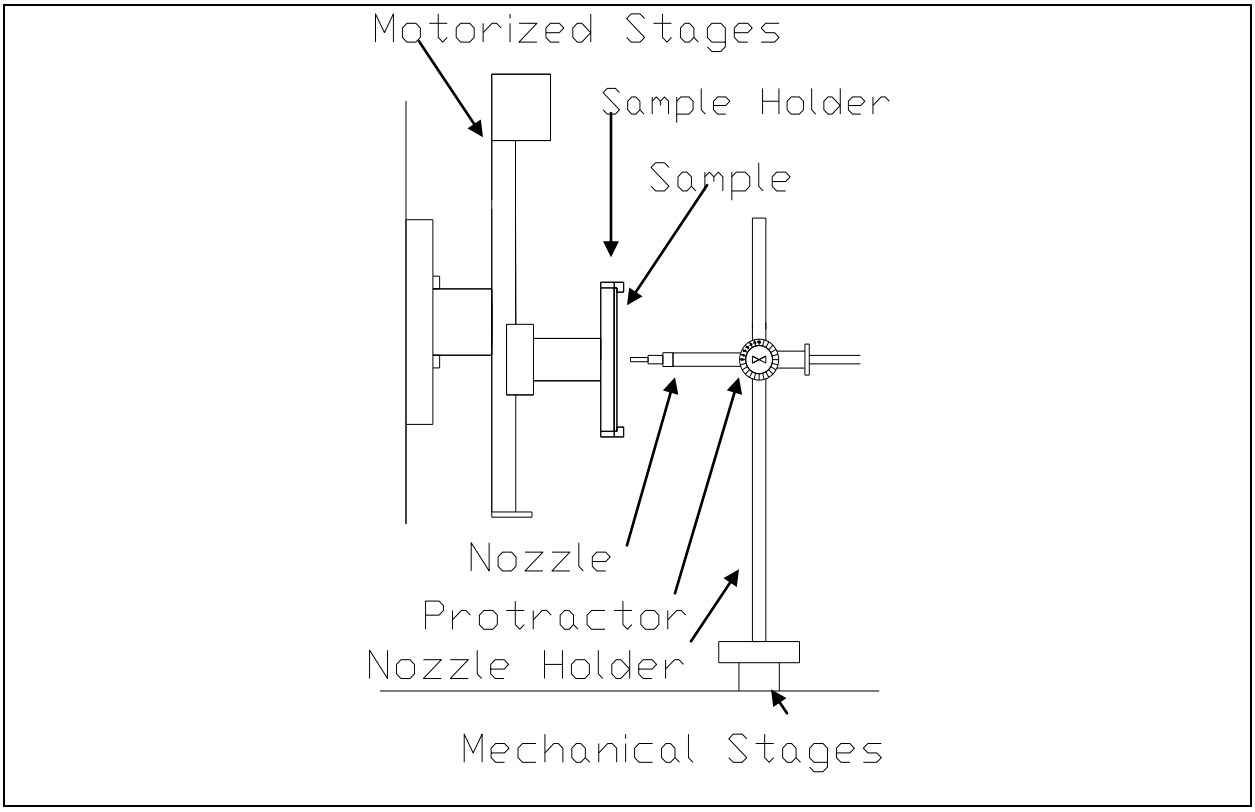

Figure 3- 11: Detail of sample holder, and stages

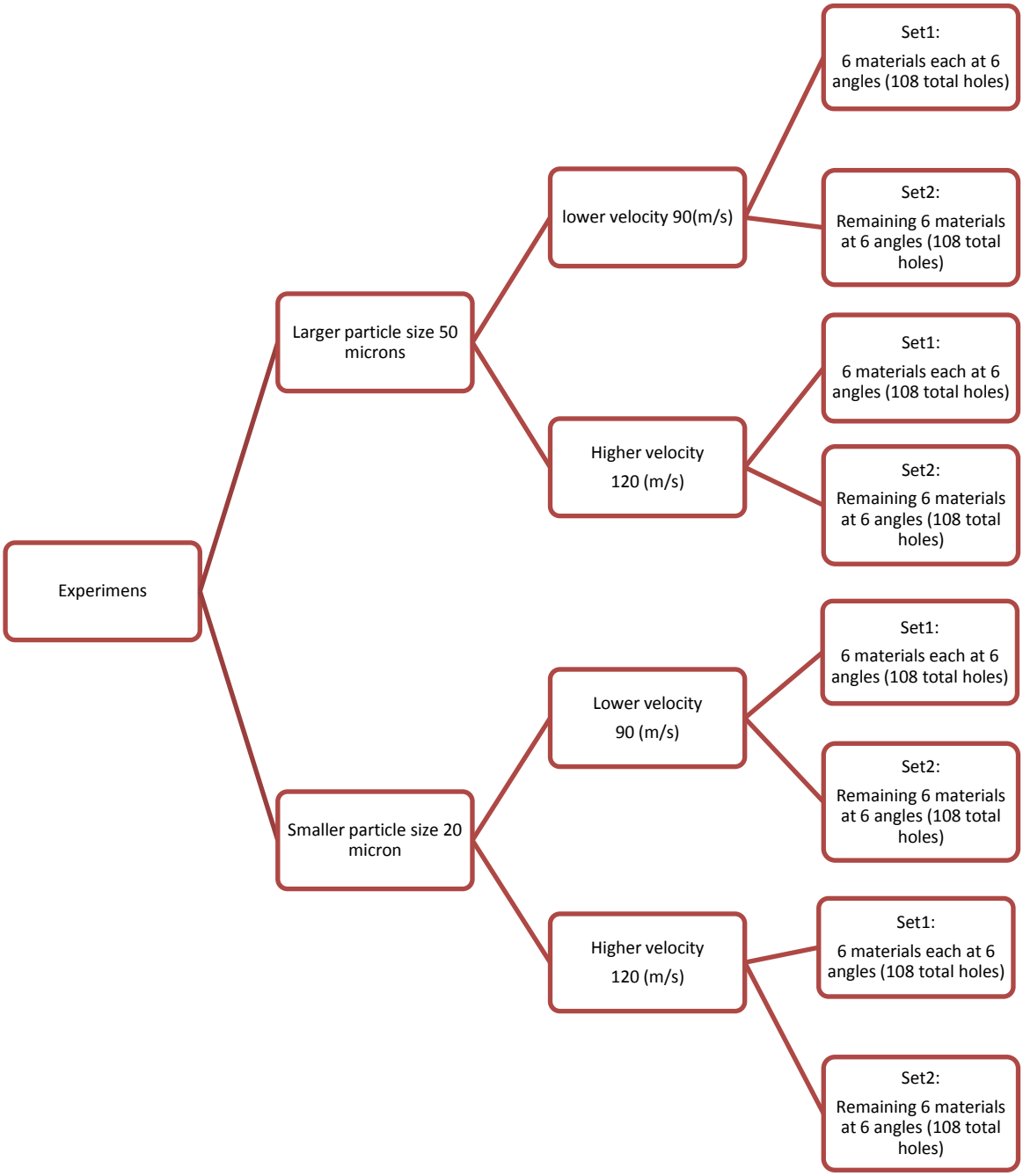

Figure 3- 12: Sequence of erosion rate measurements

The volumetric erosion rate was calculated as the slope of the least squares best fit line of a plot of the measured volume removal versus mass of abrasive used for the three dwell times. It should be noted that in the case of the nickel coated A 1018 steel, it was not possible to use three different dwell times that resulted in erosion craters that were less than the 100 μm coating thickness. In this case, the erosion rates were reported as the average of three repeats at a single dwell time for each experimental condition.

CHAPTER 4

CURVE FITTING OF EXPERIMENTAL EROSION RATES

The dependence of erosion rate on process parameters (angle of attack, velocity, etc.) can often be fit to existing erosion models in the literature. Fitting such a model can often provide some physical significance to the erosion rate dependencies. Moreover, the fits can also be used for more advanced simulations, which can predict the eroded surface profiles in real engineering parts. For example, in the present work, the industrial sponsor of the research required that the erosion data be fit to a model suitable to be implemented into the computational fluid dynamics software, Fluent, thus enabling the eroded profiles in real pipelines and control valves to be predicted. This chapter describes the erosion model used for curve fitting of numerical erosion rates, and the curve fitting algorithm.

4.1 CONVERSION OF VOLUMETRIC EROSION RATE TO DIMENSIONLESS EROSION RATE

From the volume of target material removed per mass of impinging particles ($mm^3 \cdot kg^{-1}$) (Table 1 to 6 of Appendix B), as suggested by ASTM G-76-07 [8], the volumetric erosion rates, measured according to eq. (3-1) were presented In Tables 1 to 4 of Appendix C. However, most erosion models (see eq. (4-1) require a dimensionless erosion rate ($g.g^{-1}$) expressed as the mass of target material removed per unit mass of erodent launched. Therefore, the target material density was used to convert the volumetric erosion rates to dimensionless ones. The target material densities are given in Table 3-1, and the resulting dimensionless erosion rate values are presented in Tables 1 to 4 of Appendix D.

4.2. MODEL OF OKA ET AL. [1] FOR DEPENDENCE OF EROSION ON ANGLE OF ATTACK

Oka et al. [1] proposed an empirical equation for solid particle erosion damage that can be applied to many types of metallic materials at various impact angles, velocities, and particle sizes. They performed a detailed investigation of the effects of these parameters for several aluminum, carbon steel, stainless steel, and copper specimens, and found that target hardness had a great effect on the resulting erosion rate. The erosion rate data were converted to dimensionless erosion rate, and fit to an equation of the form:

$$\xi = \frac{m_t}{m_p} = Cv^{n_3} g(\alpha) \tag{4.1}$$

where ξ is the dimensionless erosion rate expressed as mass of target material removed, m_t per mass of impacting particles, m_p ($g.g^{-1}$). In their model, the ratio of erosion damage at an arbitrary angle, ξ (α), to that at normal incidence, $\xi_{90,}$ was expressed as the product of two trigonometric functions [1]:

$$g(\alpha) = (\sin\alpha)^{n_1}(1 + Hv(1 - \sin\alpha))^{n_2} \tag{4.2}$$

where α is the angle between the target surface and the velocity vector of the incoming particles, and HV is the initial Vickers hardness of the materials in GPa. The first and second terms in equation (4.2) express the portion of erosion due to the repeated deformation, and the cutting material removal mechanisms, respectively [1].

The final equation to fit is thus:

$$\xi = Cv^{n_3}(\sin\alpha)^{n_1}(1+Hv(1-\sin\alpha))^{n_2} \tag{4.3}$$

where C, n_1, n_2, HV, and n_3 were determined by curve fitting.

The procedure for obtaining the curve fits was:

(i) The volumetric erosion rates were converted to dimensionless erosion rates.

(ii) Since *g (α)* represented the ratio of the dimensionless erosion rate at a given angle to that at normal (α =90 deg.) incidence, the dimensionless erosion rates from (i) were normalized by their values at normal incidence (Table 1 to 4 Appendix E). This allowed for an initial fitting of the *g (α)* function, i.e. determination of constants n_1, n_2 and HV.

(iii) The remaining velocity exponent, n_3, and C constant were curve fitted using the particle velocity, the normalized erosion rate fits, and the erosion rate data.

As shown in Figure 4-1, n_1 and n_2 in Oka's model account for the effects of repeated plastic deformation and cutting action. Cutting dominates at low angles of attack, and repeated deformation at high angles of attack. Cutting processes usually dominate for ductile materials such as metals, and the repeated deformation processes usually dominate for more brittle target materials. Therefore, it is expected that brittle erosive systems have erosion rate peaks at high angles of attack, and ductile erosive systems will have erosion rate peaks at intermediate to low angles of attack.

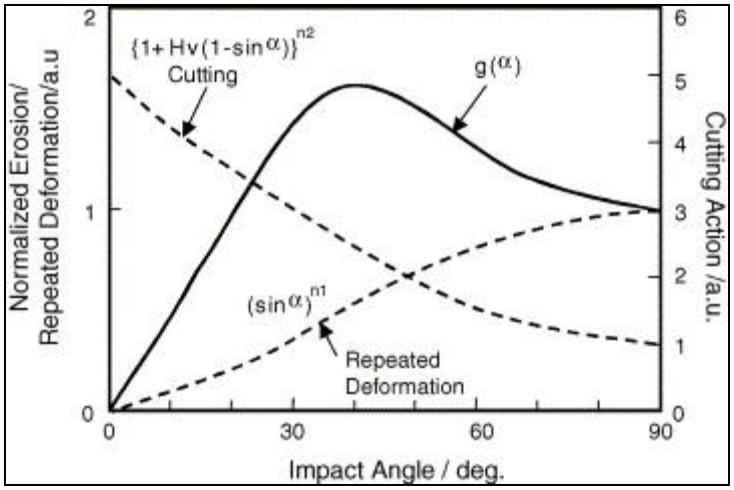

Figure 4- 1: Dependency of cutting action and repeated deformation on material removal mechanisms on angle of attack [1]

4.3 CURVE FITTING ALGORITHM

The nonlinear least squares method in the curve fitting toolbox in MATLAB version 2009b was used for all curves fitting of the erosion rate data. For the nonlinear fit in eq. 4.3, the Trust-region algorithm was used, which requires coefficient constraints. Calculation of these quantities required numerical finite difference approximations to the Jacobians. In the present work, the minimum and maximum changes in the Jacobians were assumed to be 10^{-8} and 0.1. The fit convergence criteria were set to 10^{-6} for the model coefficients. A maximum of 600 function (model objective function) evaluations was allowed, and a maximum of 400 fit iterations was allowed, which provided the highest optimization phase of the fit.

The MATLAB R2009b (The MathWorks, Inc., United States) curve fitting routine required starting values and constraints (i.e., upper and lower bounds) for the coefficients. The default starting values were chosen at random in the interval [0, 1] for all coefficients. Following Oka et al.[1], the upper bounds were chosen as $n_1 = 2$, $n_2 = 1$ (Table 1 of Appendix F). The Vickers hardness (HV) parameters were constrained to be in the range (-10%) to (+50%) of their

as-received values, given in Table 2 of Appendix F. This range, consistent with the work of other investigators [63], [71] was defined in order to allow for a work hardening layer that may have formed beneath the impacting particles. Such a layer might have changed the hardness from the as-received values. No constraints were placed on the erosion constant C, and the velocity exponent was constrained to be in the range of (1.5-3), based on common values in the literature for the solid particle erosion of metals [56]. The n_1, n_2, HV, n_3, and C values are presented in Tables 3 of Appendix F.

CHAPTER 5

RESULTS AND DISCUSSION

This chapter will present results and discussions related to the measured erosion rates, the predominant erosion mechanisms, the ranking of the erosion resistance of the target materials, and the curve fitting parameters.

5.1 MEASURED EROSION RATES AND POSSIBLE MECHANISMS: 6.9 MICRON PARTICLE SIZE

Figures 5-1 and 5-2 show the typical eroded Type 316L stainless steel samples at six angles of impact. Most of plots that were use to derive the measured erosion rates show the expected linear relationship between material volume removal and abrasive mass, indicating a steady state erosion rate and a relatively good repeatability. Two typical plots are shown in Figures 5-3 and 5-4.

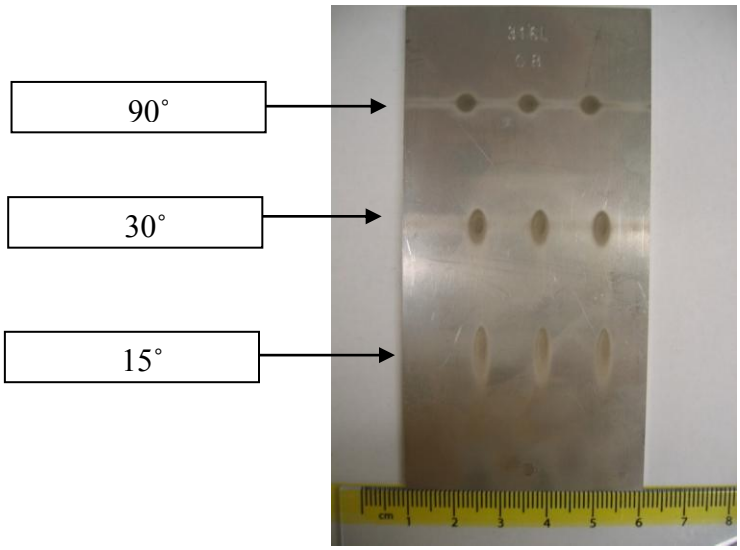

Figure 5-1: Type 316L Stainless Steel, P= 100 kPa, particle size= 6.9 µm, α= 15°, 30°, and 90°(bottom up), Dwell times (right to left): 210, 240, 270s for 90°, 300, 330, 360 s for 30°, and 15°.

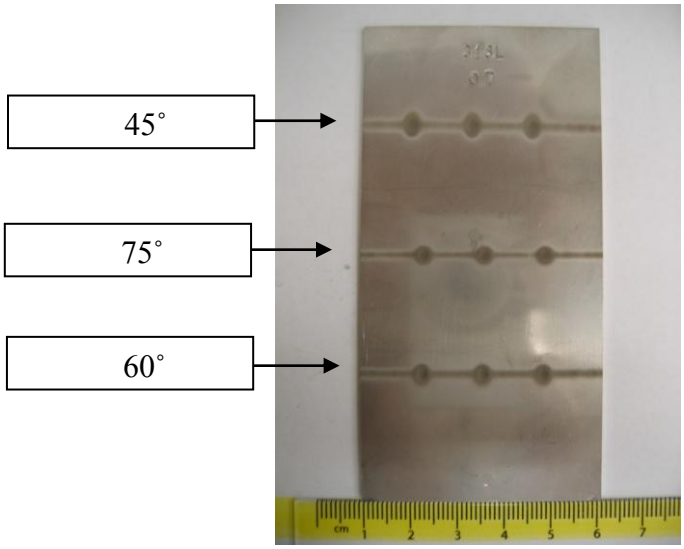

Figure 5- 2: Type 316L Stainless Steel, P= 100 kPa, particle size= 6.9 µm, α= 60°, 75°, and 45° (bottom up), Dwell Times (right to left): 210, 240, 270s for 60°, 30°, and for 45°.

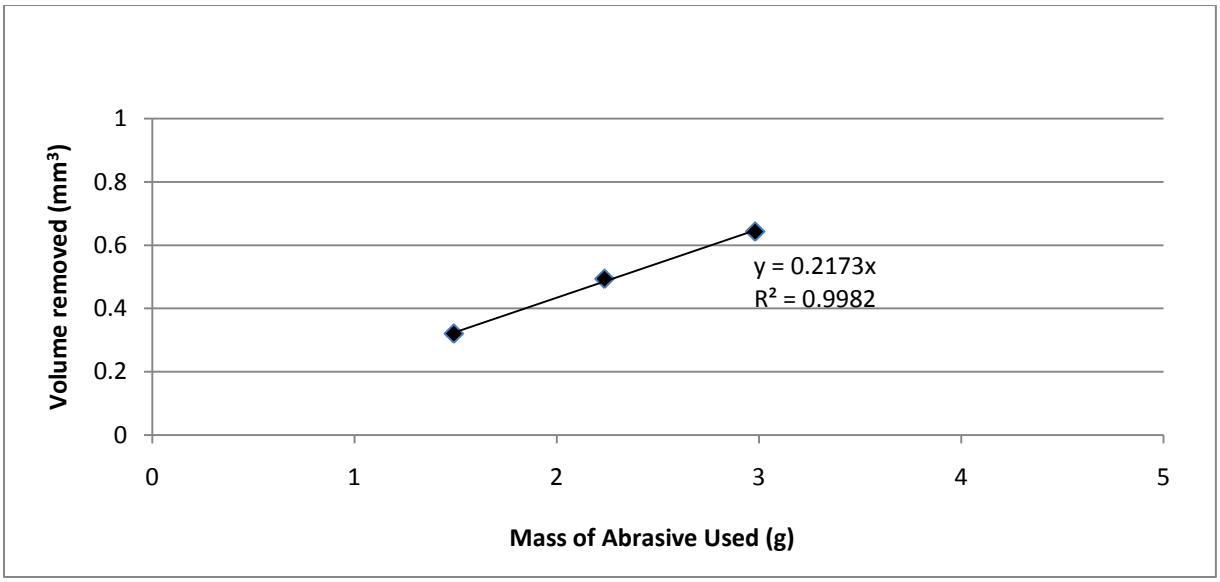

Figure 5- 3: Type 316L stainless steel: Volume removed vs. abrasive mass used and best fit line. Experimental conditions: impingement angle, α=30˚; velocity = 130 m.s^{-1}; blasting times= 60, 90, 120 s

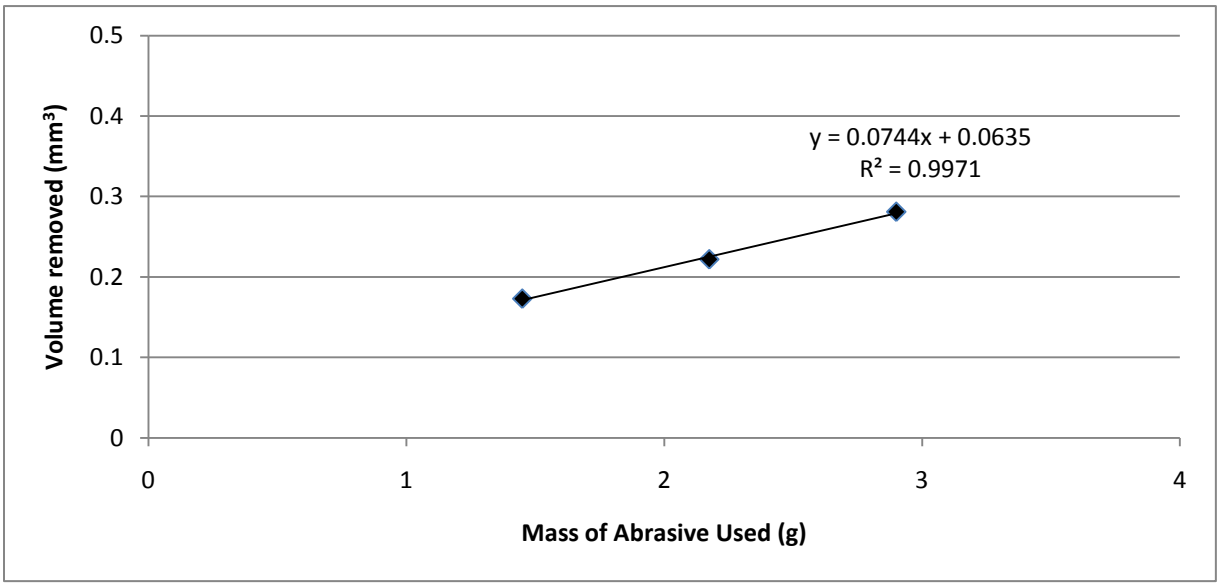

Figure 5- 4: ASTM A240 Type 410 stainless steel plate: Volume removed vs. abrasive mass used and best fit line. Experimental conditions: impingement angle, α= 75˚; particle velocity =130 m.s^{-1}; blasting times=60, 90, 120 s

In Figure 5-3, the linear fits do not pass through the origin. In these cases, it is possible that a two-stage erosion process occurred, with a higher initial erosion rate (i.e. between the

origin and some time before the first data point), followed by a lower steady state erosion. In all cases, the erosion rate has been reported as the best fit linear line, regardless of whether it passes through the origin or not (i.e. the steady-state erosion rate).

The reason for this two stage erosion is not clear. One possible reason could be the presence of an oxide layer of lower hardness than the steel. The higher initial erosion rate might also be due to knocking off of asperities on the initially rough surface. Such an effect might still be seen for such a small particle size, despite the fact that the roughness of all the materials were measured in Table 3-1 using the optical profilometer and found to be $R_q < 1$ μm RMS, as required by ASTM G76-07 [8]. A third possibility is the formation of a work hardened layer as the virgin material was initially eroded. Such an effect has recently been seen by Stachowiak and Batchelor [72] in the abrasion testing of metals, but has not been previously reported in solid particle erosion testing.

Figures 5-5 and 5-6 show the same data plotted in terms of dimensionless erosion rate (g/g) that are presented in Tables 3 and 4 of Appendix D, along with the curve fit values using the model of Oka et al. [1]. Figures 5-7 and 5- 8 show the measured volumetric (mm^3/g) erosion rates for the 6.9 μm powder blasted at 130 $m.s^{-1}$ and 90 $m.s^{-1}$, respectively. The dimensionless erosion rates at 130 $m.s^{-1}$ particle velocities were approximately twice that measured for 90 $m.s^{-1}$ particle velocity.

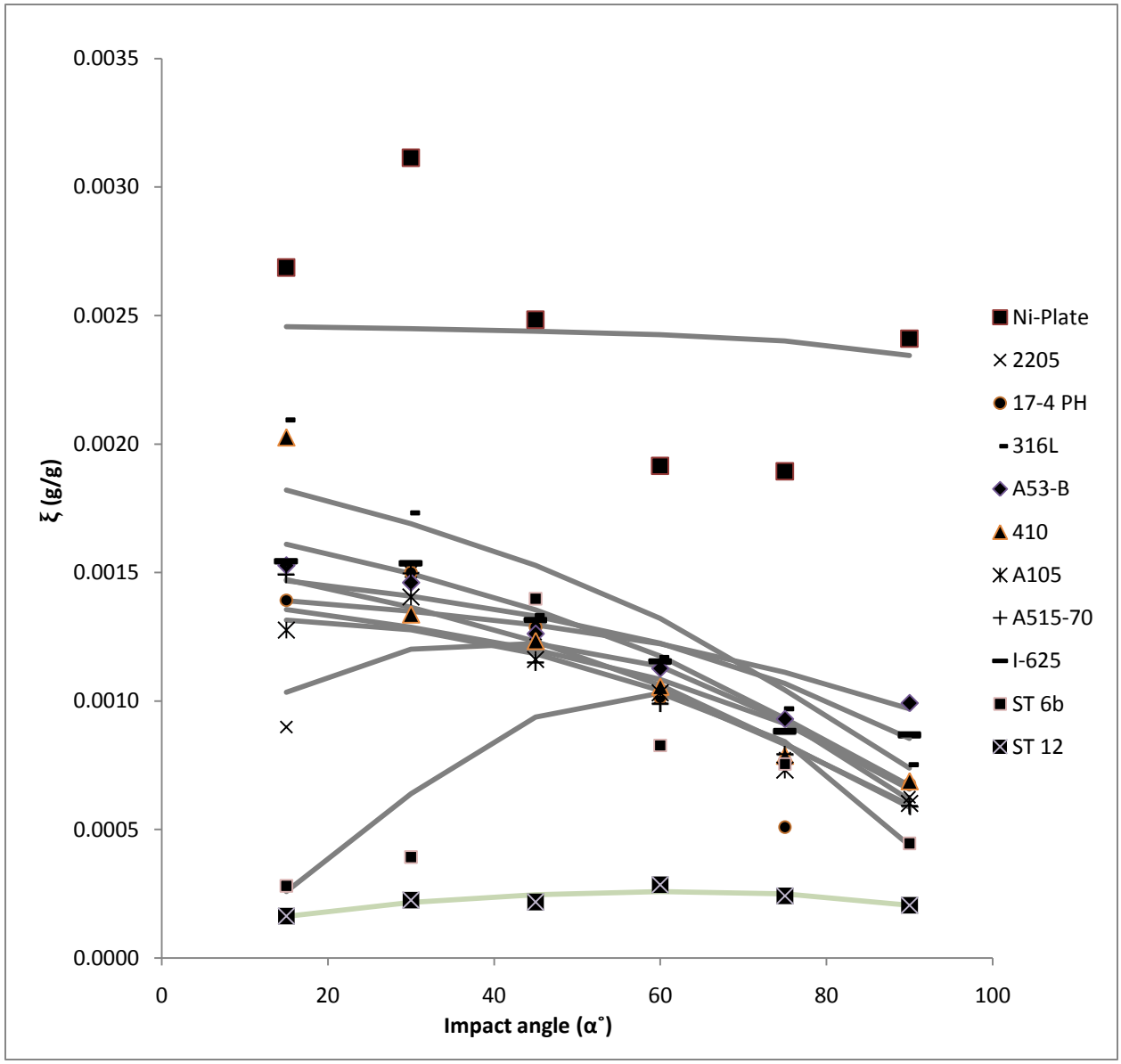

Figure 5- 5: Comparison of measured (points) and curve fit (lines) dimensionless erosion rates for 11 candidate materials for 130 m.s^{-1} and d= 6.9 µm. Legend indicates: Ni Plate - Nickel plating on A1018 carbon steel supporting substrate; 2205- A240 Type 2205 duplex stainless steel plate; 17-4ph- 17-4 PH stainless steel plate; 316L- Type 316L stainless steel; A53-B- A53 Gr. B steel; 410- A240 Type 410 stainless steel plate; A105- A105 carbon steel forging, A515-70- A515 Gr. 70 norm. plate; I-625- Alloy 625 plate; ST12- Solid Stellite 12; ST6b- Solid Stellite 6b

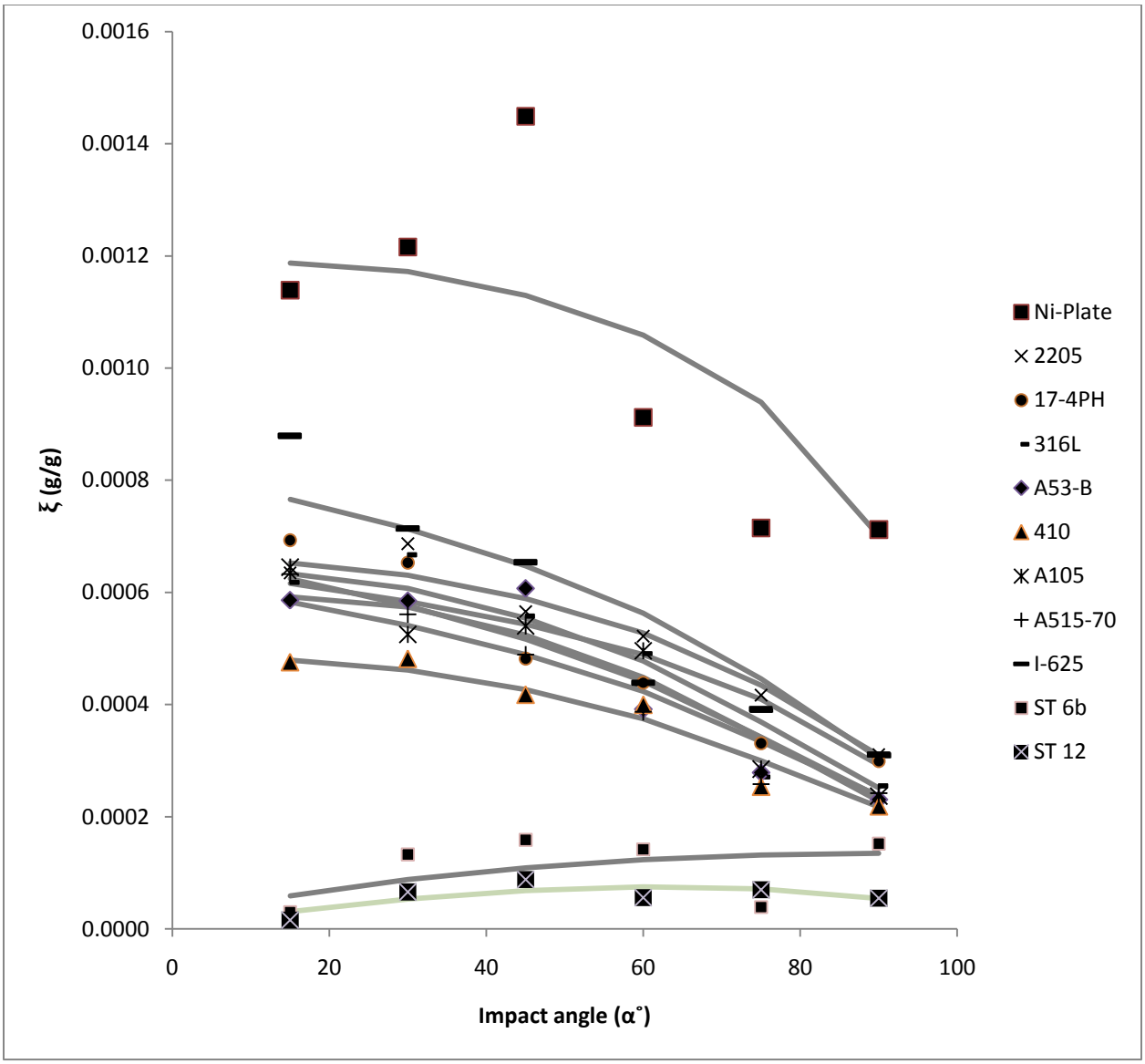

Figure 5- 6: Comparison of measured (points) and curve fit (lines) dimensionless erosion rates for 11 candidate materials for 90 m.s^{-1} and d= 6.9 µm. Legend indicates: Ni Plate - Nickel plating on A1018 carbon steel supporting substrate; 2205- A240 Type 2205 duplex stainless steel plate; 17-4ph- 17-4 PH stainless steel plate; 316L- Type 316L stainless steel; A53-B- A53 Gr. B steel; 410- A240 Type 410 stainless steel plate; A105- A105 carbon steel forging, A515-70- A515 Gr. 70 norm. plate; I-625- Alloy 625 plate; ST12- Solid Stellite 12; ST6b- Solid Stellite 6b

Table 5- 1: Erosion resistance rankings of 12 candidate materials for high particle velocity (130 m.s^{-1}) erosion rate experiments. Rankings are from most (1) to least (12) erosion resistant. Volumetric erosion rates under each condition (mm^3/g) are shown in parenthesis

Rank	**Impingement Angle, α and Erosion Rate (mm^3/g)**					
	15°	**30°**	**45°**	**60°**	**75°**	**90°**
1	WC (0)	WC (0)	WC (0)	WC (0)	WC (0)	WC (0)
2	ST. 12 (0.032)	ST. 12 (0.011)	ST. 12 (0.023)	ST. 12 (0.020)	ST. 12 (0.024)	ST. 12 (0.018)
3	ST. 6B (0.034)	ST. 6B (0.046)	A515-70 (0.112)	ST. 6B (0.098)	17-4PH (0.070)	2205 (0.069)
4	2205 (0.091)	A105 (0.167)	A53-B (0.13)	A105 (0.105)	A105 (0.077)	A105 (0.076)
5	17-4PH (0.145)	A53-B (0.172)	A105 0.137)	2205 (0.109)	I-625 (0.079)	A515-70 (0.079)
6	A105 (0.147)	2205 (0.179)	410 (0.147)	A515-70 (0.111)	2205 (0.085)	410 (0.079)
7	316L (0.181)	I-625 (0.18)	I-625 (0.152)	A53-B (0.113)	ST. 6B (0.098)	ST. 6B (0.053)
8	I-625 (0.184)	17-4PH (0.195)	17-4PH (0.159)	I-625 (0.116)	410 (0.101)	17-4PH (0.087)
9	A515-70 (0.193)	410 (0.199)	2205 (0.164)	17-4PH (0.135)	A515-70 (0.104)	316L (0.098)
10	A53-B (0.211)	A515-70 (0.213)	ST. 6B (0.166)	316L (0.141)	316L (0.216)	I-625 (0.104)
11	C1018 Ni (0.302)	316L (0.216)	316L SS (0.167)	410 (0.150)	A53-B (0.131)	A53-B (0.126)
12	410 (0.314)	C1018 Ni (0.351)	C1018 Ni (0.28)	C1018 Ni (0.216)	C1018 Ni (0.231)	C1018 Ni (0.256)

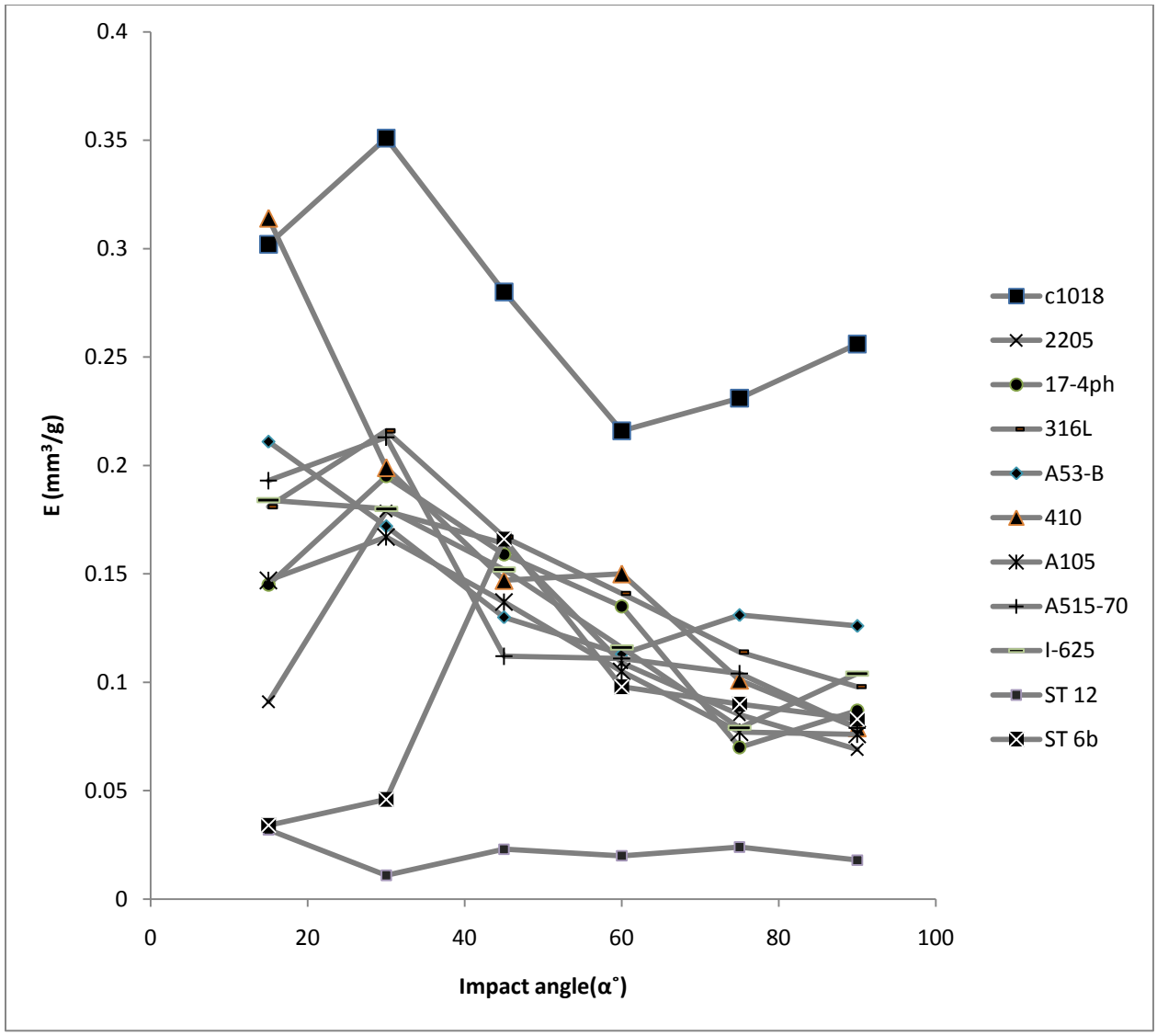

Figure 5- 7: Comparison of measured erosion rates for 11 candidate materials for 130 m.s^{-1} and d= 6.9 µm, α= 15˚, 30˚, 45˚, 60˚, 75˚, and 90˚. Legend indicates: c1018- A1018 carbon steel nickel plating; 2205- A240 Type 2205 duplex stainless steel plate; 17-4ph- 17-4 PH stainless steel plate; 316L- Type 316L stainless steel; A53-B- A53 Gr. B steel; 410- A240 Type 410 stainless steel plate; A105- A105 carbon steel forging, A515-70- A515 Gr. 70 norm. plate; I-625- Alloy 625 plate; ST12- Solid Stellite 12; ST6b- Solid Stellite 6. The lines are only to guide the eye.

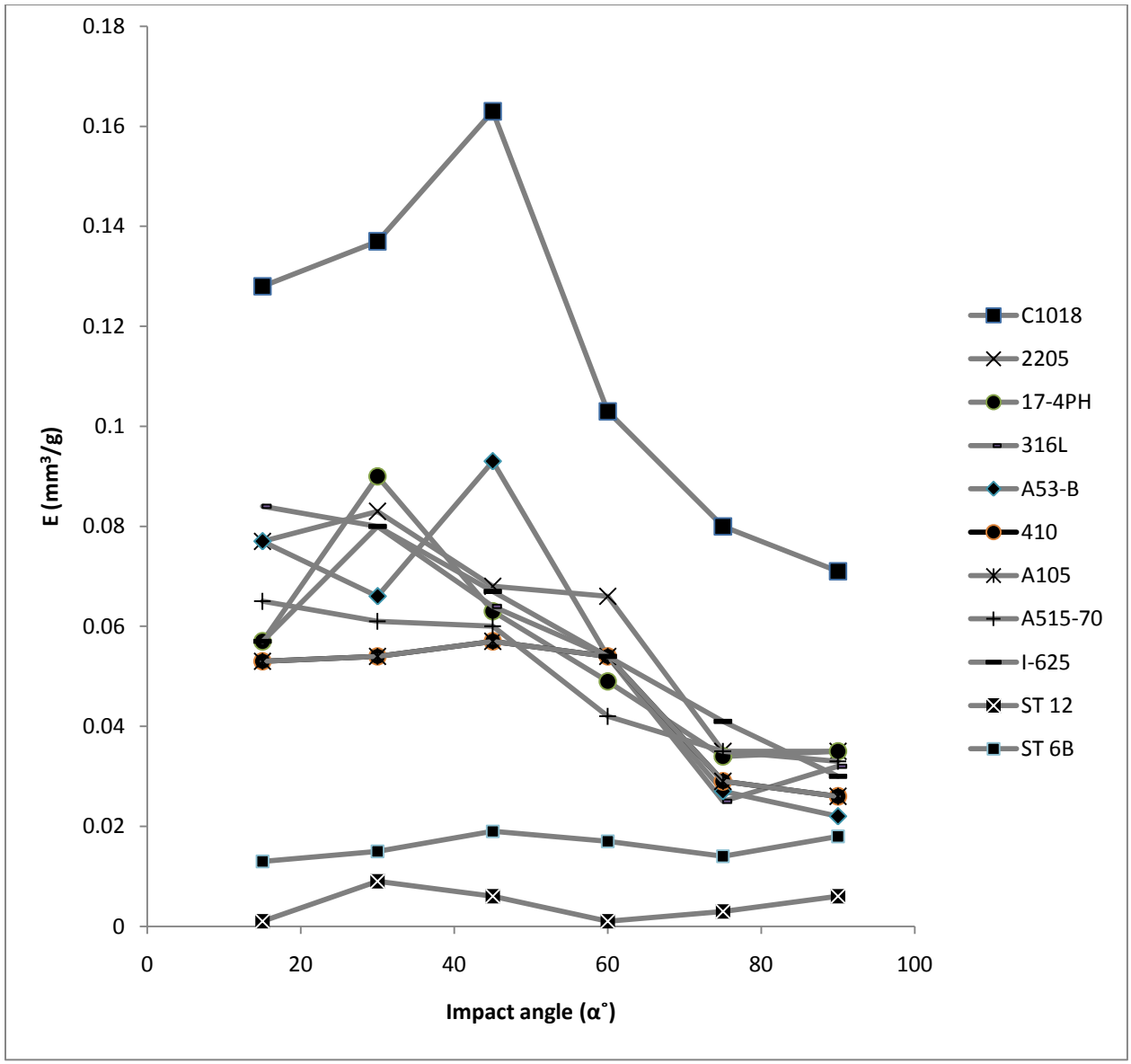

Figure 5- 8: Comparison of measured erosion rates for 11 candidate materials for 90 m.s^{-1} and d= 6.9 µm, α= 15˚, 30˚, 45˚, 60˚, 75˚, and 90˚. Legend indicates: c1018- A1018 carbon steel nickel plating; 2205- A240 Type 2205 duplex stainless steel plate; 17-4ph- 17-4 PH stainless steel plate; 316L- Type 316L stainless steel; A53-B- A53 Gr. B steel; 410- A240 Type 410 stainless steel plate; A105- A105 carbon steel forging, A515-70- A515 Gr. 70 norm. plate; I-625- Alloy 625 plate; ST12- Solid Stellite 12; ST6b- Solid Stellite 6b. The lines are only to guide the eye.

Table 5- 2: Erosion resistance rankings of 12 candidate materials for low particle velocity (90 m/s) erosion rate experiments. Rankings are from most (1) to least (12) erosion resistant. Volumetric erosion rates under each condition (mm^3/g) are shown in parenthesis

Rank	**Impingement Angle, α and Erosion Rate (mm^3/g)**					
	15°	**30°**	**45°**	**60°**	**75°**	**90°**
1	WC (0)	WC (0)	WC (0)	WC (0)	WC (0)	WC (0)
2	ST. 12 (0.001)	ST. 12 (0.009)	ST. 12 (0.006)	ST. 12 (0.001)	ST. 12 (0.003)	ST. 12 (0.006)
3	ST. 6B (0.003)	ST. 6B (0.015)	ST. 6B (0.019)	ST. 6B (0.017)	ST. 6B (0.004)	ST. 6B (0.018)
4	A53-B (0.077)	2205 (0.083)	2205 (0.068)	A515-70 (0.042)	316L (0.025)	A53-B (0.022)
5	A515-70 (0.065)	A105 (0.061)	17-4PH (0.063)	A105 (0.042)	A105 (0.026)	410 (0.026)
6	I-625 (0.057)	A53-B (0.066)	A515-70 (0.060)	17-4PH (0.049)	A53-B (0.027)	A105 (0.028)
7	17-4PH (0.057)	A515-70 (0.061)	A105 (0.059)	410 (0.054)	17-4PH (0.034)	I-625 (0.03)
8	A105 (0.072)	I-625 (0.08)	316L (0.064)	A53-B (0.054)	A240-410 (0.027)	316L (0.032)
9	410 (0.053)	410 (0.054)	410 (0.057)	316L (0.054)	A515-70 (0.035)	A515-70 (0.033)
10	2205 (0.077)	316L (0.08)	I-625 (0.067)	410 (0.054)	2205 (0.035)	17-4PH (0.035)
11	C1018 Ni (0.128)	C1018 Ni (0.137)	C1018 Ni (0.163)	2205 (0.066)	I-625 (0.041)	A240-2205 (0.035)
12	316L (0.084)	17-4PH (0.09)	A53-B (0.093)	C1018Ni (0.103)	C1018 Ni (0.08)	C1018 Ni (0.071)

In most of the cases, the maximum erosion rate occurred at shallow to intermediate angles of attack in both cases, indicating a typically ductile erosive response. The SEM

photographs from the periphery of the surface of blasted specimens (Figure 5-5) support the existence of a ductile erosive process. However Figure 5-9 (a) and (b) for the A1018 Carbon steel nickel plating at 130 $m.s^{-1}$ shows an unusual transition from brittle to ductile behavior. This can be seen when comparing the erosion rate at $\alpha = 75^{\circ}$ to that $\alpha = 90^{\circ}$, which shows in figure 5-7. The SEM in Figure 5-9 (a) shows that there was indeed likely a transition. These are 'brittle erosion behavior' which shows monotonically rises with angle to a maximum value at around normal incidence and this is implying material removal by brittle fracture. In the brittle erosion mechanism, the material is mostly removed by crack formation, and the maximum erosion occurs at a 90° impact angle. The existence of a hardened layer could act as an initiative for transferring the ductile erosion mechanism to a brittle mechanism. It was caused that the erosive wear peak to move from about a 30° to about an 80° impingement angle and even wear significantly to the extent that it resulted in a dramatic increase in erosive wear rates. Since crack formation is rapid, the brittle mode of erosion can be a very destructive form of wear. During this process, the surface work hardened and evevually falls in a brittle manner. All these observations show that for a better understanding of micro-mechanisms responsible for material removal during erosion, the effect of size of particles should be implemented in an erosion model. Figures 5-9 (c) and (d), for Type 316L stainless steel using 6.9 μm powders, show the typical cutting and ploughing mechanisms associated with the fundamental mechanisms of ductile erosion. Besides the ability of angular particles to cut a chip of material from target surface when impacted with an appropriate orientation at shallow angle, ploughing is the mechanism which leads to material removal.

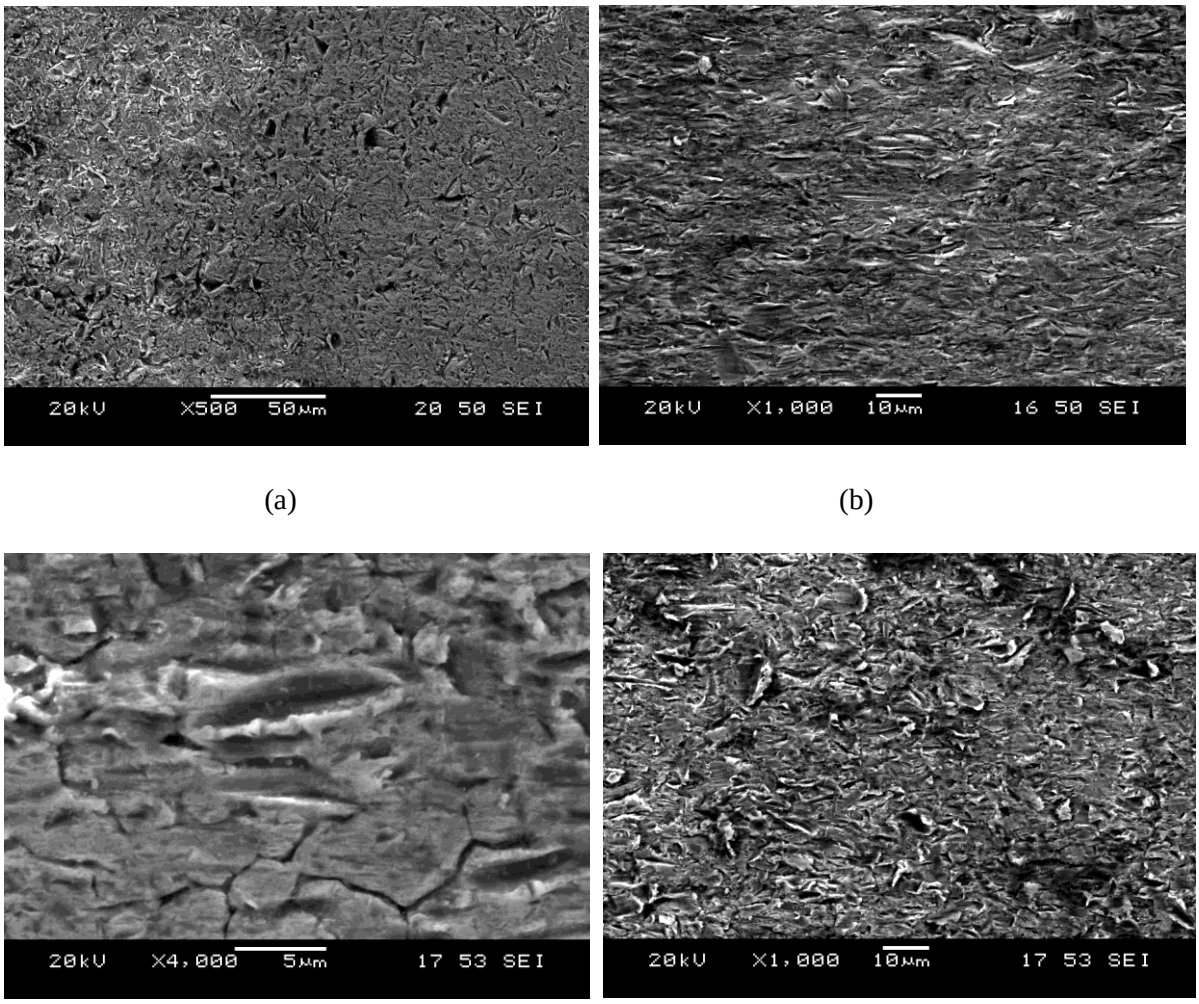

Figure 5- 9: SEM micrograph taken from erosion scar on (a) periphery of A1018 Carbon steel nickel plating eroded with 6.9 µm powder at 130 m.s-1, α= 90˚ for a dwell time of 120 s (b) periphery of A1018 Carbon steel nickel plating eroded with 6.9 µm powder at 130 m.s-1, α= 15˚ for a dwell time of 15 s (c) periphery of 316L stainless steel eroded with 6.9 µm powder at 130 m.s^{-1}, α= 15˚ for a dwell time of 120 s (d) periphery of 316L stainless steel eroded with 6.9 µm powder at 130 m.s^{-1}, α= 15˚ for a dwell time of 120 s at lower magnification

In some cases (e.g. 410, A53 B), the maximum erosion rate was found at 15˚ for both velocities. It is impossible to determine whether this value represents the maximum erosion rate, because of the difficulty in performing experiments at α < 15˚, but based on what has seen in the literature [63], it is unlikely that the maximum in erosion rate would be at α < 15˚.

The maximum erosion crater depths ranged from 11 μm for the Stellite 12 to 294 μm for the 316L stainless steel at 130 $m.s^{-1}$, and from 10 μm for the Solid Stellite 12 to 203 μm for the Type 316L stainless steel at 90 $m.s^{-1}$. These depths were far below the suggested maximum depth of 350 μm noted in ASTM G76-07 [8]. For the nickel coated A1018 steel, the least erosion resistant material, the maximum depth was 90 μm at 130 $m.s^{-1}$, and 63 μm at 90 $m.s^{-1}$, indicating that the erosion rate measurement occurred within the 100 μm thick nickel coating.

Tables 5-1 and Table 5-2 rank the erosion resistance of the candidate materials at each angle of attack for both incident velocities. There was no measurable material removal for the tungsten carbide samples at any angle or velocity for dwell times up to 400 s at either velocity. Stellite 12 also was found to be highly erosion resistant, exhibiting the second highest erosion resistance at all angles of attack. Although longer blasting times were used in the tests of Stellite 6b and Stellite 12, the craters were not sufficiently deep to obtain very reliable estimates of volume removal, and the very low measured erosion rates cannot be considered to be highly accurate. The maximum uncertainty for erosion rate measurements in Stellite 6b was observed to be 0.076±0.009 when measured at 30˚ angle of impact and 130 $m.s^{-1}$particle velocity and 0.024±0.003 when measured at 30˚ angle of impact and 90 $m.s^{-1}$particle velocity. The maximum uncertainty on erosion rate measurements on Stellite 12 observed for 0.035±0.004 when measured at 60˚ angle of impact and 130 $m.s^{-1}$particle velocity and 0.0098±0.004 when measured at 45˚ angle of impact and 90 $m.s^{-1}$particle velocity.

5.2 MEASURED EROSION RATES AND POSSIBLE MECHANISMS: 30.4 MICRON PARTICLE SIZE

An acceptable linear relationship was observed between the volume removed and abrasive mass used for the plots used in the determination of the erosion rates at steady state. As with the finer powder discussed in Section 5.1, some of the linear fits did not pass through the origin, indicating the presence of a two-stage erosion process. In all cases, the erosion rate was been reported as the best fit linear line, regardless of whether it passed through the origin or not (i.e. the steady-state erosion rate).

Figures 5-10 and 5-11 show the same data plotted in terms of dimensionless erosion rate (g/g), presented in Tables 1 and 2 of Appendix D, along with the curve fit values using the model of Oka et al. [1]. Figures 5-12 and 5-13 show the measured volumetric (mm^3/g) erosion rates for the 6.9 μm powder blasted at 130 $m.s^{-1}$ and 90 $m.s^{-1}$, respectively. The volumetric erosion rates at 130 $m.s^{-1}$ particle velocities were between 1.8 and 2.5 times larger than those measured at 90 $m.s^{-1}$. In most cases, the maximum erosion rate occurred at shallow to intermediate angles of attack, indicating a typically ductile erosive response. Several SEM photographs of blasted surface of candidate specimens confirmed this behavior (Figure 5-14). In some cases (e.g. 316 L, A53 B), the maximum erosion rate was found at 15˚ for v= 90 $m.s^{-1}$. Because of the difficulty in performing experiments at $\alpha < 15°$, it is unfortunately impossible to know whether the maximum erosion rate was reached; however, as noted in Section 5.1, it would be highly unusual to find a maximum at angles less than 15°.

Tables 5-3 and 5-4 rank the erosion resistance of the candidate materials at each angle of attack for both velocity experiments. The maximum erosion crater depths ranged from 11 μm

for the Solid Stellite 12 to 177 μm for the type 316L stainless steel at 130 $m.s^{-1}$, and from 11 μm for the Solid Stellite 12 to 128 μm for the Alloy 625 plate at 90 $m.s^{-1}$. These depths were far below the suggested maximum depth of 350 μm noted in ASTM G76-07 [8]. For the nickel coated A1018 steel, the least erosion resistant material, the maximum depth of the crater was 33 μm at 130 $m.s^{-1}$, and 28 μm for 90 $m.s^{-1}$, indicating that the erosion rate measurement occurred within the 100 μm thick nickel coating. There was no measurable material removal for the tungsten carbide samples at any angle or velocity for dwell times up to 400 s. at either particle velocity. Stellite 12 also was found to be highly erosion resistance, exhibiting the second highest erosion resistance at all angles of attack. As was the case with the finer powder (Section 5.1), for the erosion rate results for Stellite 6b and Stellite 12 can be considered to be of lower accuracy than the other materials because of the extremely low measured crater volumes. The maximum uncertainty for erosion rate measurements in Stellite 6b was observed to be 0.035±0.0024 when measured at 60˚ angle of impact and 130 $m.s^{-1}$particle velocity and 0.011±0.002 when measured at 30˚ angle of impact and 90 $m.s^{-1}$particle velocity. However, the maximum uncertainty on erosion rate measurements in Stellite 12 was observed for 0.014±0.001 when measured at 90˚ angle of impact and 130 $m.s^{-1}$particle velocity and 0.003±0.00095 when measured at 90˚ angle of impact and 90 $m.s^{-1}$particle velocity.

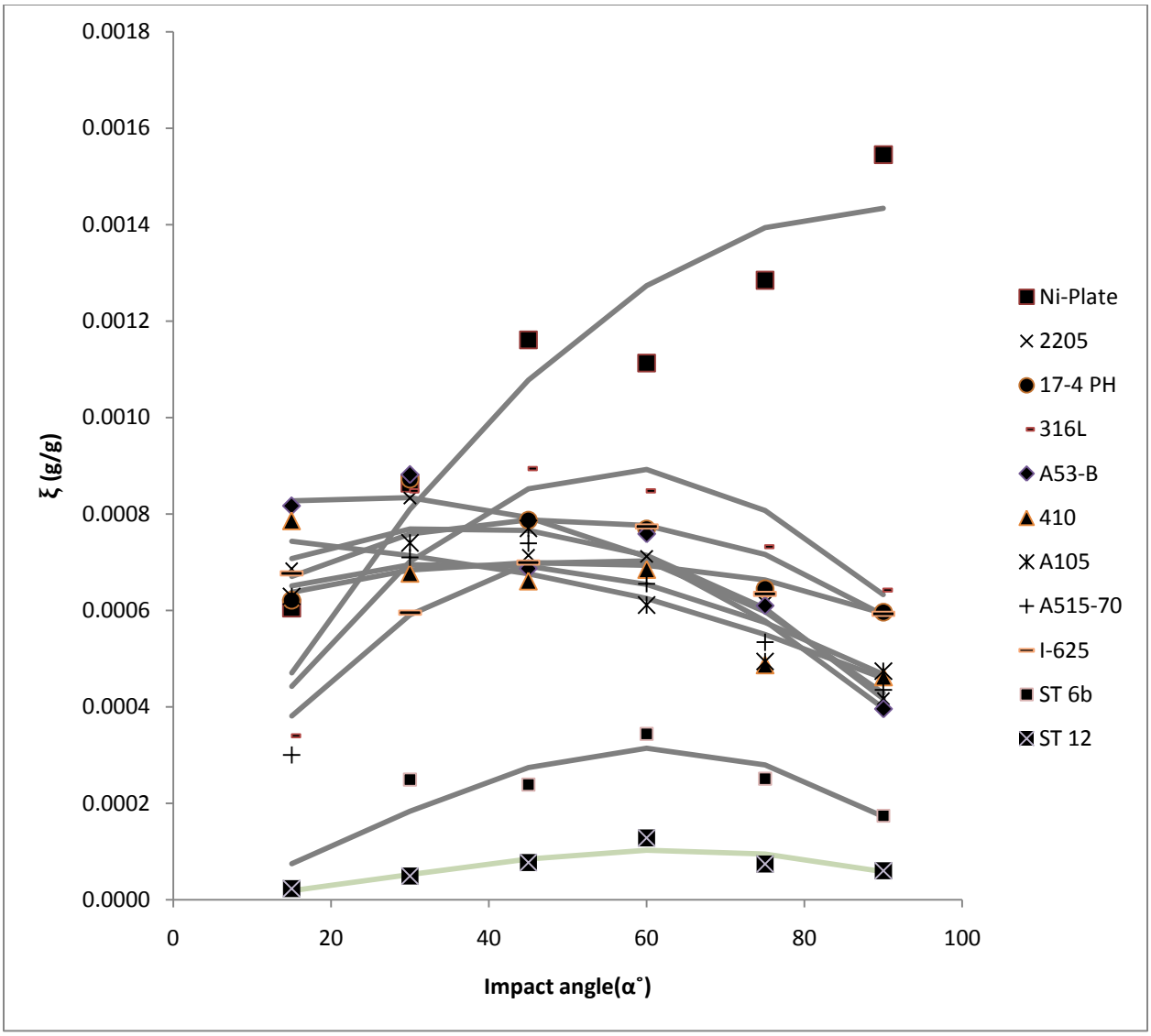

Figure 5-10: Comparison of measured (points) and curve fit (lines) dimensionless erosion rates for candidate materials for 130 m.s^{-1} and d= 30.4 µm. Legend indicates: Ni Plate- Nickel plating on A1018 carbon steel supporting substrate; 2205- A240 Type 2205 duplex stainless steel plate; 17-4ph- 17-4 PH stainless steel plate; 316L- Type 316L stainless steel; A53-B- A53 Gr. B steel; 410- A240 Type 410 stainless steel plate; A105- A105 carbon steel forging, A515-70- A515 Gr. 70 norm. plate; I-625- Alloy 625 plate; ST12- Solid Stellite 12; ST6b- Solid Stellite 6b

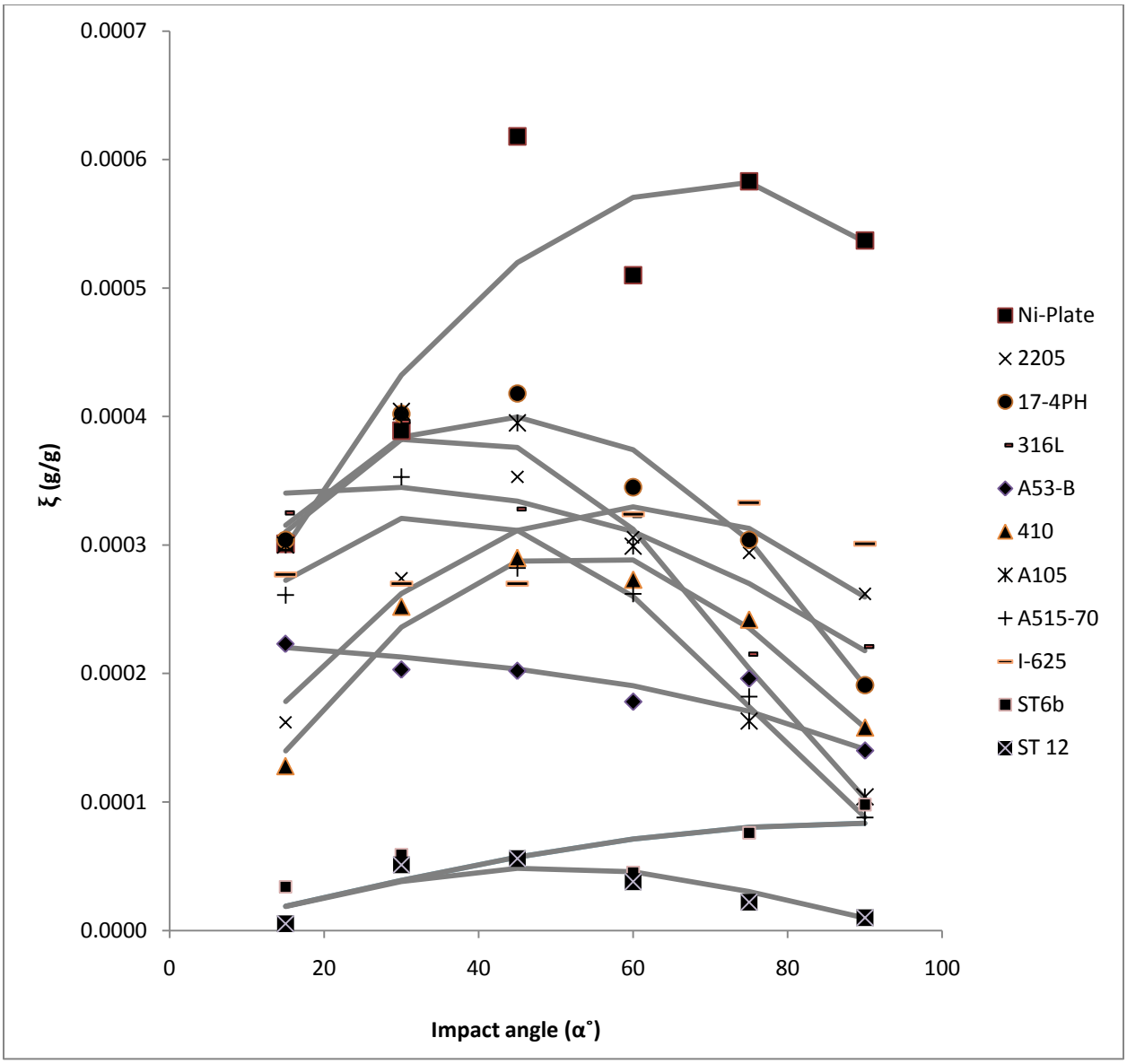

Figure 5- 11: Comparison of measured (points) and curve fit (lines) dimensionless erosion rates for candidate materials for 90 m/s and d= 30.4 µm. Legend indicates: Ni Plate - Nickel plating on A1018 carbon steel supporting substrate; 2205- A240 Type 2205 duplex stainless steel plate; 17-4ph- 17-4 PH stainless steel plate; 316L- Type 316L stainless steel; A53-B- A53 Gr. B steel; 410- A240 Type 410 stainless steel plate; A105- A105 carbon steel forging, A515-70- A515 Gr. 70 norm. plate; I-625- Alloy 625 plate; ST12- Solid Stellite 12; ST6b- Solid Stellite 6b

Table 5- 3: Erosion resistance rankings of 12 candidate materials for high particle velocity (130 m.s^{-1}) erosion rate experiments. Rankings are from most (1) to least (12) erosion resistant. Erosion rates under each condition (mm^3/g) are shown in parenthesis

Rank	Impingement Angle, α and Erosion Rate (mm^3/g)					
	15°	**30°**	**45°**	**60°**	**75°**	**90°**
1	WC (0)	WC (0)	WC (0)	WC (0)	WC (0)	WC (0)
2	ST. 12 (0.002)	ST. 12 (0.005)	ST. 12 (0.009)	ST. 12 (0.015)	ST. 12 (0.008)	ST. 12 (0.007)
3	ST. 6B (0.002)	ST. 6B (0.029)	ST. 6B (0.028)	ST. 6B (0.041)	ST. 6B (0.029)	ST. 6B (0.02)
4	A515-70 (0.038)	I-625 (0.07)	I-625 (0.082)	A105 (0.077)	A105 (0.062)	A53-B (0.05)
5	316L (0.043)	410 (0.087)	410 (0.085)	A515-70 (0.083)	410 (0.062)	2205 (0.052)
6	C1018 Ni (0.068)	A515-70 (0.09)	A53-B (0.087)	410 (0.088)	A515-70 (0.068)	A515-70 (0.055)
7	I-625 (0.079)	A105 (0.094)	2205 (0.09)	2205 (0.09)	I-625 (0.075)	410 (0.059)
8	A105 (0.08)	C1018 Ni (0.097)	A515-70 (0.094)	I-625 (0.091)	A53-B (0.077)	A105 (0.06)
9	17-4PH (0.08)	2205 (0.105)	A105 (0.098)	A53-B (0.097)	2205 (0.078)	I-625 (0.07)
10	2205 (0.087)	316L (0.106)	17-4PH (0.101)	17-4PH (0.099)	17-4PH (0.083)	17-4PH (0.077)
11	410 (0.101)	A53-B (0.112)	316L (0.112)	316L (0.106)	316L (0.091)	316L (0.08)
12	A53-B (0.104)	17-4PH (0.112)	C1018 Ni (0.131)	C1018 Ni (0.125)	C1018 Ni (0.145)	C1018 Ni (0.174)

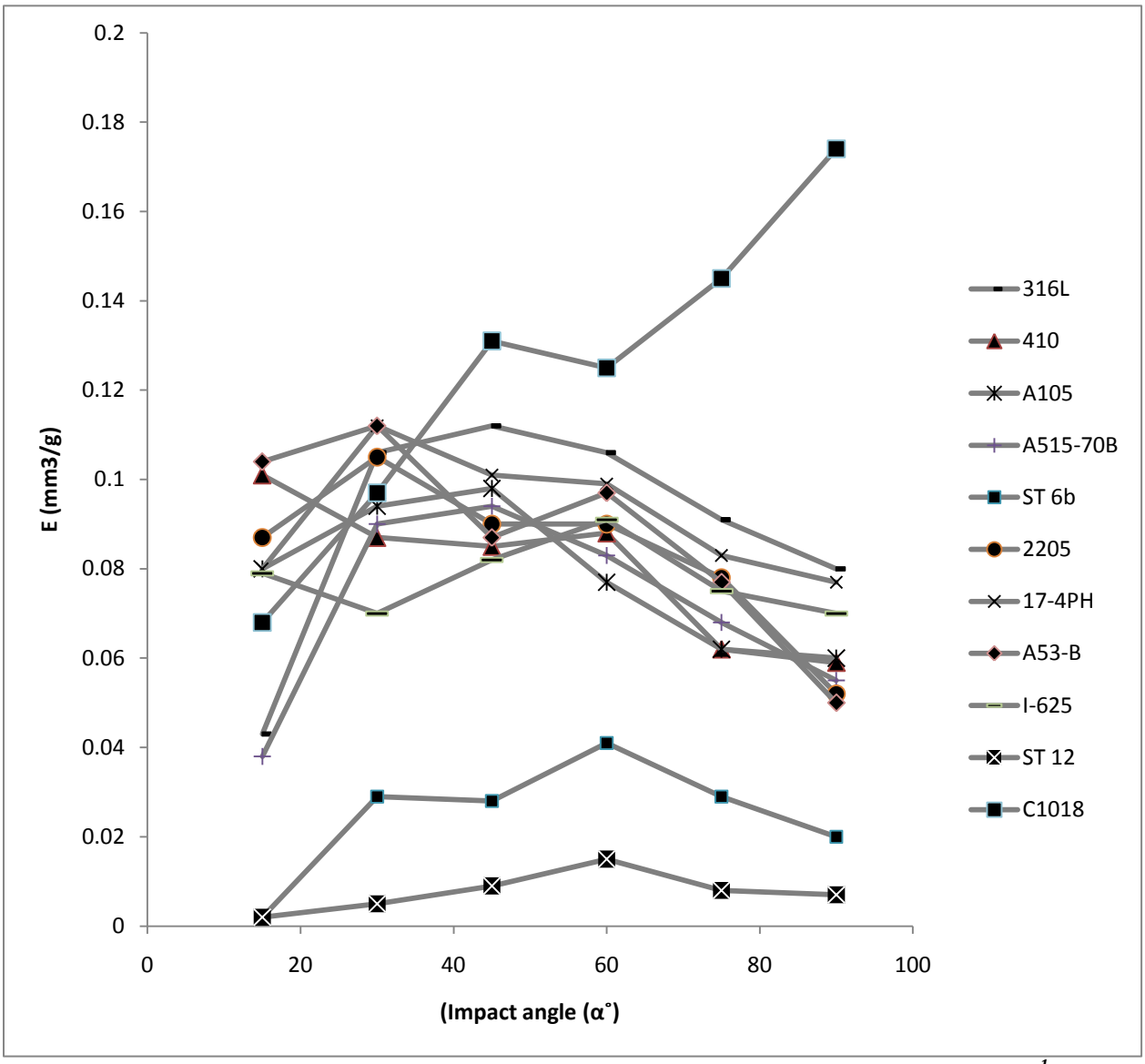

Figure 5- 12: Comparison of measured erosion rates for 11 candidate materials for 130 m.s^{-1} and d= 30.4 µm, α= 15°, 30°, 45°, 60°, 75°, and 90°. Legend indicates: c1018- A1018 carbon steel nickel plating; 2205- A240 Type 2205 duplex stainless steel plate; 17-4ph- 17-4 PH stainless steel plate; 316L- Type 316L stainless steel; A53-B- A53 Gr. B steel; 410- A240 Type 410 stainless steel plate; A105- A105 carbon steel forging, A515-70- A515 Gr. 70 norm. plate; I-625- Alloy 625 plate; ST12- Solid Stellite 12; ST6b- Solid Stellite 6b. Tungsten Carbide gave zero erosion rate at all angles of attack. The lines are to guide the eye.

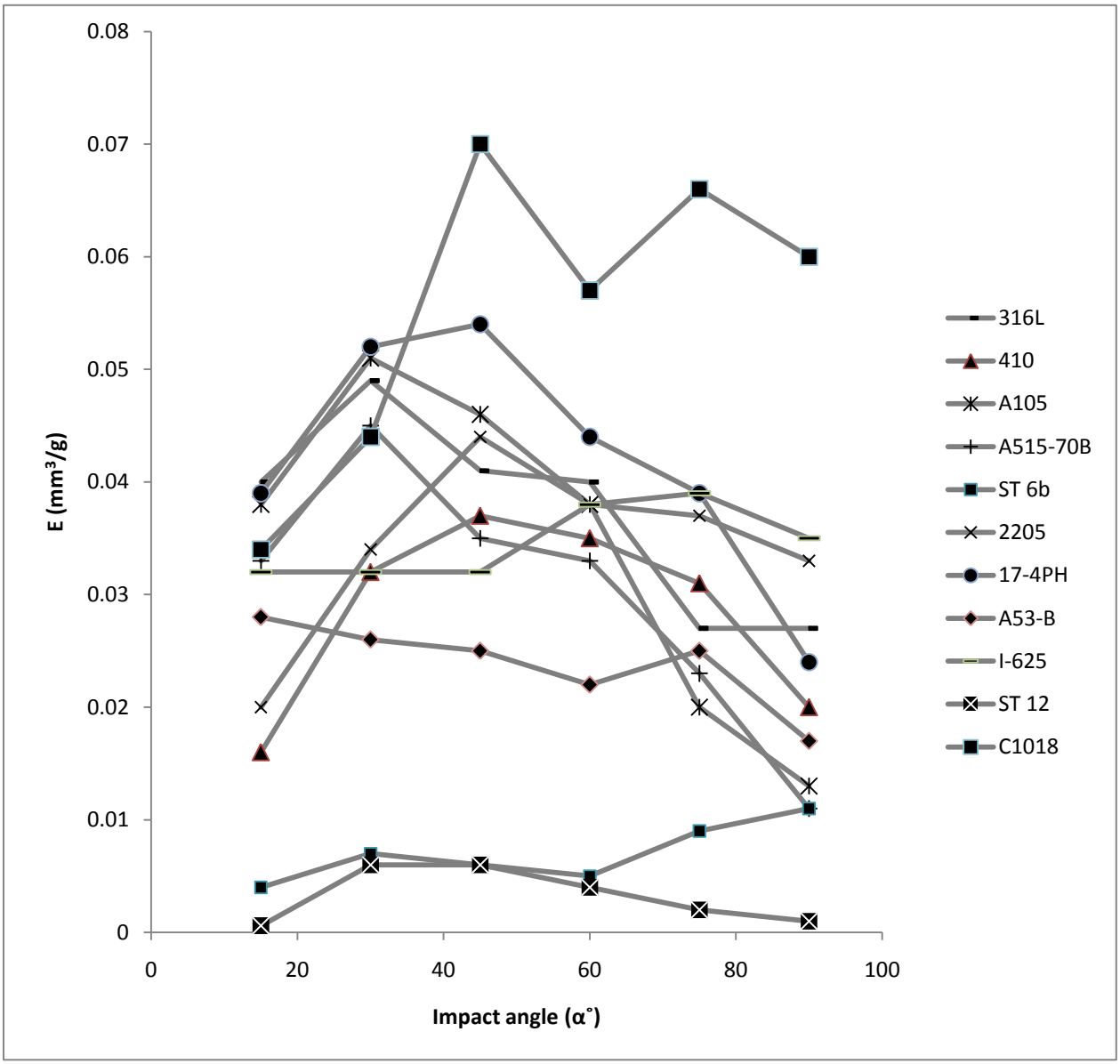

Figure 5- 13: Comparison of measured erosion rates for 11 candidate materials for 90 m/s and d= 30.4 µm, α= 15°, 30°, 45°, 60°, 75°, and 90°. Legend indicates: c1018- A1018 carbon steel nickel plating; 2205- A240 Type 2205 duplex stainless steel plate; 17-4ph- 17-4 PH stainless steel plate; 316L- Type 316L stainless steel; A53-B- A53 Gr. B steel; 410- A240 Type 410 stainless steel plate; A105- A105 carbon steel forging, A515-70- A515 Gr. 70 norm. plate; I-625- Alloy 625 plate; ST12- Solid Stellite 12; ST6b- Solid Stellite 6b. Tungsten Carbide gave zero erosion rate at all angles of attack. The lines are to guide the eye.

Table 5- 4: Erosion resistance rankings of 12 candidate materials for low particle velocity (90 m.s^{-1}) erosion rate experiments. Rankings are from most (1) to least (12) erosion resistant. Erosion rates under each condition (mm3/g) are shown in parenthesis

Rank	Impingement Angle, α and Erosion Rate (mm^3/g)					
	15°	**30°**	**45°**	**60°**	**75°**	**90°**
1	WC (0)	WC (0)	WC (0)	WC (0)	WC (0)	WC (0)
2	ST. 12 (0.0006)	ST. 12 (0.006)	ST. 12 (0.006)	ST. 12 (0.004)	ST. 12 (0.002)	ST. 12 (0.001)
3	ST. 6B (0.004)	ST. 6B (0.007)	ST. 6B (0.006)	ST. 6B (0.005)	ST. 6B (0.009)	ST. 6B (0.011)
4	410 (0.016)	A53-B (0.026)	A53-B (0.025)	A53-B (0.022)	A105 (0.02)	A515-70 (0.011)
5	2205 (0.02)	410 (0.032)	I-625 (0.032)	A515-70 (0.033)	A515-70 (0.023)	A105 (0.013)
6	A53-B (0.028)	I-625 (0.032)	A515-70 (0.035)	410 (0.035)	A53-B (0.025)	A53-B (0.017)
7	I-625 (0.032)	2205 (0.034)	410 (0.037)	2205 (0.038)	316L (0.027)	410 (0.02)
8	A515-70 (0.033)	C1018 Ni (0.044)	316L (0.041)	I-625 (0.038)	410 (0.031)	17-4PH (0.024)
9	C1018 Ni (0.034)	A515-70 (0.045)	2205 (0.044)	A105 (0.038)	2205 (0.037)	316L (0.027)
10	A105 (0.038)	316L (0.049)	A105 (0.046)	316L (0.04)	17-4PH (0.039)	2205 (0.033)
11	17-4PH (0.039)	A105 (0.051)	17-4PH (0.054)	17-4PH (0.044)	I-625 (0.039)	I-625 (0.035)
12	316L (0.04)	17-4PH (0.052)	C1018 Ni (0.07)	C1018 Ni (0.057)	C1018 Ni (0.066)	C1018 Ni (0.06)

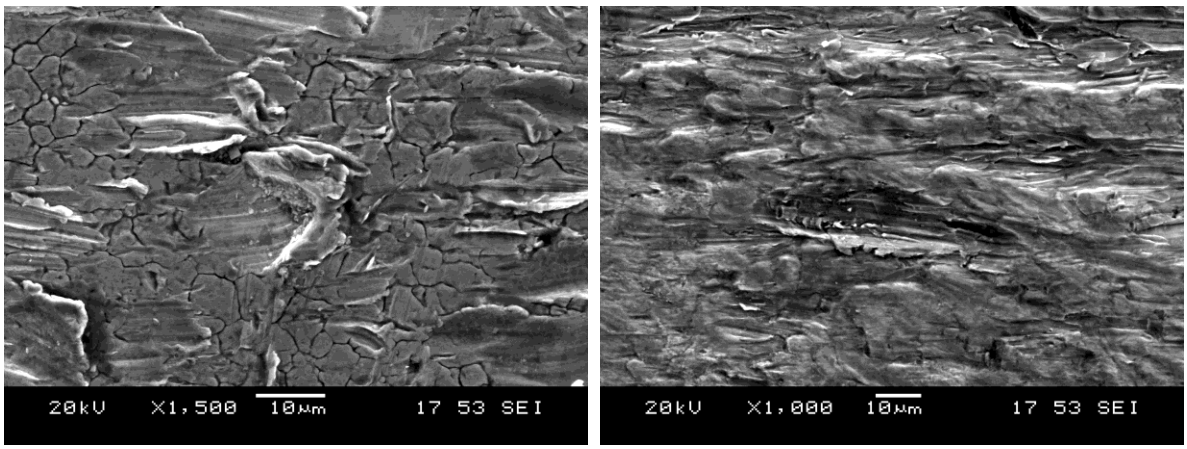

(a) (b)

Figure 5-14: (a) SEM micrograph taken from periphery of erosion scar on 316 stainless steel eroded with 30.4 µm powder at 90 m.s^{-1}, α= 15˚ for a dwell time of 180 s; (b) SEM micrograph taken from periphery of erosion scar on Stellite 12 eroded with 30.4 µm powder at 130 m.s^{-1}, α= 15˚ for a dwell time of 120 s.

The SEM photographs from the periphery of the surface of blasted specimens (Figure 5-14) support the existence of a ductile erosive process. However Figure 5-15 (a) and (b) for the A1018 Carbon steel nickel plated at 130 m.s^{-1} shows an unusual transition from ductile to brittle behavior. This can be seen when comparing the erosion rate at α= 15˚ to that α= 90˚, which shows in figure 5-12. Unlike to lower velocity case for this material, these results imply that a harder hardened layer was formed in the case of the experiments with the larger particles, possibly due to the higher associated incident particle kinetic energies and higher particle velocity. The SEM in Figure 5-15 (a) shows that there was indeed likely a transition. Figures 5-14 (a) and (b), for Type 316L stainless steel using 30.4 µm powders, show the typical cutting and ploughing mechanisms associated with the fundamental mechanisms of ductile erosion.

All these observations show that for a better understanding of micro-mechanisms responsible for material removal during erosion, the effect of size of particles should be implemented in an erosion model.

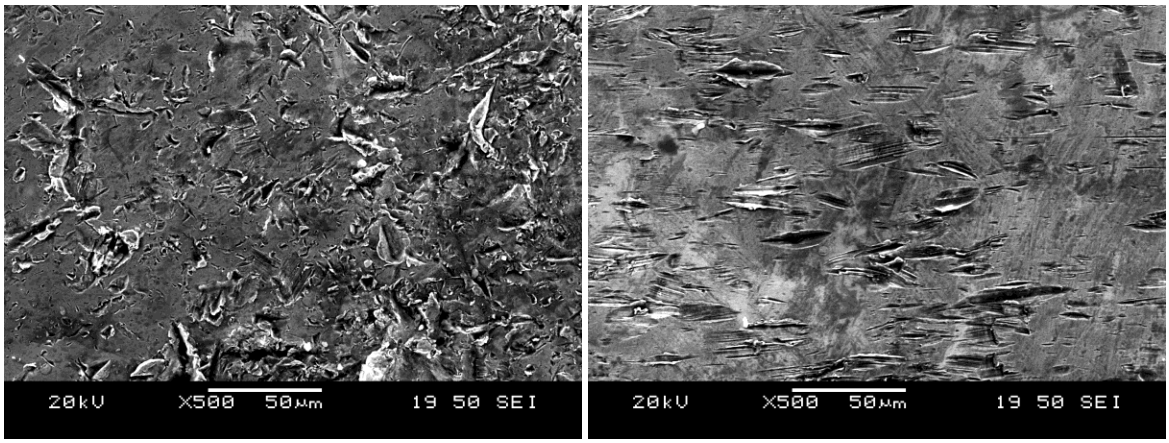

(a) **(b)**

Figure 5- 15: (a) SEM micrograph taken from periphery of erosion scar on A1018 Carbon steel nickel plating eroded with 30.4 µm powder at 130 m.s^{-1}, α= 90˚ for a dwell time of 15 s; (b) SEM micrograph taken from periphery of erosion scar on A1018 Carbon steel nickel plating eroded with 30.4 µm powder at 130 m.s^{-1}, α= 15˚ for a dwell time of 15 s.

5.3 GOODNESS OF FIT

In order to assess the fit of the model due to Oka et al. [1] (Section 4.3) to the experimental erosion rates, the goodness of fits were evaluated.

Mathematically, the residual for a specific predictor value is the difference between the response value *y* and the predicted response value. The sum of squares due to error (SSE) and the R-square statistics were used (Table 5-5). The SSE statistic measures the total deviation of the response values from the fit to the response values. It is also called the summed square of residuals [73]:

$$SSE = \sum_{i=1}^{n} \omega_i (y_i - \hat{y}_i)^2 \tag{5.1}$$

where y_i is the response value, $\hat{y}_i$ is the predicted response value, and w_i is the variable reference to matrix. SSE value closer to 0 indicates that the model has a smaller random error component,

and that the fit will be more useful for prediction. R-square is the square of the correlation between the response values and the predicted response values, and it measures how successful the fit is in explaining the variation of the data. It is also called the square of the multiple correlation coefficients and the coefficient of multiple determinations. R-square is defined as the ratio of the sum of squares of the regression (SSR) and the total sum of squares (SST). SSR is defined as [73]:

$$SSR = \sum_{i=1}^{n} \omega_i (\hat{y}_i - \bar{y}_i)^2 \tag{5.2}$$

SST is also called the sum of squares about the mean, and is defined as [73]:

$$SST = \sum_{i=1}^{n} \omega_i (y_i - \bar{y}_i)^2 \tag{5.3}$$

where SST = SSR + SSE. Given these definitions, R-square is expressed as [73]:

$$R - square = \frac{SSR}{SST} = 1 - \frac{SSE}{SST} \tag{5.4}$$

R-square can take on any value between 0 and 1, with a value closer to 1 indicating that a greater proportion of variance is accounted for by the model. For example, an R-square value of 0.8234 means that the fit explains 82.34% of the total variation in the data about the average.

Most of the R-Squared values were very close to zero, indicating a good fit, although there were some relatively poor fits (e.g. A1018). These poor fits are likely due to the higher degree of associated experimental error when measuring the erosion rates on these extremely

hard materials; i.e. the resulting very low volume removal was at the limits of detect ability of the optical profilometer. The poor fit of A1018 nickel plate was due to a single outlier in the data. Similar outliers can be seen for other materials as well, usually at the 15˚ angle of incidence where the error in the measured erosion rate is amplified due to difficulties in determining the volume removed at the periphery of the shallow scars. Elimination of these outliers from the curve fit, or more erosion rate measurements at the 15˚ angle of attack would likely result in a much better fit.

Table 5- 5: SSE and R^2 statistics on the goodness of fit

Materials	**Goodness of fit**	**Experimental Conditions**			
		V= 130 (m/s) d= 30.4 (µm)	**V= 90 (m/s) d= 30.4 (µm)**	**V= 130 (m/s) d= 6.9 (µm)**	**V= 90 (m/s) d= 6.9 (µm)**
A1018 Carbon Steel With Ni-Plate	SSE	7.799×10^{-8}	1.517×10^{-8}	1.019×10^{-6}	1.784×10^{-7}
	R^2	8.58×10^{-1}	7.92×10^{-1}	0.63×10^{-2}	5.91×10^{-1}
A240 Type 2205 Duplex Stainless Steel	SSE	7.435×10^{-9}	3.067×10^{-9}	1.461×10^{-7}	1.461×10^{-7}
	R^2	9.24×10^{-1}	8.40×10^{-1}	7.18×10^{-1}	9.54×10^{-1}
17-4 PH Stainless Steel Plate	SSE	2.054×10^{-8}	1.645×10^{-9}	2.219×10^{-7}	2.32×10^{-8}
	R^2	6.74×10^{-1}	9.59×10^{-1}	7.57×10^{-1}	8.8×10^{-1}
Type 316L Stainless Steel	SSE	4.141×10^{-8}	6.069×10^{-9}	1.43×10^{-7}	1.363×10^{-8}
	R^2	8.06×10^{-1}	7.89×10^{-1}	8.88×10^{-1}	9.19×10^{-1}
A53 Gr. B Steel	SSE	1.685×10^{-8}	9.113×10^{-10}	7.506×10^{-8}	1.41×10^{-8}
	R^2	8.8×10^{-1}	7.7×10^{-1}	7.86×10^{-1}	9.05×10^{-1}
A240 Type 410 Stainless Steel Plate	SSE	1.099×10^{-8}	6.762×10^{-10}	2.483×10^{-7}	3.24×10^{-9}
	R^2	8.63×10^{-1}	9.61×10^{-1}	7.86×10^{-1}	9.45×10^{-1}
A105 Carbon Steel Forging	SSE	1.716×10^{-8}	2.777×10^{-9}	2.865×10^{-8}	9.761×10^{-9}
	R^2	7.61×10^{-1}	9.63×10^{-1}	9.47×10^{-1}	9.23×10^{-1}
A515 Gr. 70 Norm. Plate	SSE	2.889×10^{-8}	2.097×10^{-9}	3.149×10^{-8}	1.012×10^{-8}
	R^2	8.04×10^{-1}	9.57×10^{-1}	9.42×10^{-1}	9.2×10^{-1}
Alloy 625 Plate	SSE	1.677×10^{-8}	2.338×10^{-9}	6.17×10^{-8}	3.11×10^{-8}
	R^2	3.06×10^{-1}	3.99×10^{-1}	8.64×10^{-1}	8.69×10^{-1}
Solid Stellite 6b	SSE	1.002×10^{-9}	1.554×10^{-9}	3.217×10^{-7}	1.461×10^{-8}
	R^2	8.28×10^{-1}	4.04×10^{-2}	6.16×10^{-1}	1.48×10^{-2}
Solid Stellite 12	SSE	1.187×10^{-9}	5.375×10^{-10}	1.662×10^{-9}	1.14×10^{-9}
	R^2	8.07×10^{-1}	7.63×10^{-1}	7.96×10^{-1}	6.04×10^{-1}

5.4 CURVE FIT OF HARDNESS AND IMPLICATIONS FOR EFFECT OF PARTICLE SIZE

Figures 5-16 (a) to (d) compare the as-received Vickers hardness values (gray bars) and the hardness values parameter (HV) (black bars) generated in the curve fitted equation for each material and condition (two velocities, two particle sizes).

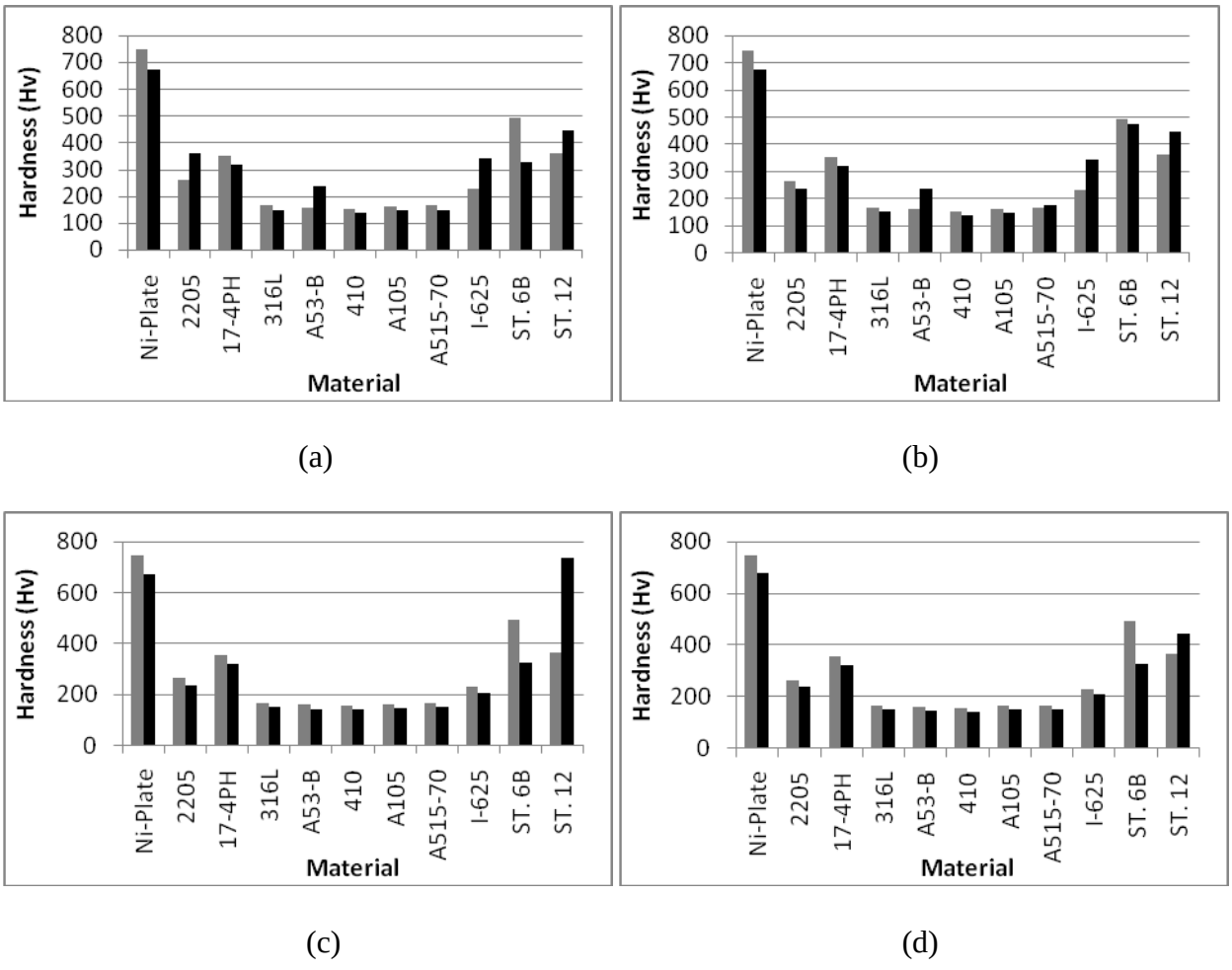

Figure 5-16: Comparison of bulk measured (Gray bars) and curve fit (Black bars) Vickers Hardness for candidate materials for (a) v=130 m.s^{-1} and d= 30.4 µm; (b) v=90 m.s^{-1} and d= 30.4 µm; (c) v=130 m.s^{-1} and d= 6.9 µm; (d) v=90 m.s^{-1} and d= 6.9 µm

In all cases, the hardness parameters were constrained to be in the range -10% to +50% of their as-received values. As a result, the fitted values are relatively close to the as-received

values. In some cases, the fitted value is lower than the as-received value. However, in other cases, the opposite is true. In the cases where the fitted hardness values are larger than the as-received, it is interesting to note that, for the same velocity, the larger particle size experiments resulted in a larger fitted hardness values than the smaller particle size experiments. Examples of this behaviour include 625 plate, A53 Gr. B steel, and A240 Type 2205 duplex stainless steel. This may indicate a degree of surface layer hardening due to particle impact, which is expected to be more severe for larger particles. This, together with associated particle fragmentation effects, may contribute to the counter-intuitive result that *small* particles gave *higher* erosion rates than large ones at the same velocity. For example, at v=90 m/s, the erosion rates were on average 80 % higher for the 6.9 μm powder than for the 30.4 μm; similarly, at v=130 m/s, the erosion rates were on average 70 % higher for the 6.9 μm powder than for the 30.4 μm.The counter-intuitive effect of particle size on erosion rate differed from what most erosion models predict, and was thus worth further investigation, in the next chapter.

CHAPTER 6

INVESTIGATION OF PARTICLE SIZE EFFECTS

It was found that the erosion rates using fine (6.9 μm) magnetite powder [1] were, on average 1.8 times higher than those obtained presently with the coarse (30.4 μm) powder. This counter-intuitive result was worthy of further investigation.

6.1 EXPLANATIONS FOR OBSERVED PARTICLE SIZE EFFECTS THAT CAN BE EXCLUDED

The mass flow rates and maximum blasting depths used in both the fine and coarse powder experiments were within the specifications of ASTM G76-07 [8], indicating that inter-particle collisions and surface curvature effects were unlikely to have played a role. The linearity of the vast majority of the plots in volumetric erosion rates indicated that steady state erosion conditions were reached, ruling out incubation effects. Figures 3-4 to 3-7, indicate that the particle velocities were very similar for both the fine (6.9 μm) and coarse (30.4 μm) powders; i.e. independent of powder, the velocities at 100 and 200 kPa were approximately 90 and 130 $m.s^{-1}$. Since the powders were also of similar purity, it can thus be concluded that in all likelihood, both sets of experiments were performed under similar conditions, giving valid erosion rate values.

A number of eroded samples were examined using scanning electron microscopy (SEM). For each sample, three micrographs were obtained: one on the virgin uneroded metal, one in the center of the erosion scar, and one at the periphery of the scar. Figures 6-1 (b) and (c), for Type

316L stainless steel using the 30.4 μm and 6.9 μm powders, respectively, show the typical cutting and ploughing mechanisms associated with ductile erosion. Figure 6-1 (a) shows the virgin uneroded sample as a reference. Noting the difference between scales in Figure 6-1 (b) and (c), it is clear that, as expected, the finer particles produced much smaller (i.e., in the plane of the surface) impact cutting/ploughing craters than the larger particles. Thus, the particle size effect was not likely due to a change in erosion mechanism.

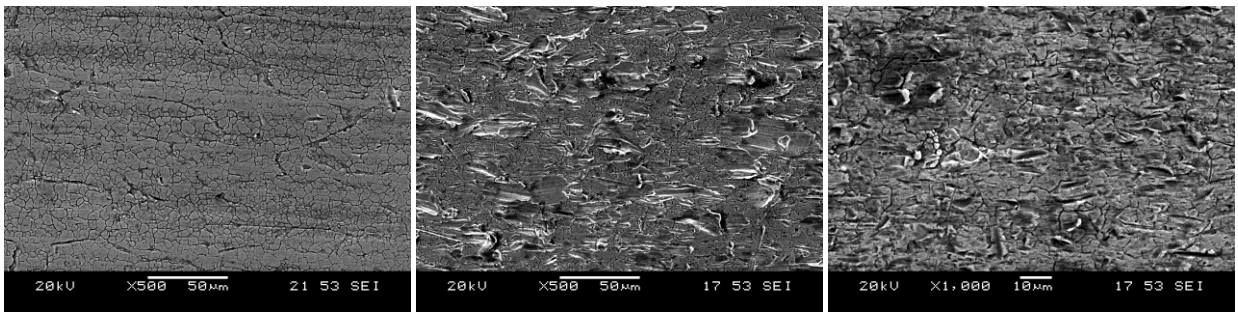

(a) (b) (c)

Figure 6- 1: SEM micrographs of Type 316L Stainless Steel: (a) unblasted virgin material; (b) at periphery of erosion scar after blasting with 30.4 μm powder at 90 m.s^{-1} velocity, α= 15˚, for a dwell time of 300 s; (c) at periphery of erosion scar on eroded with 6.9 μm powder at 90 m.s^{-1}, α= 15˚, for a dwell time of 90 s. Particle trajectory is from left to right

Higher erosion rates associated with smaller particles have also been previously reported by other investigators. For example, erosion in a typical shell-and-tube heat exchanger was investigated numerically using the Lagrangian particle-tracking method, erosion and penetration rates were obtained for sand particles of diameters ranging from 10 to 500 μm [74]. At 130 m.s^{-1} particle velocity, the particle size was found to have a negligible effect on the erosion rate, while at low velocities; the larger particles gave lower erosion rates than the smaller particles [75].

Some investigators have attributed this counter-intuitive behavior to the decreased ability for the larger particles to penetrate deep into the substrate; i.e. larger particle implies a larger

contact area and thus larger resisting force to penetration [76]. Others have attributed the behavior to a decrease in the frequency of particle impacts; i.e. for the same mass flow rate, there are many less particles striking the surface in the large particle case than the small particle case.

6.2 COMPARISON OF EROSION SCAR DIMENSIONS

Figures 6-2 (a) and (b) show the diameters of erosion scars produced by 6.9 μm and 30.4 μm under otherwise identical conditions of 130 $m.s^{-1}$ particle velocity and 90˚ angle of attack, and for the same dwell time. Use of the larger particles resulted in an approximately 0.6 mm larger erosion scar, implying a less focused jet, i.e. a more spread out particle flux on the target material in the case of larger particles. This may be evidence of the fragmentation of the larger particles, as the fragments might be expected to travel in a radial direction upon impact, causing a larger scar. Moreover, the increased particle fragments might have interfered with the incoming particles, thus deflecting them and creating the larger scar. Both the particle fragmentation and the particle interference effect would act to decrease the erosion rate, as they represent 'wasted' energy that could have been used to erode the surface. Finally, the less focused large particle jet may have resulted in an insufficiently high flux at the periphery of the jet for a steady state erosion rate to have been established at the periphery.

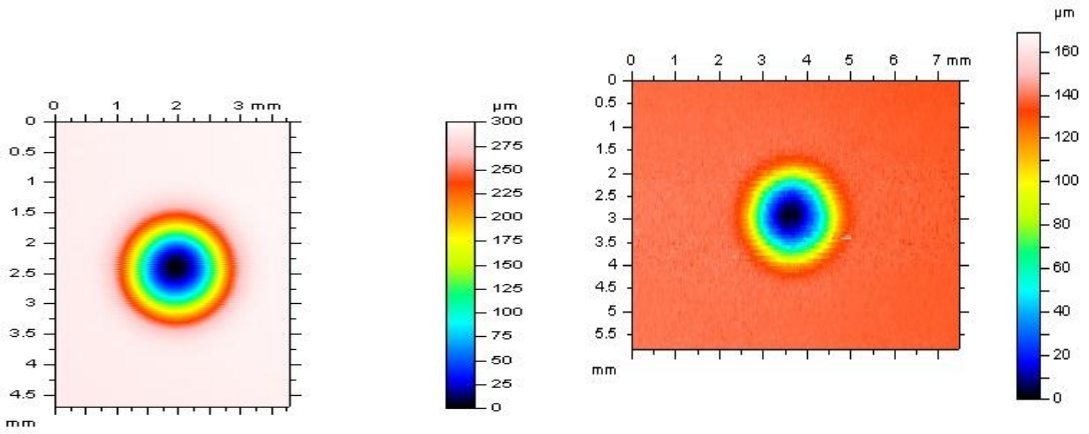

(a) (b)

Figure 6- 2: Profilometer image of erosion scar on Type 316L Stainless Steel eroded at v=130 m.s^{-1},for α= 90˚, and a dwell time of 120 s: (a) 6.9 µm powder; (b) 30.4 µm powder

6.3 DIFFERENCE IN PARTICLE SHAPE

As mentioned in Chapter 2, many investigators have found that particle shape can strongly affect the erosion rate. Figures 6-3 (a) and (b) show the measured aspect ratios, i.e., the longest dimension of a given particle divided by its shortest, for the two powders. The detailed description of how the powder samples were taken and measured can be found in Section 3.2.1. The finer powder has generally higher (average=1.641) and a larger spread in associated aspect ratios than the coarser powder (average=1.557). This is an indication that the particles within the fine powder were more angular than those in the 30.4 µm powder, which might also be expected to contribute to the explanation of why a higher erosion rate resulted from the use of the smaller particles.

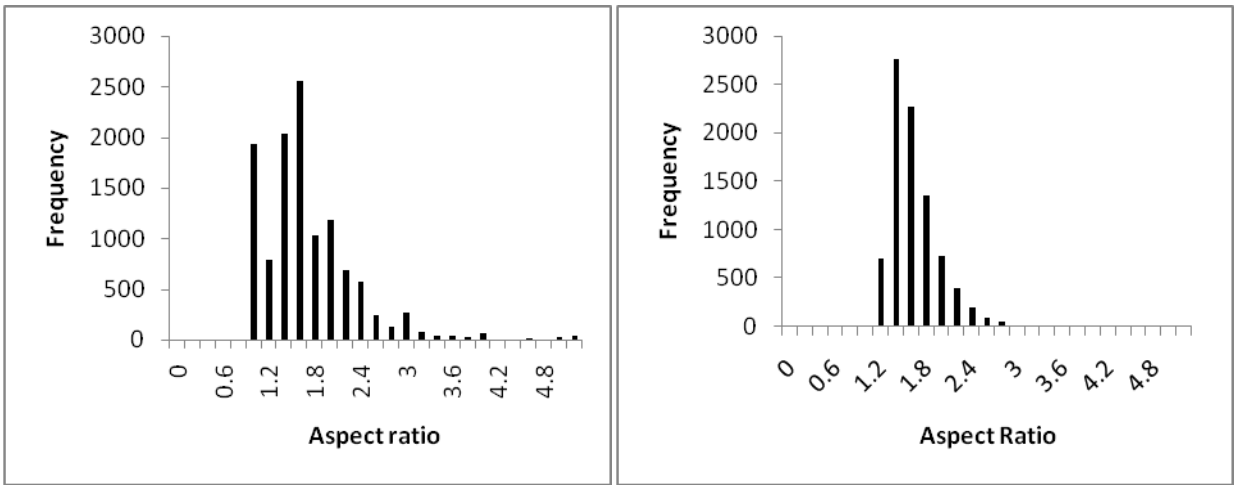

(a) (b)

Figure 6- 3: Measured aspect ratio of (a) 6.9 µm magnetite powder; (b) 30.4 µm magnetite powder

6.4 EFFECTS ASSOCIATED WITH A HARDENED SURFACE LAYER

As discussed in Chapter 2, the hardness of the target material is a dominant factor in the constitution of most erosion models. In general, the lower the bulk hardness, the larger is the expected erosion rate [71]. It is clear that the effect of hardness on erosion resistance must be considered in relation to the erodent properties (*i.e.*, size, shape, and density) and erosion test conditions (*i.e.*, velocity, temperature, and angle of impact). It is reasonable to assume that the hardness measurements of the erosion samples reasonably reflect the flow-stress levels achieved during erosion [77]. In Section 5.4, it was speculated that a hardened surface layer might develop differently when using large and small particles. A series of experiments were undertaken to investigate this hypothesis.

A micro hardness tester (MICROMET® 5100 Series Micro-indentation Hardness Testers, Buehler, Whitby, Ontario) was used to compare the hardness value of the virgin surface of several of the material with the hardness of surface after it had been blasted. Samples of type

410 Stainless Steel blasted at v=130 m/s and at 90˚ angle of impact were utilized. This represented the experimental scenario that was most likely to lead to a hardened surface layer, i.e. where the energy transfer normal to the surface should be a maximum.

The relatively high roughness of the eroded samples required a surface preparation procedure to be performed on the candidate samples, before their hardness could be measured. As a first step, chemical electro-polishing was implemented based on ASTM B912-02 [78]. The standard explains the passivation of stainless steel using an electro polisher (ELECTROMET® 4 Polisher/Etcher, Buehler, Whitby, Ontario) with a combination of 50% Sulfuric acid (96% purity) and 50% Orthophosphoric (85% purity) at 75˚ C for 180 s. This method typically removes surface waviness up to a 7 μm depth, but with most concentration on the peaks. Initially, very high hardness values (e.g. 410, 316L) were read on specimens blasted with the coarser powder. It was found that these unrealistically high values were due to placing the hardness tester on the top of large magnetite particles that were embedded in the samples. An additional surface preparation was necessary to remove these embedded particles, while not removing or disturbing the possibly hardened surface layer material. The use of a chemical solvent, Nitol, was proposed by ASTM A380-06 [79] for removing iron oxides and other impurities from stainless steel. Nitol is a combination of 30% Nitric acid (90% purity) and 70% of Ethanol (35% purity). The specimens were immersing in Nitol for 30-40 minutes at 40˚ C. After these two post-processing steps, the extremely high hardness values disappeared, and the measured hardness values were repeatable.

In order to check the ability of Nitol in solving the iron oxide particles, a sample of iron oxide prepared following ASTM and mixed in the Nitol. This mixture was leave for 40 minutes

in identical test condition of immersing material in the Nitol. Nitol show the ability of the most micron scale iron oxide particles.

In Table 6-1, for each stainless steel candidate material, the as-received surface hardness values are compared with the hardness values (minimum 10 repetitions) after polishing, before and after using the Nitol solution. The standard deviations of the hardness values were relatively low, considering that the indentation loads used varied from (200-1000) gf. Use of the Nitol solution apparently removed the embedded iron oxide particles, resulting in more reasonable hardness values. After immersion in Nitol, the hardness values were found to be significantly higher than the as-received values. Moreover, lower average hardness values were observed for the samples blasted with the fine powder than the larger particle size. These results imply that that a hardened layer was formed, and that this layer was harder in the case of the experiments with the larger particles, possibly due to the higher associated incident particle kinetic energies. This might be a possible reason for lower erosion rate values that were reported for the larger particles.

Table 6-1: Comparison of measured hardness for several materials before and after using Nitol, with the as-received values. The ± values indicate one standard deviation of at least 10 measurements.

Material	As received HV	Experimental Condition			
		d=30.4 µm, V= 130 m.s^{-1}		d=6.9 µm, V= 130 m.s^{-1}	
		(HV)	(Hv) after immersing in Nitol	(HV)	(HV) after immersing in Nitol
410 Stainless Steel	152	308±68.3	215.5±37	179.22±23.1	189.4±39.4
316L Stainless Steel	164	377±71.5	311.2±54	328.7±27.7	229.9±42
Alloy 625	227	488±88.7	360.6±27	321.6±83.4	301.8±62.4
17-4 PH Stainless Steel	352	788±9.3	360.4±70.1	380.1±9.3	330.8±17
2205 Duplex Stainless Steel	262	507±266	297.1±41.23	278.1±37.08	278.1±25.8

The averages reported in Table 6.1 were the result of using a variety of indentation loads between 200-1000 gf. In most cases, the figures show that there was a larger difference between the hardness values before and after immersing in Nitol for the larger particles, than a similar sample blasted with smaller particles. The differences between hardness values of two particle sizes after immersed in Nitol have shown in the Table 6-1 statistically significant with 95% confidence.

Since the hardness was expected to vary through the thickness of the specimens, a more detailed investigation of hardness variation with indentation depth was undertaken in order to determine the approximate thickness of the hardened layer. Vickers micro hardness indentation were performed for four different incremental loads (100, 300, 500, 1000 gf), each resulting in different indentation depths. A minimum of three hardness measurement repetitions were

performed at each load. The variations of hardness with indentation depth at the center of the blasted crater are plotted in Figures 6-4 (a) to (e). Although there is some variation, the hardness values generally show a decreasing trend with depth, for all materials. In most cases, the hardness is maximum in the first 10-30 μm below the surface. This implies a higher particle embedding rate for the larger powder than the smaller powder. Since embedded particles can shield the surface from erosion due to subsequent impacts, and can also result in increased particle fragmentation, this also likely contributed to the lower than expected measured erosion rate seen with the coarse powder, when compared to that measured using the fine powder.

The micro hardness value measured for case of 410 stainless steel after it was immersed into Nitol (Figure 6-4 (a)) shows unrealistic value for hardness gradation. The difficulty on reading the indentation effect for such a shiny surface after immersed in chemical could be the main source of this error.

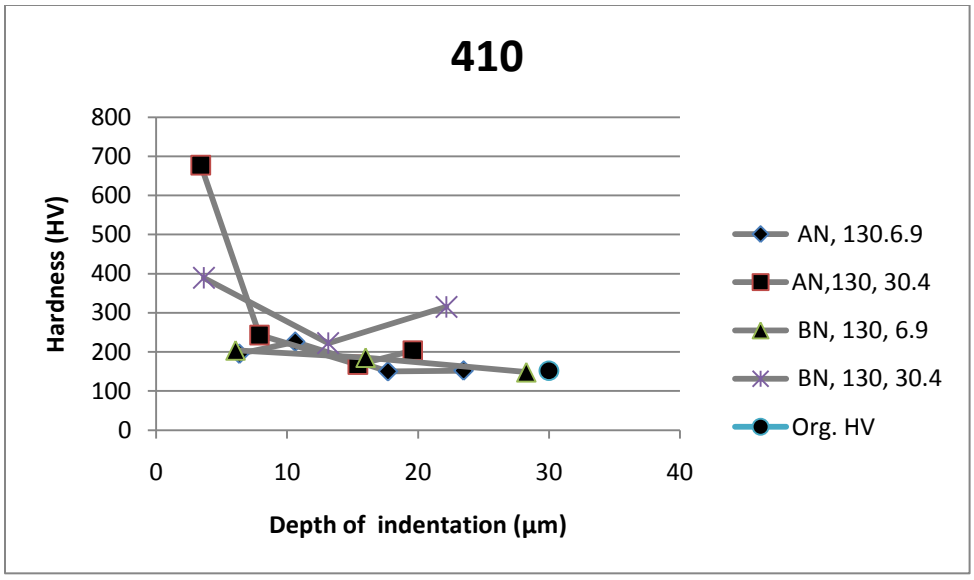
410
Hardness (HV)
800
700
600
500
400
300
200
100
0
0
10
20
30
40
Depth of indentation (µm)
AN, 130.6.9
AN,130, 30.4
BN, 130, 6.9
BN, 130, 30.4
Org. HV

(a)

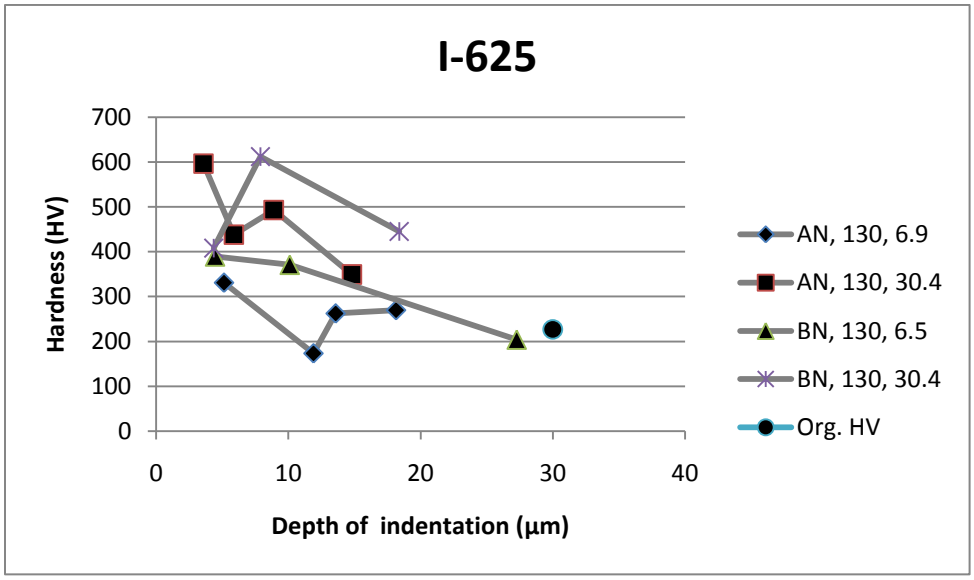
I-625
Hardness (HV)
700
600
500
400
300
200
100
0
0
10
20
30
40
Depth of indentation (µm)
AN, 130, 6.9
AN, 130, 30.4
BN, 130, 6.5
BN, 130, 30.4
Org. HV

(b)

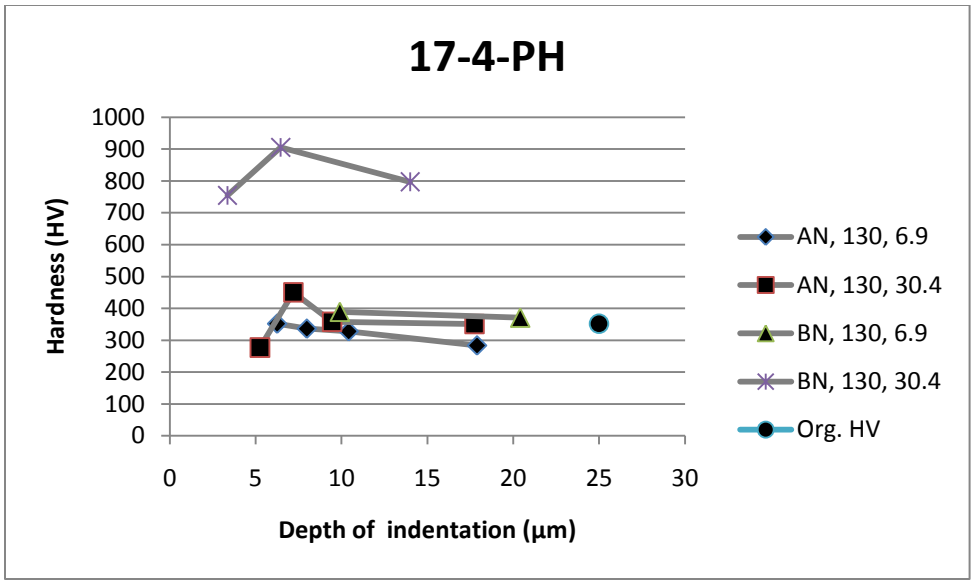
17-4-PH
Hardness (HV)
1000
900
800
700
600
500
400
300
200
100
0
0
5
10
15
20
25
30
Depth of indentation (µm)
AN, 130, 6.9
AN, 130, 30.4
BN, 130, 6.9
BN, 130, 30.4
Org. HV

(c)

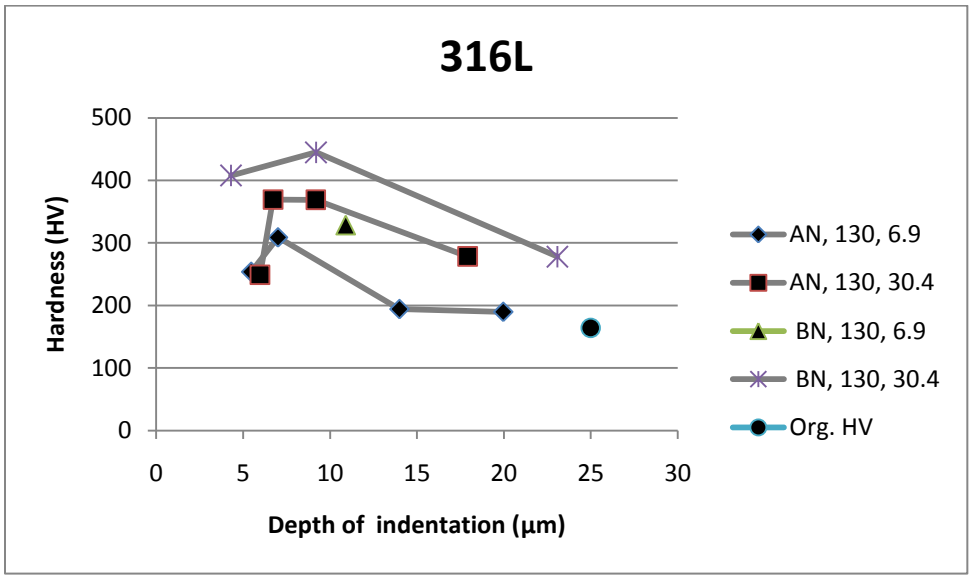
316L
Hardness (HV)
500
400
300
200
100
0
0
5
10
15
20
25
30
Depth of indentation (µm)
AN, 130, 6.9
AN, 130, 30.4
BN, 130, 6.9
BN, 130, 30.4
Org. HV

(d)

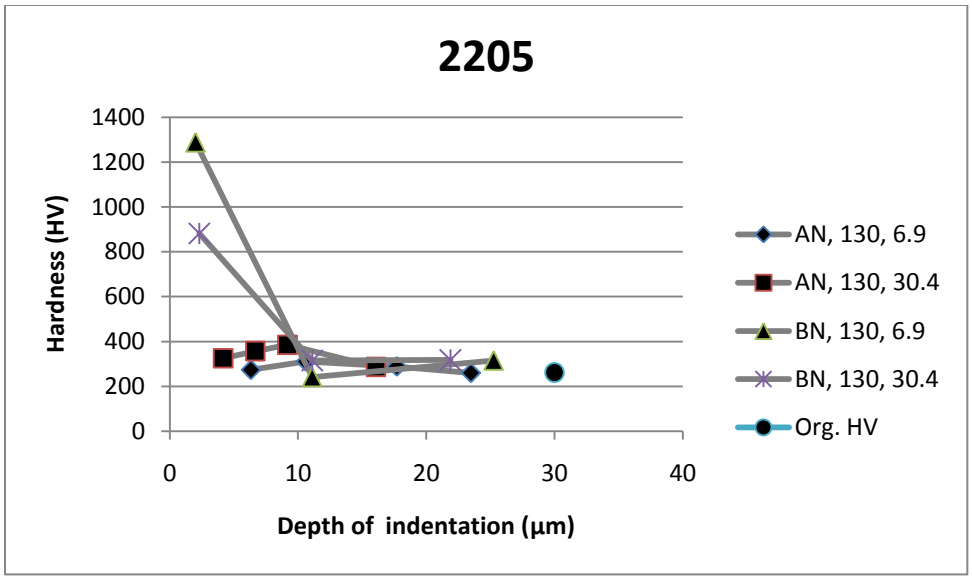

(e)

Figure 6- 4: Hardness value (HV) variation for various depth of indenter penetrations at 130 m/s incident particle velocity, for d= 30.4 µm and d= 6.9 µm particles, on (a) 410-A240 Type 410 stainless steel. (b) 625-Alloy 625 plate , (c) 17-4 PH-17-4 PH stainless steel plate ,(d) 316L-Type 316L stainless steel, .(e) 2205- A240 Type 2205 duplex stainless steel plate. AN = after immersion in Nitol, BN= before immersion in Nitol

6. 5 COMPARISON OF PARTICLE FRAGMENTATION RATE ON BOTH PARTICLE SIZE

The most common cited reason for reduced erosion using larger particles is their tendency to fracture upon impact at high velocity [80]. In the present work, it was hypothesized that larger particles might have had a greater tendency to shatter after impacting the surface because of both the increased particle embedding, and the higher hardened layer. The higher dwell time used for the larger particle (Table 3-3) than small particle (Table 3-2) under similar particle mass flow rates indicates that a larger amount of powder was needed in order to reach steady state erosion. The reason for this longer time to reach steady state might indicate that particle fragmentation occurred.

To investigate whether particle fragmentation occurred in the present experiments, samples of the 30.4 µm powder blasted through the nozzle were collected (Figure 6-5 (a)), and compared to samples which were collected after having struck a 316L Stainless Steel plate at 90˚ incidence at 130 $m.s^{-1}$ (Figure 6-5 (b)). In both experiments particles were blasted into cylinders which had filters fitted to the top where the nozzle was inserted, to ensure that small particles did not escape and that there was no significant back pressure built up. In the first experiment, particles that were blasted into a 20 cm long cylinder were collected and sized (Figure 6-5 (a)). It was assumed that the particles impacting the bottom of this cylinder at such a large distance from the nozzle would have lost most of their energy, and thus were unlikely to fracture. In the second experiment, the particles were collected after being blasted against a target plate at a 10 mm nozzle to plate standoff distance (Figure 6-5 (b)), simulated the erosion rate experiments. In this case, the plate was 45 mm from the top of the cylinder to ensure that the amount of powder collected in the filter at the top of the cylinder was negligible.

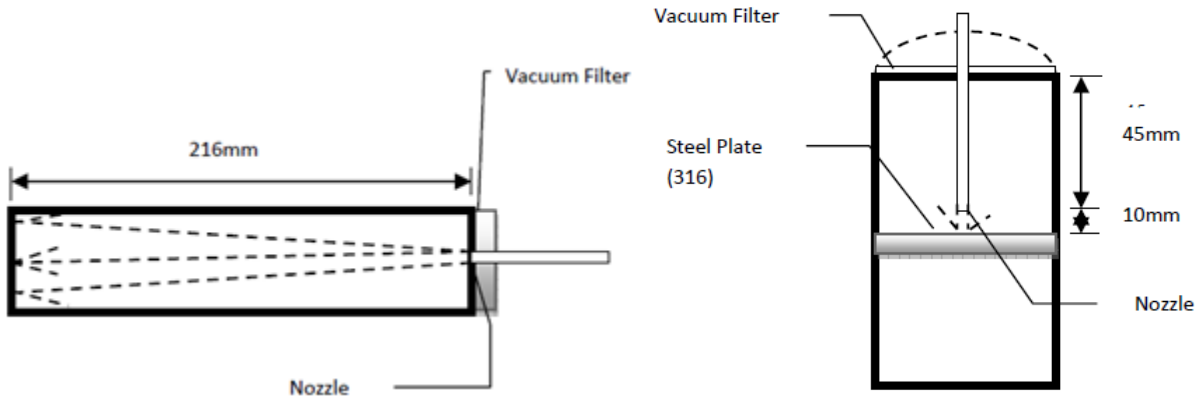

(a) (b)

Figure 6- 5: (a) Apparatus for collecting particles blasted from nozzle; (b) Apparatus for collecting particles that impacted and rebounded from plate

Figure 6-6 shows that the particles collected in experiment (b) were significantly smaller (reduction of 7.9 μm in mean diameter) than those collected in experiment (a), confirming the hypothesis that the large particles did indeed fracture upon impact. Thus, much of the incident kinetic energy that could have been used to damage the target was instead consumed in fracturing the particles. This may explain why the 30.4 μm powder resulted in lower erosion rates than the 6.9 μm powder. This test did not perform for 6.9 μm powder, because in case the particle fragmentation occurred on erosion test, powder with size lower than 4 μm does not affect the erosion mechanism [81]. Also, if the amount of fragmentation happened for the small powder size was significant; measuring the size of fragmentation happened powder value will not be reliable.

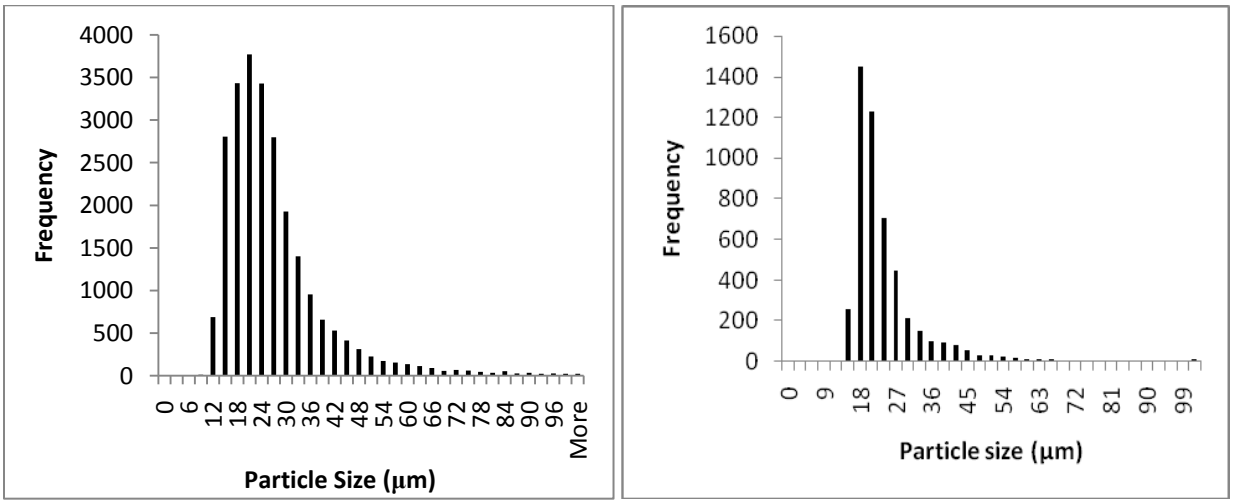

(a) (b)

Figure 6- 6: (a) Particle size distribution of Grade 3105 magnetite powder having a mean spherical diameter of 30.4 μm; (b) Particle size distribution of Grade 3105 magnetite powder was having a mean spherical diameter of 22.5 μm

CHAPTER 7

7.1 SUMMARY AND CONCLUSIONS

Experimental measurements of the erosion rate of 12 candidate materials for use in gas pipelines control valves using magnetite particles of 6.9 μm and 30.4 μm average diameters were made. The blasting tests were performed at two particle velocities, and six angles of impingement (15°, 30°, 45°, 60°, 75°, and 90°). The peak particle velocities at a 10 mm distance from the nozzle exit were measured using Particle Image Velocimetry (PIV) and found to be approximately 90 and 130 $m.s^{-1}$, for blasting pressures of 100 kPa and 200 kPa, respectively.

For each experimental point, the volume removed from the target material was calculated using an optical profilometer, and the measured erosion rate was expressed as the volume removed from the target material per unit mass of the impinging particles. All the erodible materials exhibited ductile erosive behavior, with maximum erosion rates occurring at shallow impingement angles. The majority of the erosion rates for the high velocity case were found to be between 1.8 and 2.5 times those of the low velocity case, indicating that the erosion rate depended on the kinetic energy of the particles.

The most erosion resistant material was found to be the tungsten carbide, which could not be eroded at either velocity at any impingement angle for dwell times up to 400 s. Stellite 12 was the second most erosion resistant material after tungsten carbide at all angles of attack and for both particle velocities.

Most materials exhibited a maximum erosion rate between 15˚ to 30˚, indicating a typically ductile erosive response. The nickel coated 1018 steel appeared to erode in a brittle

manner for 30.4 μm and 130 $m.s^{-1}$ particle size and velocity, respectively. This was probably due to coating delamination upon particle impact.

The erosion rates for 6.9 μm powder were higher than those for 30.4 μm powder. This counterintuitive result was found to be due to the impact of the larger particles producing a harder and thicker surface layer, a greater degree of particle embedding, and a greater degree of particle fragmentation, than the smaller particles.

A model developed by Oka et al. [1] was found to fit the experimentally measured erosion rates well. The resulting curve fits using this model can be used in future attempts to model the evolution of eroded profiles, using, for example, computational fluid dynamics simulations.

7.2 SUGGESTED FUTURE WORK

There are a number of ways in which the current work could be extended:

(i) The present study considered magnetite particle with only two sizes of 6.9 μm and 30.4 μm, but it would be interesting to perform experiments with more powder sizes. This would allow a greater understanding of the counter-intuitive particle size effect.

(ii) More investigation on the particle fragmentation effects on erosion rate, perhaps using different powder sizes, are also required to justify the differences that were observed between two particle sizes. More hardness testing would be desirable as well, in order to verify the causes and extent of the formation of the hardened layer under the blasted area.

(iii) Additional experiments at more particle velocities would provide a better measure of the velocity exponent, for use in erosion modeling.

(iv) The erosion curve fits could be used in conjunction with CFD models to study, in detail, the development of eroded profiles in control valves. This might allow a proper specification of the best materials to be used in different portions of the valve.

(v) More investigation on the A 1018 Nickel plated could clarify the erosion mechanism transition occur from ductile to brittle for larger particle size and higher velocity. In addition, the interaction between erosion and corrosion mechanism on this particular material need to be investigated.

APPENDIX A

MATERIAL TESTING REPORTS (MTR) AND MATERIAL DATA SHEETS

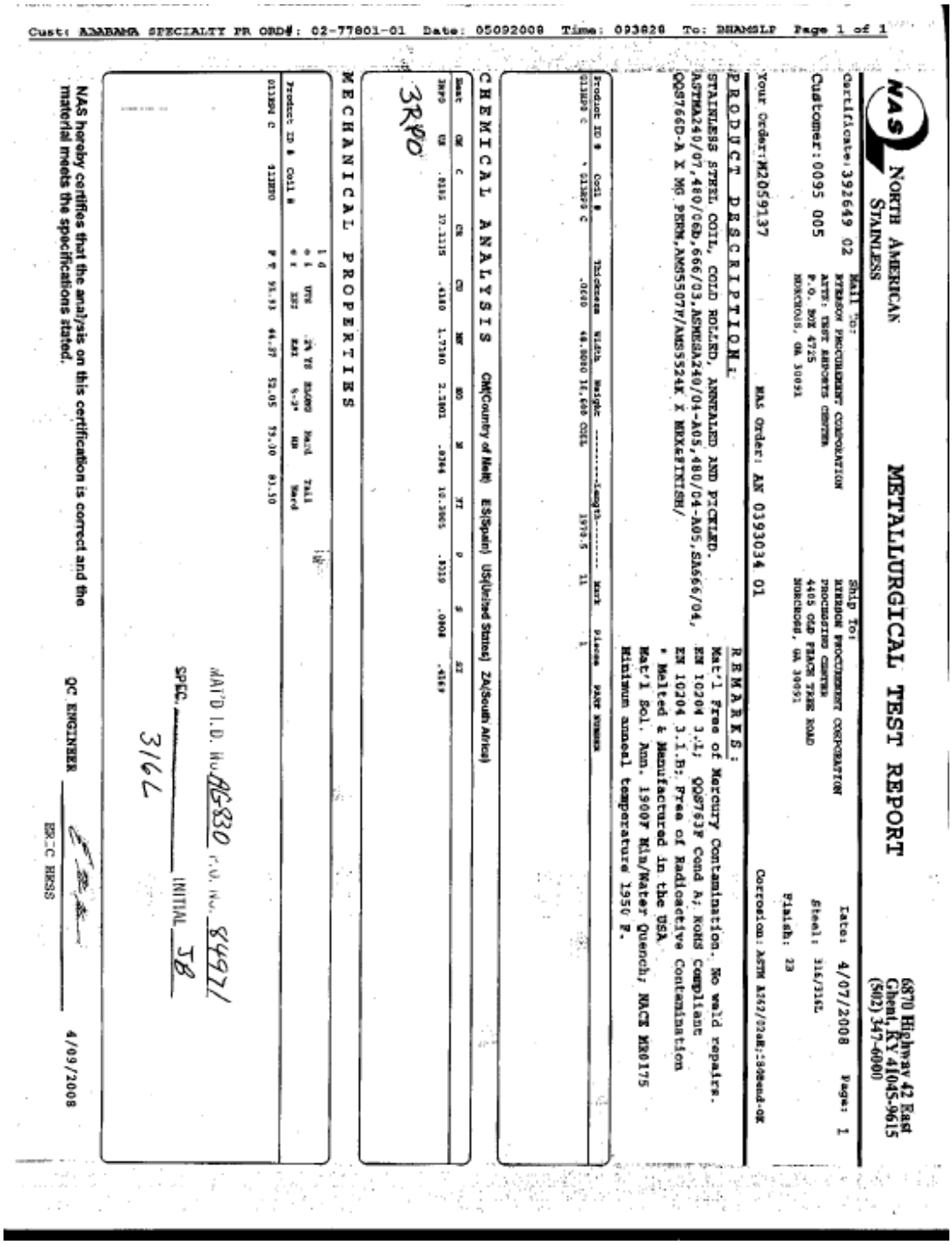

Cust: ALABAMA SPECIALTY PR ORD#: 02-77801-01 Date: 05092008 Time: 093828 To: BHAMSLP Page 1 of 1

NAS NORTH AMERICAN STAINLESS

METALLURGICAL TEST REPORT

6870 Highway 42 East
Ghent, KY 41045-9615
(502) 347-4000

Certificate: 392649 02 Mail To: BIRMINGHAM PROCUREMENT CORPORATION
ATTN: TEST REPORTS CENTER
P.O. BOX 4725
MONCROVE, GA 30052

Ship To: BIRMINGHAM PROCUREMENT CORPORATION
PROCESSING CENTER
4405 OLD PEACH TREE ROAD
MONCROVE, GA 30052

Date: 4/07/2008 Page: 1

Customer: 0095 005

Steel: 316/316L

Finish: 2B

Your Order: M2059137 NAS Order: AN 0393034 01 Corrosion: ASTM A262/Prac E-Method-CM

PRODUCT DESCRIPTION:

STAINLESS STEEL COIL, COLD ROLLED, ANNEALED AND PICKLED.
ASTMA240/07,480/06b,666/03,ASMESA240/04-A05,480/04-A05,SA666/04,
QQS766D-A X MG PERM,AMS5507F/AMS5524K X MRK&FINISH/

REMARKS:

Mat'l Free of Mercury Contamination. No weld repairs.
EN 10204 3.1; QQS763F Cond A; RoHS Compliant
EN 10204 3.1.B; Free of Radioactive Contamination
• Melted & Manufactured in the USA
Mat'l Sol. Ann. 1900F Min/Water Quench; MACE MR0175
Minimum anneal temperature 1950 F.

Product ID #	Coil #	Thickness	Width	Weight	Length	Mark	Pieces	PART NUMBER
013809 C	* 513809 C	.0060	48.0000	16,600 COIL	1973.5	11	1	

CHEMICAL ANALYSIS CM(Country of Melt) ES(Spain) US(United States) ZA(South Africa)

Heat	CM	C	CR	CU	MF	MO	N	NI	P	S	SI
3RP0	US	.0315	17.1115	.4310	1.7310	2.2803	.0364	10.2865	.0319	.0004	.4569

3RP0

MECHANICAL PROPERTIES

Product ID #	Coil #	I d e i TYS	UTS	% EL EAS	BEND	Hard	Tail Hard
013809 C	513809	P T 59.83	84.87	52.05	T5.30	80.30	

NAS hereby certifies that the analysis on this certification is correct and the material meets the specifications stated.

MAT'D I.D. W/ AB330 P.O. NO. 84971

SPEC. _____ INITIAL JB

3/16

QC ENGINEER _____ 4/09/2008

ERIC HESS

Figure A 1: A240 Type 316 stainless steel

NOTICE OF SHIPMENT/
PACKING LIST

ATI Allegheny Ludlum
Allegheny Technologies

M.A TRACER # 158629 CERTIFICATE OF TEST

AL 6168-3 407

CUST. ORDER NO. & DATE: C24005 | 09/18/07

FORMS DISTRIBUTION: SHIP TO → | SPEC 1

SOLD TO → ROLLED ALLOYS INC.
P.O. BOX 310
TEMPERANCE MI 48182

CUST. CODE: 773550

ACCEPTING MILL: VANDERGRIFT, PA.

REPEAT ORDER: 86040-3

DO DATE: 31

PRI. PRIORITY: SEC-

SHIPPER NO.: 560808

GOVT. CONTRACT: DSO DSO 584

PRODUCT CODE: 13020103060000

MATL: 1560

SHIPPING LOCATION: VANDERGRIFT

MILL ORDER NUMBER: 34-097-043

INVOICE: 653104

DATE SHIPPED: 11/09/07

SHIP TO: ROLLED ALLOYS INC.
9944 PRINCETON GLENDALE ROAD
CINCINNATI OH 45246

P4

MATL FOR P.O. NO. 82632 / P.O. NO. 82612

SPEC: 2205 INITIAL JB

GRADE AND SPECIFICATIONS
AL 2205 DUPLEX STAINLESS STEEL SHEET C R COILS ANNEALED 2D FIN 3 EDGE (UNS S31803) (UNS S32205)
(ASTM-A-240-07 S31803) (ASTM-A-240-07 S32205) (ASME-SA-240-A05 - S31803) (ASME-SA-240-A05 - S32205)

CARRIER - GROSS,RONALD,INC.

ITEM	PCS	DIMENSIONS W/G/L	HEAT #	COIL #	TEST #	GROSS	TARE	NET	THEO	TAG #/ CD	SKID
001B	1	48.02/.0595/590.	825709	092117N690B	G208033	5870	50	5820	534494		
	1	48.02/.0595/619.	825709	092117N690C	G208033	6200	50	6150	534493		
	1	48.02/.0595/621.	825709	092117N690D	G208033	6595	50	6545	534498		
C CUST IDENTITY 2390213900031											
	3	SKIDS				18665	150	18515			

GAUGE TOL: + 0.00300 - 0.00300

DIST: DO NOT SEND ACKMT TO CUSTOMER - WILL BE SENT ELECTRONICALLY AT TIME OF SHPMT, FAX CPY OF S/
TO DEBORAH NEANOVER @ 513-874-0043

HEAT		--C---	--MN--	--P---	--S---	--SI--	--CR--	--NI--	--MO--	--N---
825709		.025	1.80	.027	.001	.38	22.5	5.40	3.16	.18

ITEM	TEST NO	YIELD PSI *	TENSILE PSI	% ELONG IN 2"	% R/A	HARDNESS	BEND	GRAIN SIZE	HARDENABILITY
001B	G208033	T 90500.	122000	26.	NR	24.0HRC	NR	NR	NR
		T 93500.	125000	26.		24.0HRC			

* Y.S. BY 0.2% OFFSET METHOD
ASTM-A-923

ITEM	TEST NO	FRACT. C	CARBIDES
001B	G208033	PASS	NONE

M.A TRACER # 158529

ROLLED ALLOYS QUALITY ASSURANCE
APPROVED
DATE 11/13/07

11/09/07 11:36:36

PAGE 01 - CONTINUED ON PAGE 02 REPRINT

CONSIGNEE--Please Note--This consignment was turned over to carrier in first class condition, being correctly loaded, at which time our responsibility for loss or damage in shipment ceased. For prior damage to be recovered, have a full description made by transportation agent on waybill before signing.

WARNING: Material Safety Data Sheets for this product have been supplied to your Purchasing Department. For an additional copy phone 724-224-0057. CAUTION: Processing that involves torch cleaning, welding, grinding or machining may release fumes, dust, or oxidizes may cause lung disease. See Material Safety Data Sheets for further information.

AVERTISSEMENT: Fiches d'information--sécurité de ce produit ont été fournies à votre département chargé des achats. Pour obtenir des exemplaires supplémentaires veuillez téléphoner au numéro suivant 724-224-0057 Attention: les traitements comportant la production de vapeurs, poussières, ou oxydises peuvent causer des maladies pulmonaires. Pour plus de renseignements se référer aux fiches d'information-sécurité.

The above is a true copy of data on file. The material and test results conform to the sales contract and specification(s) as set forth in Allegheny Ludlum's Order Acknowledgment.

Dee M. Xenakis
Director, Corporate Quality Assurance

AL 6168-3 407

Figure A 1: A240 Type 2205 duplex stainless steel

NOTICE OF SHIPMENT/
PACKING LIST

ATI Allegheny Ludlum

CERTIFICATE OF TEST

AL 6188-3 407

CUST. ORDER NO. & DATE: C24005

ACCEPTING MILL: VANDERGRIFT,PA.

SHIPPER NO.: 560808

PRODUCT CODE: 13028183064000

MILL ORDER NUMBER: 34-897-043

DATE SHIPPED: 11/09/07

SOLD TO: ROLLED ALLOYS INC.
P.O. BOX 310
TEMPERANCE MI 48182

CUST. CODE: 773550

SHIP TO: ROLLED ALLOYS INC.
9944 PRINCETON GLENDALE ROAD
CINCINNATI OH 45246

SHIPPING LOCATION: 1548 VANDERGRIFT PA

INVOICE: 658104

WA TRACER# 158529

GRADE AND SPECIFICATIONS
AL 2205 DUPLEX STAINLESS STEEL SHEET C R COILS ANNEALED 2D FIN 3 EDGE (UNS S31803) (UNS S32205)
(ASTM-A-240-07 S31803) (ASTM-A-240-07 S32205) (ASME-SA-240-A05 - S31803) (ASME-SA-240-A05 - S32205)

CARRIER - GROSS,RONALD,INC.

NR = DATA NOT REQUIRED
GRADE VERIFICATION WAS CARRIED OUT SPECTROSCOPICALLY

ALLEGHENY LUDLUM DOES NOT USE MERCURY IN THE TESTING OR PRODUCTION OF ITS PRODUCTS. TO THE BEST OF ALLEGHENY LUDLUMS KNOWLEDGE, UNDERSTANDING, AND BELIEF, THIS MATERIAL WAS NOT CONTAMINATED BY MERCURY WHILE IT WAS BEING PRODUCED IN OUR FACILITIES.

THIS CERTIFICATE OF TEST SHALL NOT BE REPRODUCED EXCEPT IN FULL WITHOUT THE WRITTEN APPROVAL OF THE COMPANY. THE RECORDING OF FALSE, FICTITIOUS OR FRAUDULENT STATEMENTS OR ENTRIES ON THE CERTIFICATE MAY BE PUNISHED AS A FELONY UNDER FEDERAL LAW. MATERIAL WAS MANUFACTURED IN ACCORDANCE WITH THE ALC QUALITY MANUAL REVISION 16 DATED 08/07/2006. ALC HOLDS SEVERAL QUALITY CERTIFICATIONS THAT INCLUDE ISO-9001. DIN EN 18204:2005 - 3.1. ALLEGHENY LUDLUM IS APPROVED AS A MANUFACTURER ACCORDING TO AD-MERK BLATT WO/TRD100 AND THE PRESSURE EQUIPMENT DIRECTIVE PED 97/23/EC. TESTING WAS PERFORMED AT ALC NADCAP AND ISO/IEC 17025 APPROVED LABORATORIES LOCATED AT NATRONA HEIGHTS, BRACKENRIDGE, LATROBE, MIDLAND, PA FACILITIES OR A NADCAP AND ISO/IEC 17025 ACCREDITED LABORATORY.

ALLEGHENY LUDLUM PERFORMS CHEMICAL ANALYSIS BY THE FOLLOWING TECHNIQUES:
C,S BY COMBUSTION/INFRARED
N,O,H BY INERT FUSION/THERMAL CONDUCTIVITY
MN,P,SI,CR,NI,MO,CU,CB,CO,V BY WDXRF
B BY DES
AL AND TI (>=0.10%) BY WDXRF, OTHERWISE BY DES
PB,BI,AG BY GFAA

PAGE 02 -- CONTINUED ON PAGE 03 REFRINT

11/09/07 11:36:36

The above is a true copy of data on file. The material and test results contained herein have been accepted in accordance with the requirements of the Allegheny Ludlum Corporation Quality Assurance Program.

Paul M. Yanulis

Figure A 2 (continued): A240 Type 2205 duplex stainless steel

NOTICE OF SHIPMENT/
PACKING LIST

ATI Allegheny Ludlum

CERTIFICATE OF TEST

AL 6188-3 407

CUST. ORDER NO. & DATE: C240005

DUST. CODE: 773558

ACCEPTING MILL: VANDERGRIFT,PA.

SHIPPER NO.: 5488888

PRODUCT CODE: 1382010306888PP

MILL ORDER NUMBER: 34-897-043

DATE SHIPPED: 11/89/87

FORMS DISTRIBUTION

SOLD TO: SOLD TO
ROLLED ALLOYS INC.
P.O. BOX 318
TEMPERANCE MI 48182

REPEAT: 86040

ORD. QUAN.: 31

PRIME SEC.: PRIME DSD 584

GOVT. CONTRACT:

MATL.: 1360

SHIPPING LOCATION: VANDERGRIFT PA

INVOICE: 658184

SHIP TO
ROLLED ALLOYS INC.
9944 PRINCETON GLENDALE ROAD
CINCINNATI OH 45246

GRADE AND SPECIFICATIONS CARRIER - GROSS,RONALD,INC.
AL 2205 DUPLEX STAINLESS STEEL SHEET C R COILS ANNEALED 2D FIN 3 EDGE (UNS S31803) (UNS S32205)
(ASTM-A-240-07 S31803) (ASME-SA-240-07 S32205) (ASME-SA-240-A05 - S31803) (ASME-SA-240-A05 - S32205)

MATERIAL MELTED AND ROLLED IN THE UNITED STATES AND COMPLIES WITH DFARS EDITION 1998, SECTION
252.225-7014

DA TRACER # 158529

<<<<<<<< FOR ACCESS TO ONLINE CERTIFICATES OF TEST >>>>>>>>
<<<<<<<< REGISTER AT WWW.ALCEXTRA.COM >>>>>>>>

ROLLED ALLOYS

Certification of Conformance: We certify that the above material meets all requirements of the purchase order and material specifications.

Customer : ALABAMA SPECIALTY PROTE
P.O.# 86512 BL
168R SHEET C&R 2205
Tracer No. [158529]

Ship-C58469
48 X 60"
Heat No. [B25709]

Date 12/11/2007
1 PC

9944 Princeton-Glendale Rd.Cincinnati, OH 45246

BEFORE

PAGE 83 - FINAL PAGE

11/89/87 11:36:36

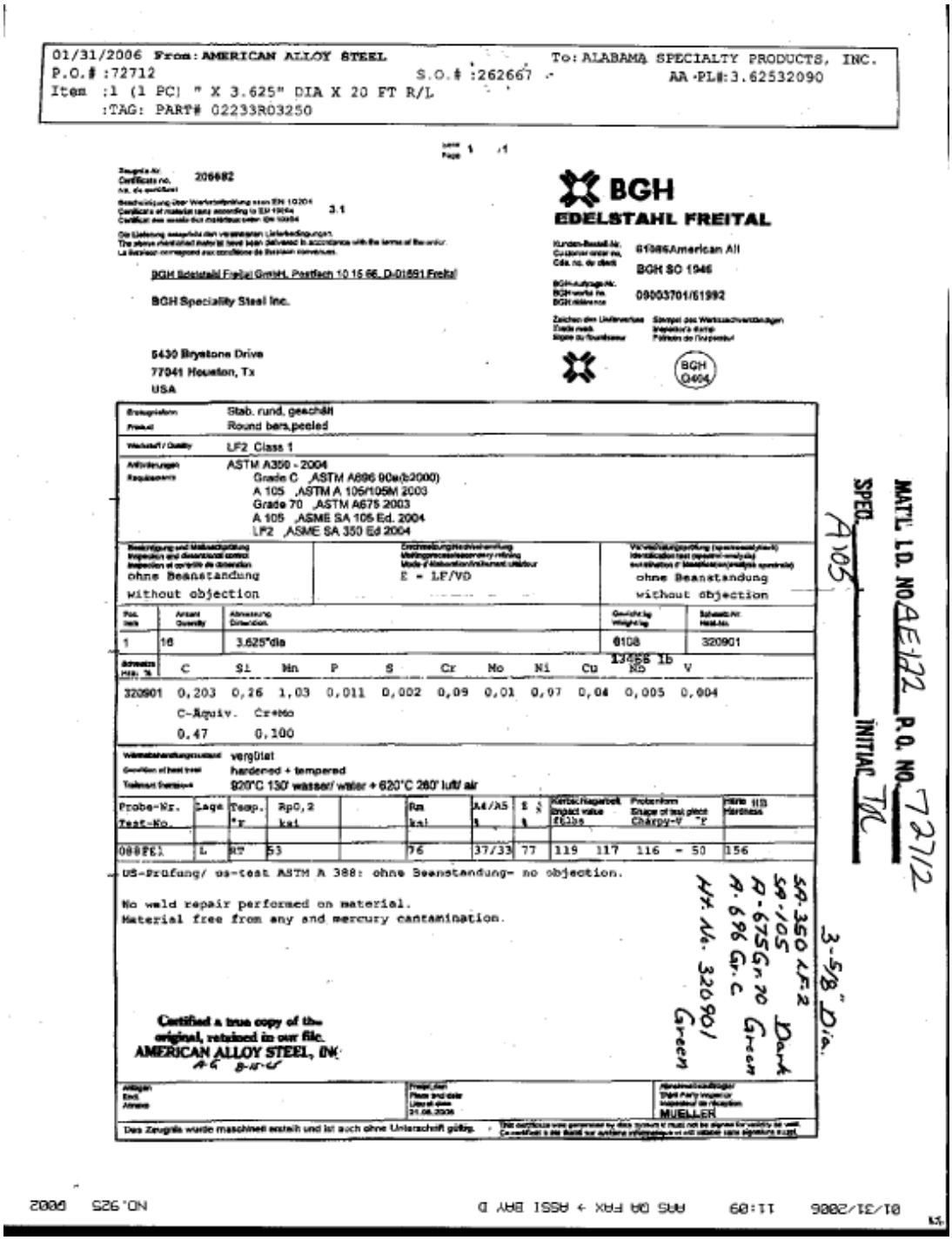

01/31/2006 From: AMERICAN ALLOY STEEL To: ALABAMA SPECIALTY PRODUCTS, INC.
P.O.# :72712 S.O.# :262667 AA-PL#:3.62532090
Item :1 (1 PC) " X 3.625" DIA X 20 FT R/L
:TAG: PART# 02233R03250

Zeugnis-Nr. Certificate no. 206682
3.1
BGH Edelstahl Freital GmbH, Postfach 10 15 66, D-01661 Freital
BGH Speciality Steel Inc.
5430 Bryestone Drive
77041 Houston, Tx
USA

BGH EDELSTAHL FREITAL
Kunden-Bestell-Nr. 61986/American All
BGH SO 1946
09003701/61992
BGH Q404

Stab. rund, geschält / Round bars,peeled
LF2 Class 1
ASTM A350 - 2004
Grade C ,ASTM A696 90a(b2000)
A 105 ,ASTM A 105/105M 2003
Grade 70 ,ASTM A675 2003
A 105 ,ASME SA 105 Ed. 2004
LF2 ,ASME SA 350 Ed 2004

ohne Beanstandung / without objection
E = LF/VD
ohne Beanstandung / without objection

Pos. Item	Anzahl Quantity	Abmessung Dimension	Gewicht kg Weight kg	Schmelz-Nr. Heat-No.
1	16	3.625"dia	6108 13455 lb	320901

Schmelz-Nr. Heat-No.	C	Si	Mn	P	S	Cr	Mo	Ni	Cu	Nb	V
320901	0,203	0,26	1,03	0,011	0,002	0,09	0,01	0,07	0,04	0,005	0,004
	C-Äquiv.		Cr+Mo								
	0,47		0,100								

vergütet / hardened + tempered
920°C 130' wasser/ water + 620°C 260' luft/ air

Probe-Nr. Test-No.	Lage	Temp. °F	RpO,2 ksi		Rm ksi	A4/A5 %	Z %	Kerbschlagarbeit Impact value ft/lbs			Probenform Shape of test piece Charpy-V °F	Härte HB Hardness
088FE1	L	RT	53		76	37/33	77	119	117	116	- 50	156

US-Prüfung/ us-test ASTM A 388: ohne Beanstandung- no objection.

No weld repair performed on material.
Material free from any and mercury contamination.

Certified a true copy of the original, retained in our file.
AMERICAN ALLOY STEEL, INC.
AC 8-11-06

Prüfer/in Place and date 31.08.2006
MUELLER

Das Zeugnis wurde maschinell erstellt und ist auch ohne Unterschrift gültig. / This certificate was generated by data system it must not be signed for validity be valid.

MATL LD. NO AE-122 P.O. NO. 72712
SPEC A105 INITIAL TJC
3-5/8" Dia.
SA-350 LF2 Dark Green
SA-105 Dark Green
A-675 Gr 70 Green
A-696 Gr. C
Mfr No. 320901

01/31/2006 11:09 ARS 08 FAX → ASSI BRY D NO.925 D002

Figure A 3: A105 carbon steel forging

NOTICE OF SHIPMENT/
PACKING LIST

CERTIFICATE OF TEST

RA TRACER # 141168

ROLLED ALLOYS

Certification of Conformance: We certify that the above material meets all requirements of the purchase order and material specifications.

ATI Allegheny Ludlum

C22916 | 08/30/06 | 3773550 | LOUISVILLE, OH | 521441 | 1302010306000 | 34-086-101 | 11/21/06
1612 LOUISVILLE | OH | 245008

9944 Princeton-Glendale Rd(Cincinnati, OH 45246

Customer : ALABAMA SPECIALTY PRDTS
P.O.# 79016 (2/2) GL
16 GA (.056/.063) SHEET 410
Tracer No. [141168]

Ship-to#521441
48 X 72"
Heat No. [973310]

Date 09/10/2006
1 PC

D 246

ROLLED ALLOYS QUALITY ASSURANCE
APPROVED
DATE 9/23/06

GRADE AND SPECIFICATIONS
ALLEGHENY STAINLESS STEEL, TYPE 410 SHEET C R COILS ANNEALED 2D FIN 3 EDGE (AMS 5504M) (UNS S41000)
(ASMR-SA-240-A05) (ASTM-A-240-05A)

CARRIER - BESL TRANSFER COMPANY

ITEM	PCS	DIMENSIONS W/G/L	HEAT #	LIFT #	TEST #	GROSS	TARE	NET	THRU	TAG #/ CD	SKID #
001A	1	48./.0595/685.	973310	09456C124A	L216829	6930	40	6890		448626	
	1	48./.0595/688.	973310	09456C124B	L216829	6980	40	6940		448628	
	1	48./.0595/653.	973310	09456C124C	L216829	6660	40	6620		448632	
PAPER WT. 62# THRU WT. 20389											
C CUST IDENTITY 289021648001											
	3	SKIDS				20570	120	20450			

GAUGE TOL: + 0.00350 - 0.00350

DIST: AT TIME OF SHPMT, FAX CPY S/N TO DEBORAH NEANOVER @513-874-0043 MAIL COPY OF S/N TO SHIP-TO
ATTN: DEBORAH NEANOVER

TYPE HEAT/TEST	--C---	--MN--	--P---	--S---	--SI--	--CR--	--NI--	--AL--	--MO--	--CU--	--N---	--SN--
HEAT 973310	.14	.38	.039	.001	.46	12.35	.37	.001	.04	.12	.01	.01

ITEM TEST NO	YIELD PSI *	TENSILE % ELONG PSI IN 2"	% R/A	HARDNESS	BEND	P&N-S25	GRAIN	MAG PERM
001A L216829			NR	85.HRB	T PASS	TRANS BEND	SIZE	
	T 48300.	79000. 30.		82.HRB	2.		10.	NR
	* Y.S. BY 0.2% OFFSET METHOD							

ITEM TEST NO	HARDEN-ABILITY	NRIT SOURCE
001A L216829	41.0HRC	1.

PAGE 01 - CONTINUED ON PAGE 02

RA TRACER # 141168
11/21/06 09:23:37

MAT'D I. D. NO. AF610 P.O. NO. 79016

SPEC. 410 INITIAL JB

Figure A 4: A240 Type 410 stainless steel

NOTICE OF SHIPMENT/
PACKING LIST

ATI Allegheny Ludlum

CERTIFICATE OF TEST

AL 6188A-7 4/00

CUST. ORD. NO. & DATE
C22916

08/30/06

CUST. CODE
3773550

LOUISVILLE, OH

SHIPPER NO.
521441

PRODUCT CODE
13020103060000

MILL ORDER NUMBER
34-086-101

DATE SHIPPED
11/21/06

SOLD TO
ROLLED ALLOYS INC.
P.O. BOX 310
TEMPERANCE MI 48182

PRIME 85722-0 31
DSO 584
SEC. DSO

SHIP TO
ROLLED ALLOYS INC.
9944 PRINCETON GLENDALE ROAD
CINCINNATI OH 45246

1612 LOUISVILLE OH 245008

GRADE AND SPECIFICATIONS
ALLEGHENY STAINLESS STEEL TYPE 410 SHEET C R COILS ANNEALED 2D FIN 3 EDGE (AMS 5504M) (UNS S41000)
(ASMR-SA-240-A05) (ASTM-A-240-05A)

CARRIER - BNSL TRANSFER COMPANY

NR - DATA NOT REQUIRED
METALLOGRAPHIC MAGNIFICATION: 100X ETCHANT USED: HCl/PICRIC ACID

GRADE VERIFICATION WAS CARRIED OUT SPECTROSCOPICALLY

EQUIPMENT, MATERIALS AND SERVICES ARE OF U.S. ORIGIN

THE NUMERIC CODES SHOWN UNDER MELT SOURCE CAN BE INTERPRETED AS FOLLOWS:
1. - MATERIAL MELTED AND ROLLED IN THE UNITED STATES AND COMPLIES WITH DFARS EDITION 1998, SECTION 252.225-7014
2. - FOREIGN MELT AND ROLLED IN THE UNITED STATES

THIS CERTIFICATE OF TEST SHALL NOT BE REPRODUCED EXCEPT IN FULL WITHOUT THE WRITTEN APPROVAL OF THE COMPANY. THE RECORDING OF FALSE, FICTITIOUS OR FRAUDULENT STATEMENTS OR ENTRIES ON THIS CERTIFICATE MAY BE PUNISHED AS A FELONY UNDER FEDERAL LAW. MATERIAL WAS MANUFACTURED IN ACCORDANCE WITH THE ALC QUALITY MANUAL REVISION 16 DATED 08/07/2006. ALC HOLDS SEVERAL QUALITY CERTIFICATIONS THAT INCLUDE ISO-9001, DIN EN 10204:2005 - 3.1. ALLEGHENY LUDLUM IS APPROVED AS A MANUFACTURER ACCORDING TO AD-MERK BLATT W0/TRD100 AND THE PRESSURE EQUIPMENT DIRECTIVE PED 97/23/EC. TESTING WAS PERFORMED AT ALC NADCAP AND ISO/IEC 17025 APPROVED LABORATORIES LOCATED AT WATSONA HEIGHTS, BRACKENRIDGE, LATROBE, MIDLAND AND LEECHBURG PA FACILITIES OR A NADCAP AND ISO/IEC 17025 ACCREDITED LABORATORY.

RA TRACER # 141168

11/21/06 09:23:37

PAGE 02 - CONTINUED ON PAGE 03

Figure A 4 (continued): A240 Type 410 stainless steel

NOTICE OF SHIPMENT/
PACKING LIST

ATI Allegheny Ludlum

CERTIFICATE OF TEST

CUST. ORDER NO. & DATE: C22916

08/30/06 | 3773550 | LOUISVILLE, OH | 521441 | 1302010106000 | 34-086-101 | 11/21/06

95722-0 | 31 | 1612 | LOUISVILLE | OH | 245008

PRIME SEC. DSO 584

SOLD TO
ROLLED ALLOYS INC.
P.O. BOX 310
TEMPERANCE MI 48182

SHIP TO
ROLLED ALLOYS INC.
9944 PRINCETON GLENDALE ROAD
CINCINNATI OH 45246

GRADE AND SPECIFICATIONS
ALLEGHENY STAINLESS STEEL TYPE 410 SHEET C R COILS ANNEALED 2D FIN 3 EDGE (AMS 5504M) (UNS S41000)
(ASME-SA-240-A05) (ASTM-A-240-05A)

CARRIER - BESL TRANSFER COMPANY

ALLEGHENY LUDLUM PERFORMS CHEMICAL ANALYSIS BY THE FOLLOWING TECHNIQUES:
C,S BY COMBUSTION/INFRARED
N,O,H BY INERT FUSION/THERMAL CONDUCTIVITY
MN,P,SI,CR,NI,MO,CU,CB,CO,V BY WDXRF
B BY OES
AL AND TI (>=0.10%) BY WDXRF, OTHERWISE BY OES
FE,BI,AG BY GFAA

ALLEGHENY LUDLUM DOES NOT USE MERCURY IN THE TESTING OR PRODUCTION OF ITS PRODUCTS.

REISSUED BY ALLEGHENY LUDLUM - 2/21/07 14:36

ALLEGHENY LUDLUM/ALLEGHENY ROONEY WORKS TO THE ROLLS ROYCE RR9000:SABRE REQUIREMENTS.

MATERIAL TESTED AT GEARS (S-400 DATED 4/28/04) AND (S-1000 DATED 1/03/05) APPROVED LABORATORIES AT
ALLEGHENY LUDLUM FACILITIES LOCATED AT TECHNICAL CENTER NATRONA HEIGHTS, BRACKENRIDGE, AND LEECHBURG, PA.

THE MATERIAL WAS HEAT TREATED AT APPROPRIATE TEMPERATURES TO MEET THE DESIGNATED PROPERTIES OF THE
REFERENCED SPECIFICATION.

REISSUED BY ALLEGHENY LUDLUM - 11/29/06 11:08
TERESA A. STUMPF / QUALITY ASSURANCE DEPT.

PAGE 03 - FINAL PAGE.

RA TRACER # 141168

Figure A 4 (continued): A240 Type 410 stainless steel

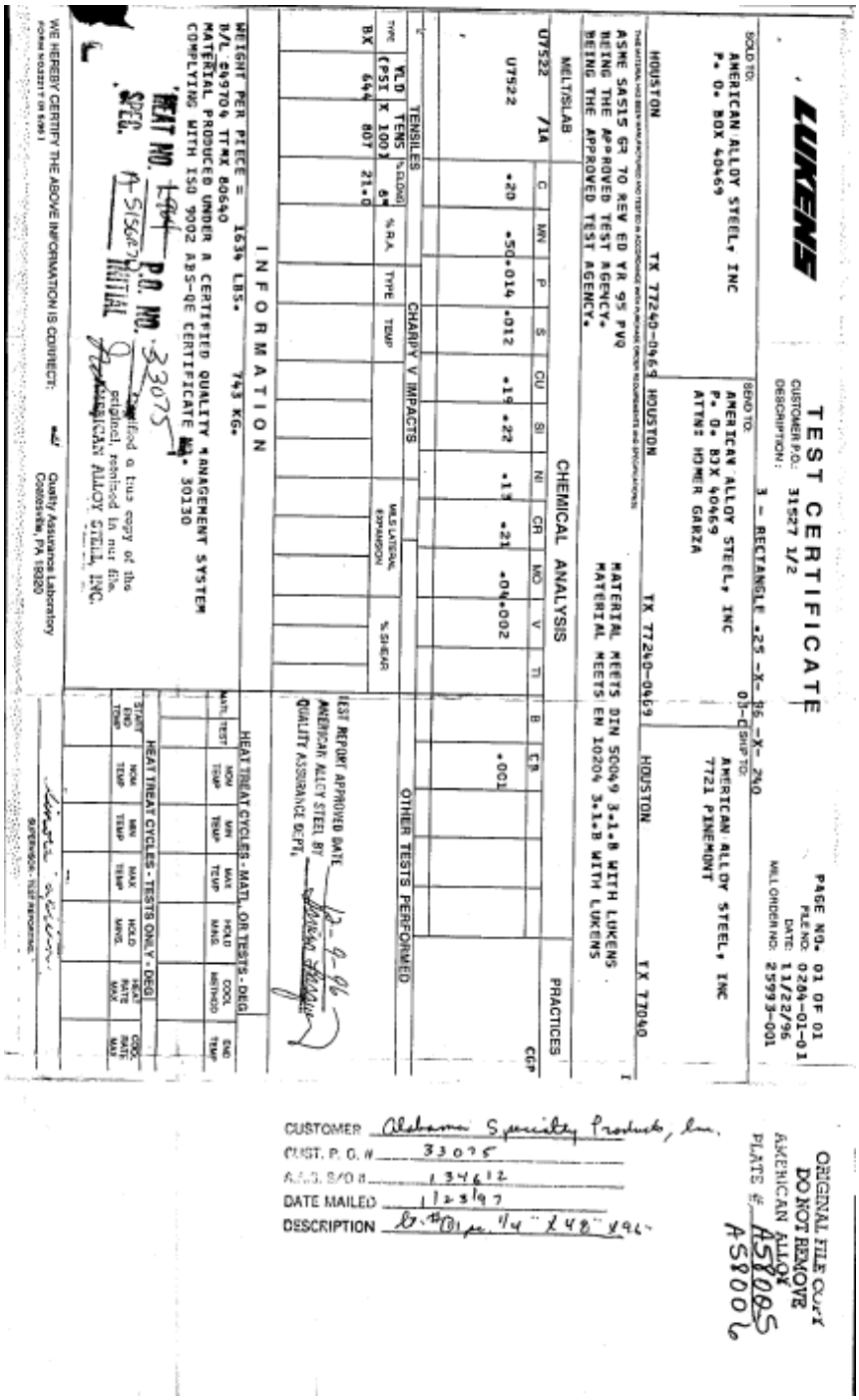

LUKENS

TEST CERTIFICATE

PAGE NO. 01 OF 01
FILE NO: 0204-01-01
DATE: 11/22/96
MILL ORDER NO: 25993-001

CUSTOMER P.O.: 31527 1/2
DESCRIPTION: 3 -- RECTANGLE .25 -X- 96 -X- 240

SOLD TO: AMERICAN ALLOY STEEL, INC
P. O. BOX 40469
HOUSTON TX 77240-0469

SEND TO: AMERICAN ALLOY STEEL, INC
P. O. BOX 40469
ATTN: HOMER GARZA
HOUSTON TX 77240-0469

DISP TO: AMERICAN ALLOY STEEL, INC
7721 PINEMONT
HOUSTON TX 77040

THE MATERIAL HAS BEEN MANUFACTURED AND TESTED IN ACCORDANCE WITH THE PURCHASE ORDER REQUIREMENTS AND SPECIFICATIONS.

ASME SA515 GR 70 REV ED YR 95 PVQ
BEING THE APPROVED TEST AGENCY.
BEING THE APPROVED TEST AGENCY.

MATERIAL MEETS DIN 50049 3.1.B WITH LUKENS .
MATERIAL MEETS EN 10204 3.1.B WITH LUKENS

MELT/SLAB

CHEMICAL ANALYSIS

	C	MN	P	S	CU	SI	NI	CR	MO	V	TI	B	CB	PRACTICES
U7522 /1A														CGP
U7522	.20	.50	.014	.012	.19	.22	.13	.21	.04	.002			.001	

TENSILES

TYPE	YLD (PSI X 1000)	TENS (PSI X 1000)	%ELONG 8"	%R.A.	TYPE
BX	64.4	80.7	21.0		

CHARPY V IMPACTS

TEMP	MILS LATERAL EXPANSION	% SHEAR

OTHER TESTS PERFORMED

TEST REPORT APPROVED DATE 12-9-96
AMERICAN ALLOY STEEL BY
QUALITY ASSURANCE DEPT.

INFORMATION

WEIGHT PER PIECE = 1634 LBS. 743 KG.
B/L 49704 TTMX 80640
MATERIAL PRODUCED UNDER A CERTIFIED QUALITY MANAGEMENT SYSTEM
COMPLYING WITH ISO 9002 ABS-QE CERTIFICATE No. 30130

HEAT NO. 1404 P.O. NO. 33075
SPEC. A-515Gr70 MATERIAL

I hereby certify a true copy of the original, retained in our file.
AMERICAN ALLOY STEEL, INC.

HEAT TREAT CYCLES - MATL. OR TESTS - DEG.

MATL TEST	START END TEMP	NOM TEMP	MIN TEMP	MAX TEMP	HOLD MINS.	COOL METHOD	END TEMP

HEAT TREAT CYCLES - TESTS ONLY - DEG.

NOM TEMP	MIN TEMP	MAX TEMP	HOLD MINS.	HEAT RATE MAX	COOL RATE MAX

WE HEREBY CERTIFY THE ABOVE INFORMATION IS CORRECT:
Quality Assurance Laboratory
Coatesville, PA 19320
SUPERVISOR - TEST PERFORMANCE

ORIGINAL FILE COPY
DO NOT REMOVE
AMERICAN ALLOY
PLATE # AS1005
AS1005

CUSTOMER Alabama Specialty Products, Inc.
CUST. P. O. # 33075
A.A.S. S/O # 134612
DATE MAILED 12/3/97
DESCRIPTION 8-#01 pc. 1/4" X 48" X 96"

Figure A 5: A515 Gr. 70 normalized plate

METALLURGICAL TEST REPORT

P.O. Box 2259
Mt. Pleasant, SC 29465

Nucor Steel - Berkeley
a division of NUCOR corporation

Phone: 843-336-6000
Sales Fax: 843-336-6150

Sold KLOCKNER NAMASCO NORCROSS
To: 500 COLONIAL CENTER PKWY.
SUITE 500
ROSWELL, GA 30076

Ship NAMASCO NORCROSS
To: 1950 MCFARLAND 400 BLVD
ALPHARETTA, GA 30004

Ship date 3/10/04
Bill of Lading # 368859
Vehicle # 1213

P/O # 8005330
Mill Order # 118147-1
Part # 58891

Gauge x Width .0630 MIN X 48.0000 MIN
Description UNS G10180
Chemistry certification only

CR
No Welds

(in percent)

Heat	C	Mn	P	S	Si	Cu	Ni	Cr	Mo	Sn	Al	V	Nb	N	Ti	B	Ca
1402657	.190	.670	.003	.001	.020	.08	.040	.030	.020	.008	.030	.003	.004	.0070	.004	.000	.001

Coil Numbers 381530.100 381530.200

All material is sold subject to the description, specifications and terms and conditions set forth on the face and reverse side of Nucor Steel - Berkeley's sales order acknowledgment.

Tensile Testing is performed in accordance with ASTM A-370 specifications. Specimen is machined to standard rectangular test configuration (Figure 3 of ASTM A-370) with a 2" gage length. Yield Strength is determined at 0.2% offset.

This material has been produced in compliance with the chemistry and established rolling practices of the ordered specification. If material is ordered to a chemical composition only and if physical testing is not a requirement of the customer's order, testing is not performed by the producer.

We hereby certify the above information is correct as contained in the records of the corporation.
Randall C Kreuse
Hot Mill Metallurgist

Ann M Gillespie
Cold Mill Metallurgist

** 100% MELTED AND MANUFACTURED IN THE USA **

MATD I.D. NO. AB825 P.O. NO. 62283
SPEC. C1018 INITIAL TB

04/05/2004 07:08 FAX

002/002

Figure A 6: A1018 Carbon Steel

AK Steel

AK Steel Corporation
Metallurgical Test Report
Coshocton Works
Coshocton, OH 43812

Page :

CUSTOMER: ADVANCED ALLOYS, INC.
1014 GRAND BLVD.
DEER PARK, NY 11729-5700

SHIPPED TO:

MILL ORDER NO: 273940-0440 010808156
PROCESSOR ORDER NO: 010808156
BUYERS ORDER NO:
PART NO: 10162
ENGLISH UNITS - PRODUCT - METRIC UNITS
.0030 NOM 36.0000 X 120.0000

COIL ID	PIECE	HEAT	PARENT COIL ID	NET WEIGHT	OUTSIDE PROCESSOR ID
666189-05-065	32	7351657	666189-05	2,295 LBS. 1,041 KG.	546375A
TOTAL COILS 1	TOTAL PIECES 32			TOTAL NET WEIGHT 2,295 LBS. 1,041 KG.	

L=Ladle Analysis of Heat P=Product Analysis of Parent Coil

CHEMICAL ANALYSIS

ID	C	MN	P	S	SI	CR	NI	MO	N	CU	TI	AL	CB	SN	TA
L 7351657	.04	.54	.023	.001	.39	15.29	4.25	.22	.032	3.40	.0020	.002	.33	.016	.001

REMARKS: THIS MATERIAL WAS MELTED AND MANUFACTURED IN THE U.S.A.
NO INTENTIONAL ADDITIONS OF MERCURY OR MERCURY COMPOUNDS, RADIUM, ALPHA SOURCE, AND LOW MELTING ALLOYS OR ELEMENTS CAPABLE OF FORMING LOW MELTING ALLOYS WERE MADE THROUGHOUT THE PROCESSING OF THIS MATERIAL.
COILED PRODUCTS CONTAIN NO WELDS

PRODUCT DESCRIPTION

CR SHT 17-4 PH STAINLESS #2D FINISH COND A SLIT EDGE * ASTM A 693 -03 (UNS S17400) FLATNESS VARIATION WILL BE 2" MAX * AMS 5604 E EX 2 LATEST REV REVIEWED BY AK. NO OBSOLETE OR CANCELED SPECS: EX 3.3 NAIVE AMS 2759 REQ; EX 3.4.1.3 NAIVE REQ; EX 3.4.2.2 PE R ASTM A 693; EX 3.6 FLATNESS VARIATION 2" MAX. EX 4.2.2 WAIVE MICROSTRUCTURE AS PERIODIC TEST * UNS-S17400 9TH EDITION * PHI 17 -4 11/03/04 WITH

PARENT COIL ID	POS (F/T)	DIR (L, T, D)	COND	% ELONG 2 INCH MEASURED	TENSILE STRENGTH (KSI)	Y.S. .2% OFFSET (KSI)	ROCKWELL HARDNESS Tail	ROCKWELL HARDNESS Front
666189-05	T	T	A.S.T.M	17.7	163.5	120.4	C 34	C 36

ADVANCED ALLOYS, INC.
1014 GRAND BLVD.
DEER PARK, NY 11729-5700

WE CERTIFY THAT THIS IS A TRUE COPY OF MILL CERTIFICATE OF TEST DATA ON MATERIAL USED TO FILL YOUR ORDER

CUSTOMER ALABAMA SPECIALTY PRODUCTS
P.O. NO. 73267 ITEM NO. 17-4PH
SIZE .062"X36"X120" QUANTITY 1PC/78#
HEAT NO. 7351657
DATE SHIPPED MARCH 29, 2006
AA ORDER NO. 74290-1

MAT'D I.D. NO. AE365 P.O. NO. 73267
SPEC. 17-4PH INITIAL JB

*** CONTINUED ON NEXT PAGE ***

Figure A 7: A693 17-4 PH stainless steel

AK Steel

AK Steel Corporation
Metallurgical Test Report
Coshocton Works
Coshocton, OH 43812

Page 2

CUSTOMER:
ADVANCED ALLOYS, INC.
1014 GRAND BLVD.
DEER PARK, NY 11729-5700

SHIP TO:

MILL ORDER NO. 271940-0440
PROCESSOR ORDER NO. 01068156
BUYERS ORDER NO. 01068156
PART NO. 10162
ENGLISH UNITS - PRODUCT - METRIC UNITS
.0630 NOM 160000 X 1200000

PARENT COIL ID	POS (F/T)	DIR (L, T, D)	COND	% ELONG 2 INCH MEASURED	TENSILE STRENGTH (KSI)	Y.S. .2% OFFSET (KSI)	ROCKWELL HARDNESS Tail	ROCKWELL HARDNESS Front				
0666189-05	T	T	H 900	10.68	205	183.3	C 46	C 46				
0666189-05	T	T	H 925	10.22	191.7	176.6	C 43	C 44				
0666189-05	T	T	H 1025	9.76	175.3	164.8	C 40	C 40				
0666189-05	T	T	H 1075	12.55	168.1	155.2	C 38	C 37				
0666189-05	T	T	H 1150	15.4	153.7	136.3	C 34	C 34				
PARENT COIL ID	POS (F/T)	DIR (L, T, D)	COND	% ELONG 2 INCH MEASURED	TENSILE STRENGTH (KSI)	Y.S. .2% OFFSET (KSI)	ROCKWELL HARDNESS Tail	ROCKWELL HARDNESS Front				
0666189-05	T		A.S.T.M	PASS								
PARENT COIL ID	POS (F/T)	DIR (L, T, D)	COND	% ELONG 2 INCH MEASURED	TENSILE STRENGTH (KSI)	Y.S. .2% OFFSET (KSI)	ROCKWELL HARDNESS Tail	ROCKWELL HARDNESS Front				
0666189-05	F	T	A.S.T.M	12.2	164.7	110.6	C 34	C 36				
0666189-05	F	T	H 900	11.8	210	189.7	C 46	C 46				
0666189-05	F	T	H 925	10.86	191.9	175.3	C 43	C 44				
0666189-05	F	T	H 1025	9.02	176.3	168.1	C 40	C 40				
0666189-05	F	T	H 1075	12.4	168.1	160.7	C 38	C 37				
0666189-05	F	T	H 1150	15.4	152.7	134.4	C 34	C 34				
PARENT COIL ID	POS (F/T)	DIR (L, T, D)	COND	BEND 180 DEG								
0666189-05	F		A.S.T.M	PASS								

THE CHEMICAL ANALYSIS AND PHYSICAL OR MECHANICAL TESTS REPORTED ABOVE ARE CORRECT AS CONTAINED IN THE RECORDS OF THE CORPORATION.

ALL TESTING IS DONE IN ACCORDANCE WITH A.S.T.M STANDARDS UNLESS OTHERWISE NOTED

AK Steel Corporation

MANUFACTURING SITE

"THIS CERTIFIED TEST REPORT HAS BEEN ORIGINATED TO A CONSUMER OF MATERIALS PURCHASED FROM AK Steel CORPORATION. TO AVOID THE POSSIBILITY OF ITS MISUSE OR OBSOLESCENCE, ANY ALTERATION OF THE REPORT TO A THIRD PARTY IT MUST BE RECERTIFIED BY AND UNDER THE NAME OF SUCH CONSUMER."

SIGNED: Date: 03/16/2006 Time: 08:33 AM

APPLICATION ENGINEER

Figure A 7 (continued): A693 17-4 PH stainless steel

INCO ALLOYS INTERNATIONAL

INCO ALLOYS INTERNATIONAL, INC.
HUNTINGTON, WEST VIRGINIA 25705

CERTIFIED MATERIAL TEST REPORT No. 93024

A M CASTLE & CO
3000 NORTH 114TH ST
WAUWATOSA WI 53222

DATE 07/22/96
PAGE 1 OF 1

QUANTITY 6844203 1
INSPECTED BY IAII

CHARGE/ORDER NO. 12220 LBS
MARK/ORDER NO. 06-86233 A/C32793

DESCRIPTION OF MATERIAL SHIPPED .0500 36.0000 COIL COIL INCONEL ALLOY 625 LCF CR SPL TOL SHEET IN COIL CR ANN

QUALITY CERTIFICATION REPRESENTATIVE

SPECIFICATIONS: HAI 320 REV F/SAE AMS 5599E MARKING WAIVED/ UNS:N06626/N06625
SAE AMS 5879B MARKING WAIVED/
ASME SB-443 1995 EDITION 95 ADDENDA GRADE 1/
ASTM B 443-93 GRADE 1.
CERTIFICATE 3.1.B AS IN EN 10 204 (CERTIFICATE DIN 50 049-3.1B)
MATERIAL MANUFACTURED IN ACCORDANCE WITH A QUALITY MANAGEMENT
SYSTEM CERTIFIED TO ISO 9002 BY ABS-QE (CERTIFICATE NO. 30125)

CHEMICAL ANALYSIS (WT. %)

HEAT#	C	MN	FE	SI	NI	CR	AL	TI
	GO	NO	NB	TA	P	N	NB+TA	
VX2652AK	0.02	0.05	3.42	<0.001	0.06	61.45	21.81	0.28 0.15
	0.10	0.10	3.54	<0.01	0.005	0.015	3.54	

MELT METHOD: ELECTROSLAG REMELT (VIM ELECTRODE)

MECHANICAL PROPERTIES

HEAT/LOT	QUANTITY	HARD NESS	GRAIN SIZE	YIELD STRENGTH .2%PSI	TENSILE PSI	%ELG 2"	R/A %	DEG F
VX2652AK GK65A 2 PCS			X 100	X 100				
ROOM TEMP-HRB -AS SHIPPED		97.0		0771	1375	48.5		
GRAIN SIZE-AS SHIPPED			11.0					

YIELD STRENGTH WAS DETERMINED USING A STRESS STRAIN CURVE

CASTLE METALS - MIL

DATE RECD 7-25-96

BEND TEST(S): SATISFACTORY

PATENT NUMBER(S)

U.S. NO. 4,761,190

REC'D FROM AM- LCS

APPROVED BY

VISUAL AND DIMENSIONAL EXAMINATION SATISFACTORY.

MATERIAL, WHEN SHIPPED, IS FREE FROM CONTAMINATION BY MERCURY, PLATIUM, ALPHA SOURCE,
AND LOW MELTING ELEMENTS.

AUTHORIZED QUALITY CERTIFICATION REPRESENTATIVES - D.B. WATSON, W.E. BOLEN, D.A. CRAZE, G.B. SIMPSON

N06625
I625

Figure A 8: B443 Alloy 625 plate

LaBarge 8/16/2006 3:13:54 PM PAGE 003/003 Fax Server

MATL. I.D. NO. AE745 P.O. NO. 23353

SPEC. A53 GRB INITIAL TK

MATERIAL TEST REPORT

Paragon Industries, Inc.
Rt.3 Box 331A
Sapulpa, Oklahoma, 74066
Phone: (918) 291-4459
Fax: (918) 291-0918

PLANT
Highway 117
6 Miles East of
Sapulpa, OK

Certificate Number 4570
Customer PO 213010 • 213020

Manufactured by Electric Resistance Weld (Type E)

Specifications
ASTM A53 06B
ASME B36.10M-1996
ASTM A500-99

Melted and Manufactured in the USA
Results relate only to items tested. Test report not to be reproduced without written approval of Quality Assurance.

Customer
LABARGE PIPE & STEEL CO.
901 N. 10TH ST. STE. 300
ST. LOUIS, MO 63101-

Product
10.75 x .500 54.79# (S)A53B/ A500B&C

Heat Number	Steel Order No.	Yield Strength Psi	Tensile Strength Psi	Elongation % in 2 inches	Test Type Orientation/Tensile	Test Condition	Gauge Width
A93918	3442	60990	72940	45.0%	Strip/Transverse/Body	As Rolled	1.5
A93919	3442	60000	73670	41.5%	Strip/Transverse/Body	As Rolled	1.5
A93920	3442	57850	73230	42.5%	Strip/Transverse/Body	As Rolled	1.5
B53997	3442	59690	74370	43.5%	Strip/Transverse/Body	As Rolled	1.5
B53998	3442	57110	71250	48.0%	Strip/Transverse/Body	As Rolled	1.5

Heat Number	Mill Control	C	MN	P	S	SI	Cr	Ni	Mo	Cu	V	Al	Ca
A93918	Heat	0.220	0.670	0.010	0.003	0.050	0.005	0.000	0.000	0.000	0.000	0.024	0.001
	Product	0.194	0.629	0.014	0.004	0.070	0.037	0.006	0.006	0.012	0.001	0.024	0.004
A93919	Heat	0.220	0.610	0.011	0.002	0.060	0.000	0.000	0.000	0.000	0.000	0.024	0.001
	Product	0.196	0.609	0.011	0.003	0.061	0.034	0.007	0.012	0.015	0.002	0.027	0.003
A93920	Heat	0.220	0.650	0.014	0.003	0.050	0.000	0.000	0.000	0.000	0.000	0.024	0.001
	Product	0.199	0.599	0.011	0.003	0.069	0.034	0.007	0.012	0.014	0.001	0.028	0.003
B53997	Heat	0.210	0.630	0.010	0.004	0.070	0.000	0.000	0.000	0.000	0.000	0.041	0.001
	Product	0.189	0.619	0.013	0.004	0.078	0.034	0.006	0.006	0.012	0.001	0.036	0.003
B53998	Heat	0.220	0.660	0.015	0.004	0.050	0.000	0.000	0.000	0.005	0.000	0.023	0.002
	Product	0.191	0.626	0.014	0.001	0.058	0.037	0.006	0.005	0.012	0.001	0.026	0.004

TEST / INSPECTION
Hydrostatic Test Psi 1850 @ 5 secs
Flattening Test YES
Ultrasonic weldline (NDT) YES .125 DH
Full Length Visual YES
Full Length Drift N/A size
Heat Treat Min. Temperature 1600 degrees

Comment
REVISED 1.9.02

We certify that the product described above has been manufactured, Sampled, Inspected and tested in accordance to the referenced specification and / or order, and is in compliance with all requirements.

QA Department

P.MTR. 0102

Figure A 9: API 5L Gr. B carbon steel pipe

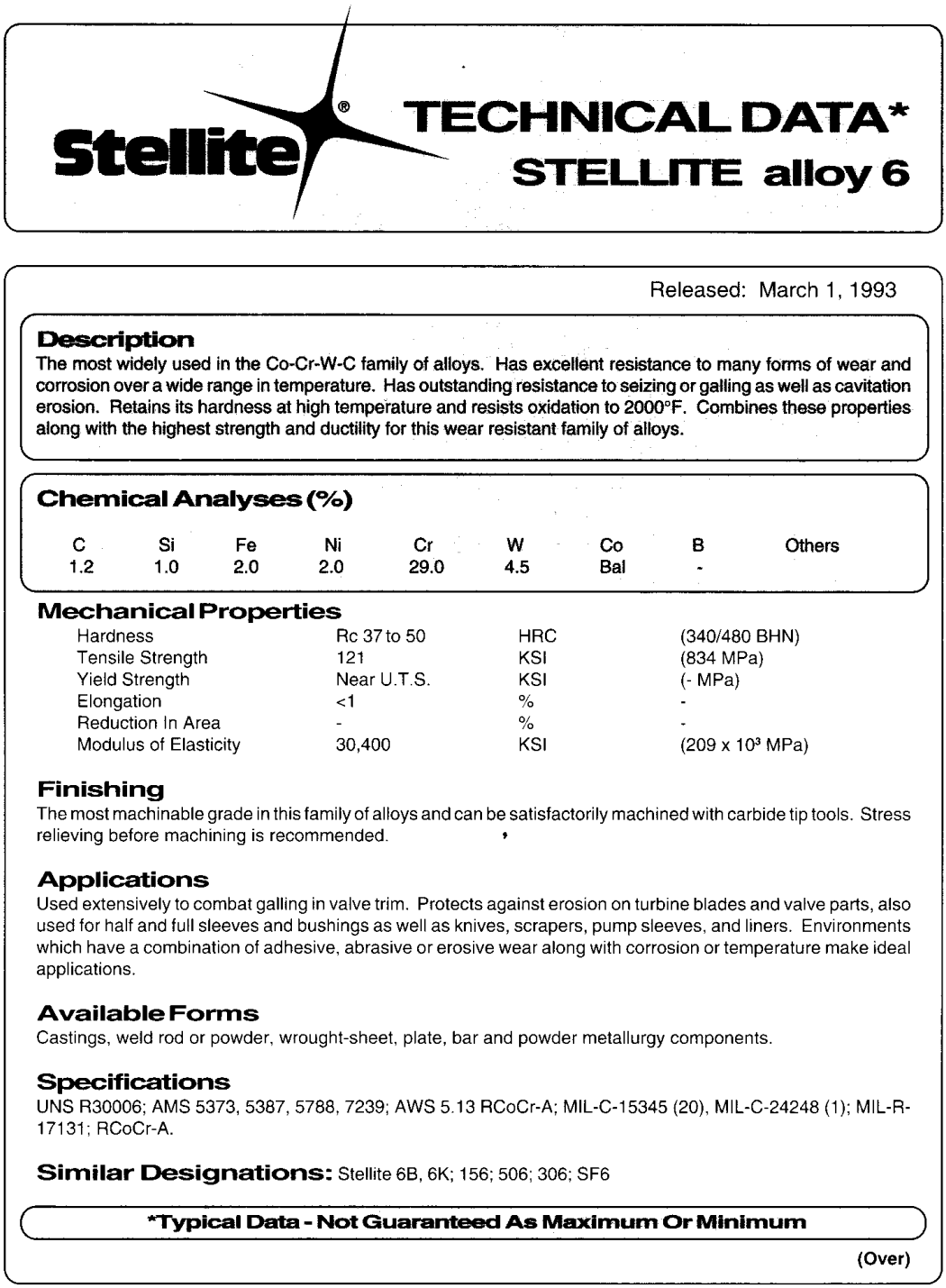

Stellite®

TECHNICAL DATA*

STELLITE alloy 6

Released: March 1, 1993

Description

The most widely used in the Co-Cr-W-C family of alloys. Has excellent resistance to many forms of wear and corrosion over a wide range in temperature. Has outstanding resistance to seizing or galling as well as cavitation erosion. Retains its hardness at high temperature and resists oxidation to 2000°F. Combines these properties along with the highest strength and ductility for this wear resistant family of alloys.

Chemical Analyses (%)

C	Si	Fe	Ni	Cr	W	Co	B	Others
1.2	1.0	2.0	2.0	29.0	4.5	Bal	-	

Mechanical Properties

Hardness	Rc 37 to 50	HRC	(340/480 BHN)
Tensile Strength	121	KSI	(834 MPa)
Yield Strength	Near U.T.S.	KSI	(- MPa)
Elongation	<1	%	-
Reduction In Area	-	%	-
Modulus of Elasticity	30,400	KSI	(209 x 10^3 MPa)

Finishing

The most machinable grade in this family of alloys and can be satisfactorily machined with carbide tip tools. Stress relieving before machining is recommended.

Applications

Used extensively to combat galling in valve trim. Protects against erosion on turbine blades and valve parts, also used for half and full sleeves and bushings as well as knives, scrapers, pump sleeves, and liners. Environments which have a combination of adhesive, abrasive or erosive wear along with corrosion or temperature make ideal applications.

Available Forms

Castings, weld rod or powder, wrought-sheet, plate, bar and powder metallurgy components.

Specifications

UNS R30006; AMS 5373, 5387, 5788, 7239; AWS 5.13 RCoCr-A; MIL-C-15345 (20), MIL-C-24248 (1); MIL-R-17131; RCoCr-A.

Similar Designations: Stellite 6B, 6K; 156; 506; 306; SF6

***Typical Data - Not Guaranteed As Maximum Or Minimum**

(Over)

Figure A 10: Stellite 6

STELLITE alloy 6

Thermal Expansion per °C x 10^6

20-100	20-300	20-500	20-600	20-700	20-800	20-1000
13.9	14.5	15.0	15.3	15.8	16.3	17.4

Thermal Conductivity	Density	Melting Range
102.7 BTU-in/ft²-hr-°F	lb/in³ .303	°F 2300 - 2475
.035 CAL-cm/cm²-sec-°C	gm/cm³ 8.38	°C 1260 - 1357

Hot Hardness: Diamond Hardness Number

20°C	100	200	300	400	500	600	700	800	900
(68)°F	(212)	(392)	(572)	(752)	(932)	(1112)	(1292)	(1472)	(1652)
410	390	356	345	334	301	235	155	138	95

Compressive Strength (Ultimate)	Impact Strength (RT)
220 KSI	Ft. Lb. 11 IZOD
1517 MPa	Joules 14.9 Un-notched

Wear

Stellite alloy 6 has excellent resistance to thermal shock and resists most types of mechanical wear especially when in combination with corrosion and/or temperature. When self-mated, it has a very low coefficient of friction of .12 and exceptional resistance to galling. It has cavitation-erosion resistance ten times that of 304 stainless steel. The material is also ten times more resistant than 1020 or 304SS in low stress abrasion and at least twice as resistant as hardened 1090 steel (Rc 55). Stellite alloy 6 is used to protect bearing surfaces in non-lubricating conditions due to its resistance to metal-to-metal wear.

Corrosion

Stellite alloy 6 has high resistance to a variety of corrosive media and excellent oxidizing resistance to about 2000°F. The material is inferior to most nickel base alloys but is resistant to oxidating acids such as acetic, formic, phosphoric and low concentration sulphuric. The alloy is not recommended for strongly reducing acids such as hydrochloric. The material behaves similar to 316SS and the extent of resistance will vary with acid concentration, temperature and contaminants making actual field tests the best method for determining suitability.

Heat Treatment

This material does not respond to thermal treatments but may be stress relieved for machining by holding at 1650°F for 4 hours and slow cool.

Stellite®

THERMADYNE®
Deloro Stellite

Executive Offices
101 South Hanley Road
St. Louis, Missouri 63105
314-721-5573
FAX: 314-862-5803

Customer Service
Deloro Stellite Inc.
P.O. Box 5300
Belleville, Ontario, Canada K8N5C4
613-968-3481
FAX: 613-966-8269

Deloro Stellite, Ltd.
Stratton St. Margaret
Swindon, Wiltshire, England SN34QA
44-(0) 793-822451
FAX:44-(0) 793-823814

Deloro Stellite GmbH
Postfach 520
Zur Bergfege 53, West Germany
49-(0) 261-80880
FAX: 49-(0) 261-808823

Form No. 461-6
Revised 2/3/93

Printed in U.S.A.

Figure A 11 (continued): Stellite 6

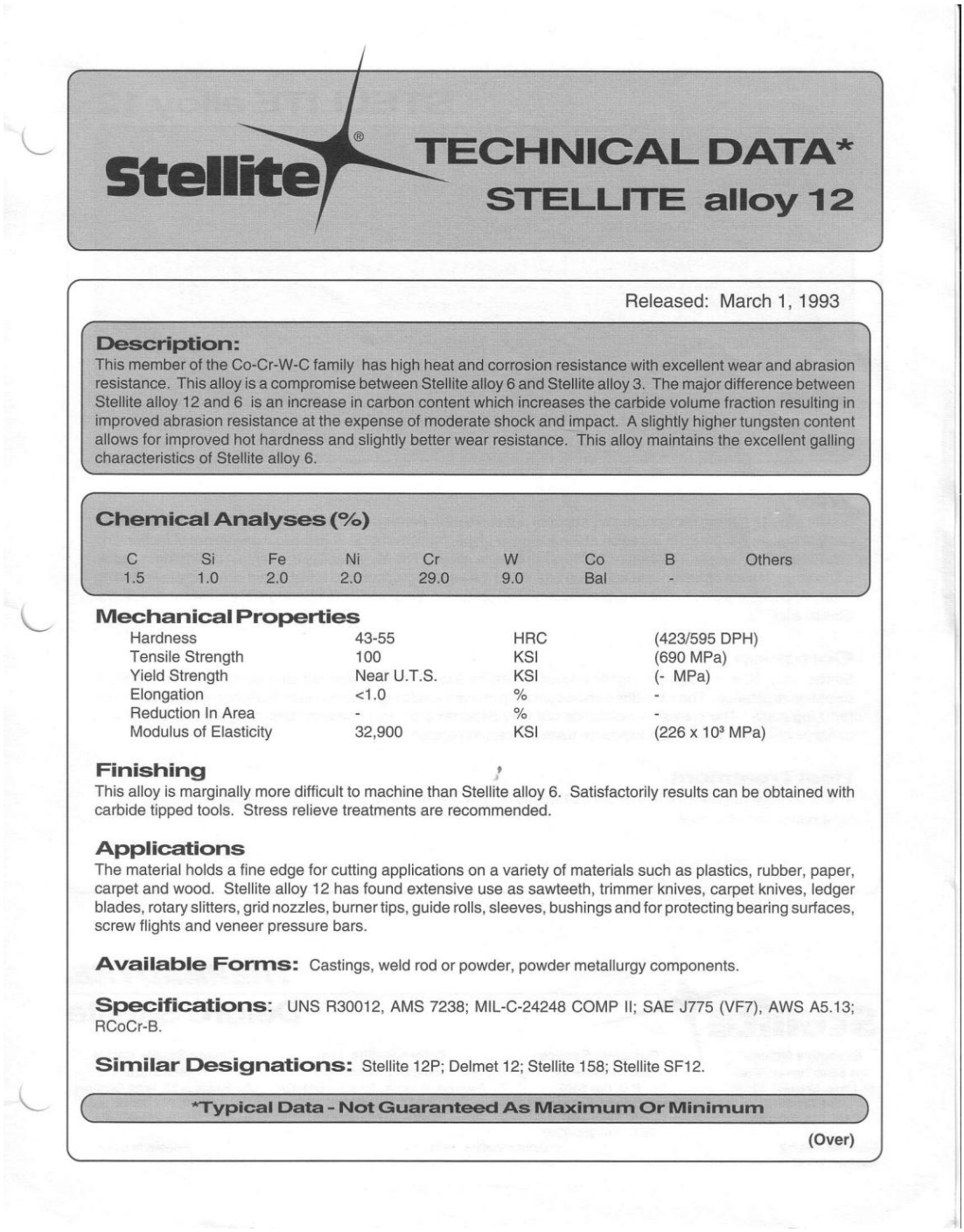

Stellite®

TECHNICAL DATA*
STELLITE alloy 12

Released: March 1, 1993

Description:
This member of the Co-Cr-W-C family has high heat and corrosion resistance with excellent wear and abrasion resistance. This alloy is a compromise between Stellite alloy 6 and Stellite alloy 3. The major difference between Stellite alloy 12 and 6 is an increase in carbon content which increases the carbide volume fraction resulting in improved abrasion resistance at the expense of moderate shock and impact. A slightly higher tungsten content allows for improved hot hardness and slightly better wear resistance. This alloy maintains the excellent galling characteristics of Stellite alloy 6.

Chemical Analyses (%)

C	Si	Fe	Ni	Cr	W	Co	B	Others
1.5	1.0	2.0	2.0	29.0	9.0	Bal	-	

Mechanical Properties

Hardness	43-55	HRC	(423/595 DPH)
Tensile Strength	100	KSI	(690 MPa)
Yield Strength	Near U.T.S.	KSI	(- MPa)
Elongation	<1.0	%	-
Reduction In Area	-	%	-
Modulus of Elasticity	32,900	KSI	(226 x 10^3 MPa)

Finishing
This alloy is marginally more difficult to machine than Stellite alloy 6. Satisfactorily results can be obtained with carbide tipped tools. Stress relieve treatments are recommended.

Applications
The material holds a fine edge for cutting applications on a variety of materials such as plastics, rubber, paper, carpet and wood. Stellite alloy 12 has found extensive use as sawteeth, trimmer knives, carpet knives, ledger blades, rotary slitters, grid nozzles, burner tips, guide rolls, sleeves, bushings and for protecting bearing surfaces, screw flights and veneer pressure bars.

Available Forms: Castings, weld rod or powder, powder metallurgy components.

Specifications: UNS R30012, AMS 7238; MIL-C-24248 COMP II; SAE J775 (VF7), AWS A5.13; RCoCr-B.

Similar Designations: Stellite 12P; Delmet 12; Stellite 158; Stellite SF12.

***Typical Data - Not Guaranteed As Maximum Or Minimum**

(Over)

Figure A 12: Stellite 12

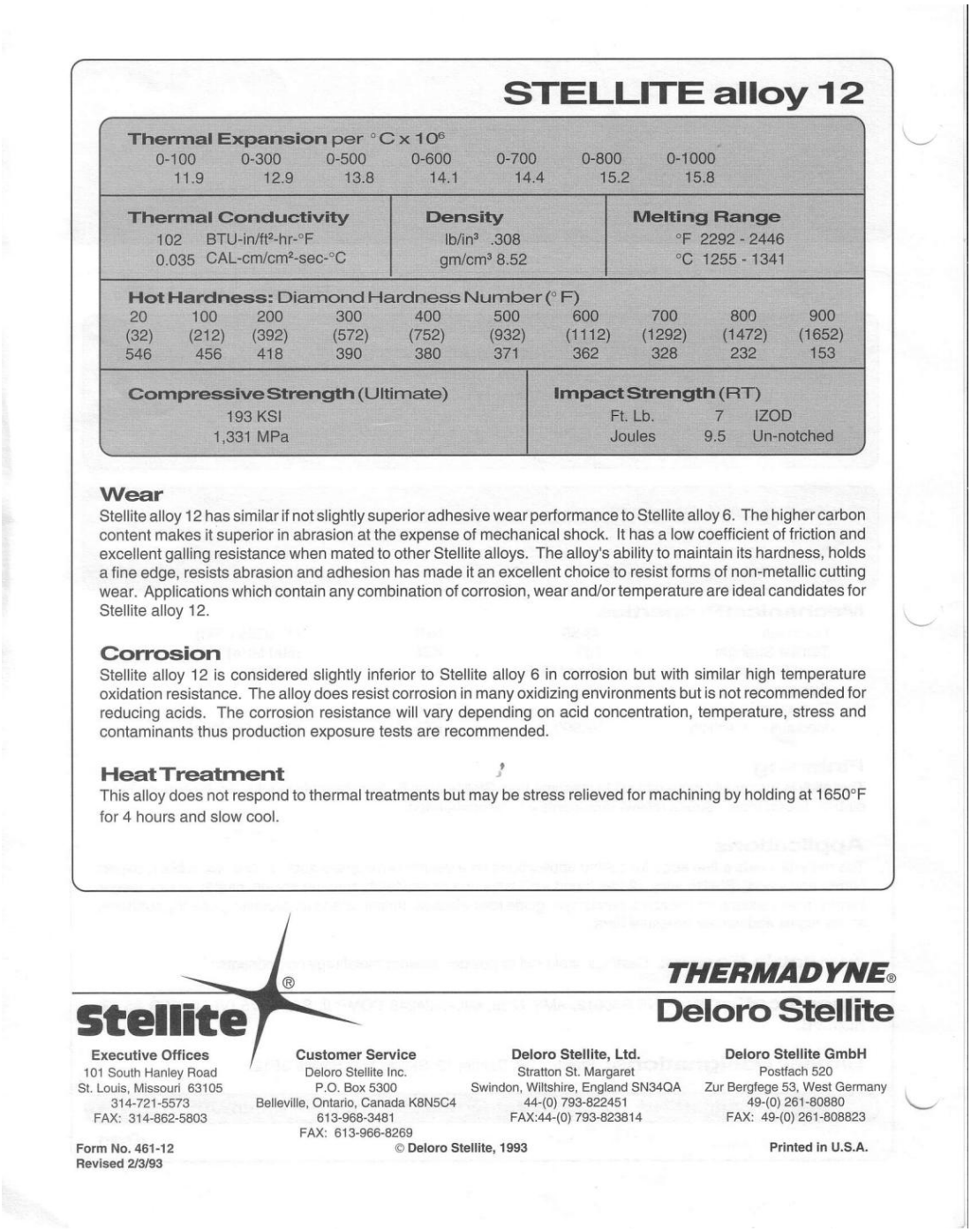

STELLITE alloy 12

Thermal Expansion per °C x 10^6

0-100	0-300	0-500	0-600	0-700	0-800	0-1000
11.9	12.9	13.8	14.1	14.4	15.2	15.8

Thermal Conductivity	Density	Melting Range
102 BTU-in/ft²-hr-°F	lb/in³ .308	°F 2292 - 2446
0.035 CAL-cm/cm²-sec-°C	gm/cm³ 8.52	°C 1255 - 1341

Hot Hardness: Diamond Hardness Number (° F)

20	100	200	300	400	500	600	700	800	900
(32)	(212)	(392)	(572)	(752)	(932)	(1112)	(1292)	(1472)	(1652)
546	456	418	390	380	371	362	328	232	153

Compressive Strength (Ultimate)	Impact Strength (RT)
193 KSI	Ft. Lb. 7 IZOD
1,331 MPa	Joules 9.5 Un-notched

Wear

Stellite alloy 12 has similar if not slightly superior adhesive wear performance to Stellite alloy 6. The higher carbon content makes it superior in abrasion at the expense of mechanical shock. It has a low coefficient of friction and excellent galling resistance when mated to other Stellite alloys. The alloy's ability to maintain its hardness, holds a fine edge, resists abrasion and adhesion has made it an excellent choice to resist forms of non-metallic cutting wear. Applications which contain any combination of corrosion, wear and/or temperature are ideal candidates for Stellite alloy 12.

Corrosion

Stellite alloy 12 is considered slightly inferior to Stellite alloy 6 in corrosion but with similar high temperature oxidation resistance. The alloy does resist corrosion in many oxidizing environments but is not recommended for reducing acids. The corrosion resistance will vary depending on acid concentration, temperature, stress and contaminants thus production exposure tests are recommended.

Heat Treatment

This alloy does not respond to thermal treatments but may be stress relieved for machining by holding at 1650°F for 4 hours and slow cool.

Stellite®

THERMADYNE®
Deloro Stellite

Executive Offices
101 South Hanley Road
St. Louis, Missouri 63105
314-721-5573
FAX: 314-862-5803

Customer Service
Deloro Stellite Inc.
P.O. Box 5300
Belleville, Ontario, Canada K8N5C4
613-968-3481
FAX: 613-966-8269

Deloro Stellite, Ltd.
Stratton St. Margaret
Swindon, Wiltshire, England SN34QA
44-(0) 793-822451
FAX:44-(0) 793-823814

Deloro Stellite GmbH
Postfach 520
Zur Bergfege 53, West Germany
49-(0) 261-80880
FAX: 49-(0) 261-808823

Form No. 461-12
Revised 2/3/93

Printed in U.S.A.

Figure A 13 (continued): Stellite 12

Product Data Sheet

Kennametal Tungsten Carbide Grade K3109

Nominal Properties

Table A 1: Ni plate Composition (Weight %)

Cobalt	12.1%
Tantalum Carbide	0.3%
Titanium Carbide	0.4% max.
Niobium Carbide	0.2% max.
Tungsten Carbide	Balance

Table A 1 (continued): Ni plate Sintered Properties

Density	14.20 g/cc
Hardness	88.0 HRA
Grain Size Range	1-8 microns

Table A 1 (continued): Ni plate Mechanical Properties

Transverse Rupture	430,000 psi
Compressive Strength	635,000 psi
Elastic Modulus	82.2 x 10^6 psi
Poisson's Ratio	0.28
Thermal Expansion*	3.3 X 10^{-6}in/in/F°

*Thermal Expansion Room to 750F

Material Data Sheet: 88% WC & 12% Cobalt Binder

APPENDIX B

Material	15°				30°				45°			
	90 m/s		130 m/s		90 m/s		130 m/s		90 m/s		130 m/s	
	Abrasive (g)	Volume Rem. (mm^3)	Abrasive (g)	Volume Rem. (mm^3)	Abrasive (g)	Volume Rem. (mm^3)	Abrasive (g)	Volume Rem. (mm^3)	Abrasive (g)	Volume Rem. (mm^3)	Abrasive (g)	Volume Rem. (mm^3)
316L	11.90	0.399	3.30	0.389	12.15	0.505	4.14	0.443	8.89	0.400	5.20	0.537
	13.09	0.462	3.96	0.418	13.37	0.572	5.18	0.567	10.16	0.451	6.24	0.644
	14.28	0.496	4.62	0.446	14.58	0.626	6.21	0.663	11.43	0.505	7.28	0.771
410	8.17	0.369	5.33	0.428	12.30	0.483	4.18	0.418	9.17	0.314	5.10	0.473
	9.33	0.375	6.39	0.563	13.53	0.532	5.23	0.516	10.48	0.356	6.12	0.567
	10.50	0.407	7.46	0.644	14.76	0.563	6.27	0.601	11.79	0.412	7.14	0.647
A105	10.20	0.345	5.33	0.443	12.30	0.484	4.18	0.389	9.17	0.339	5.10	0.474
	14.95	0.499	6.39	0.472	13.53	0.554	5.23	0.484	10.26	0.389	6.12	0.549
	16.10	0.585	12.33	0.983	14.76	0.611	6.27	0.586	10.48	0.400	7.14	0.674
A515-70	13.56	0.455	1.58	0.486	12.30	0.497	4.18	0.396	9.17	0.348	5.10	0.488
	14.69	0.492	2.37	0.516	13.53	0.534	5.23	0.503	10.48	0.385	6.12	0.589
	15.82	0.530	3.16	0.568	14.76	0.608	6.27	0.585	11.79	0.442	7.14	0.680

Table B 1: Measured Abrasive Blasted and Volume Removed for 6.9 µm particle size

Material	15°				30°				45°			
	90 m/s		130 m/s		90 m/s		130 m/s		90 m/s		130 m/s	
	Abrasive (g)	Volume Rem. (mm^3)	Abrasive (g)	Volume Rem. (mm^3)	Abrasive (g)	Volume Rem. (mm^3)	Abrasive (g)	Volume Rem. (mm^3)	Abrasive (g)	Volume Rem. (mm^3)	Abrasive (g)	Volume Rem. (mm^3)
ST 6b	12.60	0.017	3.01	0.057	12.60	0.127	6.00	0.208	11.61	0.181	6.30	0.258
	14.24	0.139	3.44	0.111	13.46	0.183	7.00	0.226	12.90	0.142	7.35	0.280
	14.70	0.030	14.48	0.148	14.70	0.141	8.00	0.268	14.19	0.171	8.40	0.318
2205	11.90	0.343	5.56	0.420	12.15	0.407	5.12	0.448	8.89	0.307	5.20	0.496
	13.09	0.371	6.95	0.529	13.37	0.444	6.40	0.592	10.16	0.344	6.24	0.583
	14.28	0.392	8.34	0.662	14.58	0.492	7.66	0.718	11.43	0.421	7.28	0.684
C1018	3.29	0.110	0.86	0.057	3.11	0.145	1.00	0.099	1.29	0.087	1.05	0.117
	3.29	0.131	0.86	0.053	3.11	0.131	1.00	0.096	1.29	0.090	1.05	0.155
	3.29	0.093	0.86	0.066	3.11	0.132	1.00	0.096	1.29	0.092	1.05	0.140
17-4PH	11.90	0.433	3.30	0.529	12.15	0.464	4.14	0.460	8.89	0.376	5.20	0.541
	13.09	0.461	3.96	0.613	13.37	0.530	5.18	0.598	10.16	0.448	6.24	0.657
	14.28	0.526	4.62	0.635	14.58	0.590	6.21	0.693	9.45	0.443	7.28	0.752

Table B 1 (continued): Measured Abrasive Blasted and Volume Removed for 6.9 µm particle size

Material	15°				30°				45°			
	90 m/s		130 m/s		90 m/s		130 m/s		90 m/s		130 m/s	
	Abrasive (g)	Volume Rem. (mm^3)	Abrasive (g)	Volume Rem. (mm^3)	Abrasive (g)	Volume Rem. (mm^3)	Abrasive (g)	Volume Rem. (mm^3)	Abrasive (g)	Volume Rem. (mm^3)	Abrasive (g)	Volume Rem. (mm^3)
A53-B	11.90	0.416	3.30	0.365	12.15	0.510	4.14	0.434	8.89	0.333	6.10	0.459
	13.09	0.431	3.96	0.407	13.37	0.532	5.18	0.594	10.16	0.420	7.32	0.589
	14.28	0.484	4.62	0.503	14.58	0.573	6.21	0.667	11.43	0.399	8.54	0.673
I-625	13.14	0.234	9.06	0.573	12.42	0.410	4.18	0.417	9.17	0.324	5.10	0.501
	14.24	0.266	10.36	0.676	13.46	0.436	5.23	0.519	10.48	0.360	6.12	0.591
	15.33	0.306	11.655	0.778	14.49	0.476	6.27	0.565	11.79	0.408	7.14	0.670
ST 12	12.48	0.043	16.12	0.100	12.84	0.077	6.00	0.084	11.61	0.045	6.30	0.100
	13.44	0.043	17.36	0.102	13.91	0.085	7.00	0.092	12.90	0.054	7.35	0.114
	14.40	0.044	18.60	0.107	14.98	0.090	8.00	0.096	14.19	0.062	8.40	0.119

Table B 1 (continued): Measured Abrasive Blasted and Volume Removed for 6.9 µm particle size

***NOTE: Tungsten carbide does not appear in these tables. Dwell times of 400 s at all angles were tested, with no measurable volume removed for both particle velocities.**

Material	60°				75°				90°			
	90 m/s		130 m/s		90 m/s		130 m/s		90 m/s		130 m/s	
	Abrasive (g)	Volume Rem. (mm^3)	Abrasive (g)	Volume Rem. (mm^3)	Abrasive (g)	Volume Rem. (mm^3)	Abrasive (g)	Volume Rem. (mm^3)	Abrasive (g)	Volume Rem. (mm^3)	Abrasive (g)	Volume Rem. (mm^3)
316L	9.07	0.360	4.32	0.433	8.89	0.257	3.30	0.305	7.49	0.223	2.93	0.235
	10.36	0.407	5.40	0.544	10.16	0.287	4.40	0.405	8.56	0.263	3.90	0.311
	11.66	0.465	6.48	0.663	11.43	0.326	5.50	0.507	9.63	0.283	4.88	0.393
410	7.77	0.274	4.00	2.93	8.37	0.186	3.30	0.235	8.54	0.175	3.00	0.183
	8.88	0.328	5.00	3.90	9.56	0.226	4.40	0.305	9.76	0.210	4.00	0.247
	9.99	0.352	6.00	4.88	10.76	0.261	5.50	0.374	10.98	0.225	5.00	0.302
A105	7.77	0.293	3.52	0.348	8.37	0.186	3.30	0.237	8.54	0.184	3.00	0.177
	8.88	0.315	5.00	0.445	9.56	0.215	4.40	0.272	9.76	0.196	4.00	0.244
	9.99	0.377	6.00	0.544	11.25	0.246	5.50	0.375	10.98	0.216	5.00	0.297
A515-70	7.77	0.242	4.00	0.396	8.37	0.205	3.30	0.235	8.54	0.186	3.00	0.188
	8.88	0.278	5.00	0.482	9.56	0.233	4.40	0.299	9.76	0.191	4.00	0.250
	9.99	0.316	6.00	0.563	10.76	0.261	5.50	0.384	10.98	0.214	5.00	0.299

Table B 2: Measured Abrasive Blasted and Volume Removed for 30.4 µm particle size

Material	60°				75°				90°			
	90 m/s		130 m/s		90 m/s		130 m/s		90 m/s		130 m/s	
	Abrasive (g)	Volume Rem. (mm^3)	Abrasive (g)	Volume Rem. (mm^3)	Abrasive (g)	Volume Rem. (mm^3)	Abrasive (g)	Volume Rem. (mm^3)	Abrasive (g)	Volume Rem. (mm^3)	Abrasive (g)	Volume Rem. (mm^3)
ST 6b	10.13	0.128	6.39	0.207	8.64	0.100	6.54	0.222	11.25	0.072	4.85	0.167
	11.25	0.137	7.46	0.269	9.60	0.100	7.63	0.254	12.50	0.096	5.82	0.175
	12.38	0.140	11.7	0.431	10.56	0.117	13.2	0.421	13.75	0.102	6.79	0.207
2205	9.07	0.333	4.32	0.396	4.20	0.176	3.30	0.284	6.44	0.213	2.93	0.211
	10.36	0.390	5.40	0.493	5.25	0.221	4.40	0.363	7.36	0.252	3.90	0.272
	11.66	0.434	6.48	0.591	6.30	0.254	5.50	0.456	8.28	0.274	4.88	0.314
C1018	1.13	0.067	1.07	0.132	0.96	0.062	0.55	0.077	1.25	0.076	0.49	0.086
	1.13	0.063	1.07	0.139	0.96	0.063	0.55	0.084	1.25	0.080	0.49	0.082
	1.13	0.064	1.07	0.130	0.96	0.064	0.55	0.076	1.25	0.071	0.49	0.085
17-4PH	9.07	0.344	4.32	0.425	8.89	0.228	3.30	0.288	7.49	0.216	2.93	0.217
	10.36	0.432	5.40	0.550	10.16	0.289	4.40	0.389	8.56	0.228	3.90	0.287
	11.66	0.460	6.48	0.639	11.43	0.328	5.50	0.471	9.63	0.269	4.88	0.367

Table B 2 (continued): Measured Abrasive Blasted and Volume Removed for 30.4 µm particle size

Material	60°				75°				90°			
	90 m/s		130 m/s		90 m/s		130 m/s		90 m/s		130 m/s	
	Abrasive (g)	Volume Rem. (mm^3)	Abrasive (g)	Volume Rem. (mm^3)	Abrasive (g)	Volume Rem. (mm^3)	Abrasive (g)	Volume Rem. (mm^3)	Abrasive (g)	Volume Rem. (mm^3)	Abrasive (g)	Volume Rem. (mm^3)
A53-B	9.07	0.332	4.32	0.361	8.89	0.194	3.30	0.236	7.49	0.154	2.93	0.183
	10.36	0.344	5.40	0.472	10.16	0.226	4.40	0.321	8.56	0.175	3.90	0.251
	11.66	0.391	6.48	0.570	11.43	0.257	5.50	0.408	9.63	0.193	4.88	0.281
I-625	7.77	0.288	4.00	0.380	7.70	0.282	3.30	0.286	8.54	0.201	3.00	0.231
	8.88	0.333	5.00	0.471	8.80	0.332	4.40	0.369	9.76	0.248	4.00	0.317
	9.99	0.374	6.00	0.563	9.90	0.369	5.50	0.452	10.98	0.289	5.00	0.372
ST 12	10.13	0.070	6.39	0.090	8.64	0.065	6.54	0.101	11.25	0.031	4.85	0.073
	11.25	0.077	7.46	0.105	9.60	0.068	7.63	0.118	12.50	0.053	5.82	0.097
	12.38	0.080	8.52	0.122	10.56	0.070	8.72	0.121	13.75	0.034	6.79	0.087

***NOTE: Tungsten carbide does not appear in these tables. Dwell times of 400 s at all angles were tested, with no measurable volume removed for both particle velocities.**

Table B 2(continued): Measured Abrasive Blasted and Volume Removed for 30.4 µm particle size

APPENDIX C

Table C 1: Erosion resistance rankings of 11 candidate materials for high particle velocity (130 $m.s^{-1}$) erosion rate experiments for large particle size (30.4 μm). Erosion rates under each condition are volumetric.

Material	Impingement Angle(α), and Erosion Rate (g/g)					
	15°	**30°**	**45°**	**60°**	**75°**	**90°**
A1018 Carbon Steel Nickel Plating	0.068	0.097	0.131	0.125	0.145	0.174
A240 Type 2205 Duplex Stainless Steel Plate	0.087	0.105	0.09	0.09	0.078	0.052
17-4 PH Stainless Steel Plate	0.08	0.112	0.101	0.099	0.083	0.077
Type 316L Stainless Steel	0.043	0.106	0.112	0.106	0.091	0.08
A53 Gr. B Steel	0.104	0.112	0.087	0.097	0.077	0.05
A240 Type 410 Stainless Steel Plate	0.101	0.087	0.085	0.088	0.062	0.059
A105 Carbon Steel Forging	0.08	0.094	0.098	0.077	0.062	0.06
A515-70- A515 Gr. 70 Norm. Plate	0.038	0.09	0.094	0.083	0.068	0.055
Alloy 625 Plate	0.079	0.07	0.082	0.091	0.075	0.07
Solid Stellite 6b	0.002	0.029	0.028	0.041	0.029	0.02
Solid Stellite 12	0.002	0.005	0.009	0.015	0.008	0.007

Table C 2: Erosion resistance rankings of 11 candidate materials for high particle velocity (90 m.s^{-1}) erosion rate experiments for large particle size (30.4 μm). Erosion rates under each condition are volumetric.

Material	Impingement Angle(α), and Erosion Rate (g/g)					
	15°	**30°**	**45°**	**60°**	**75°**	**90°**
A1018 Carbon Steel Nickel Plating	0.034	0.044	0.07	0.057	0.066	0.06
A240 Type 2205 Duplex Stainless Steel Plate	0.02	0.034	0.044	0.038	0.037	0.033
17-4 PH Stainless Steel Plate	0.039	0.052	0.054	0.044	0.039	0.024
Type 316L Stainless Steel	0.04	0.049	0.041	0.04	0.027	0.027
A53 Gr. B Steel	0.028	0.026	0.025	0.022	0.025	0.017
A240 Type 410 Stainless Steel Plate	0.016	0.032	0.037	0.035	0.031	0.02
A105 Carbon Steel Forging	0.038	0.051	0.046	0.038	0.02	0.013
A515-70- A515 Gr. 70 Norm. Plate	0.033	0.045	0.035	0.033	0.023	0.011
Alloy 625 Plate	0.032	0.032	0.032	0.038	0.039	0.035
Solid Stellite 6b	0.004	0.007	0.006	0.005	0.009	0.011
Solid Stellite 12	0.0006	0.006	0.006	0.004	0.002	0.001

Table C 2: Erosion resistance rankings of 11 candidate materials for high particle velocity (130 m.s^{-1}) erosion rate experiments for large particle size (6.9 µm). Erosion rates under each condition are volumetric.

Material	Impingement Angle(α), and Erosion Rate (g/g)					
	15°	**30°**	**45°**	**60°**	**75°**	**90°**
A1018 Carbon Steel Nickel Plating	0.302	0.351	0.28	0.216	0.231	0.256
A240 Type 2205 Duplex Stainless Steel Plate	0.091	0.179	0.164	0.109	0.085	0.069
17-4 PH Stainless Steel Plate	0.145	0.195	0.159	0.135	0.07	0.087
Type 316L Stainless Steel	0.181	0.216	0.167	0.141	0.114	0.098
A53 Gr. B Steel	0.211	0.172	0.13	0.113	0.131	0.126
A240 Type 410 Stainless Steel Plate	0.314	0.199	0.147	0.15	0.101	0.079
A105 Carbon Steel Forging	0.147	0.167	0.137	0.105	0.077	0.076
A515-70- A515 Gr. 70 Norm. Plate	0.193	0.213	0.112	0.111	0.104	0.079
Alloy 625 Plate	0.184	0.18	0.152	0.116	0.079	0.104
Solid Stellite 6b	0.034	0.046	0.166	0.098	0.09	0.083
Solid Stellite 12	0.032	0.011	0.023	0.02	0.024	0.018

Table C 3: Erosion resistance rankings of 11candidate materials for high particle velocity (90 m.s^{-1}) erosion rate experiments for large particle size (6.9 µm). Erosion rates under each condition are volumetric.

Material	Impingement Angle(α), and Erosion Rate (g/g)					
	15°	**30°**	**45°**	**60°**	**75°**	**90°**
A1018 Carbon Steel Nickel Plating	0.128	0.137	0.163	0.103	0.08	0.071
A240 Type 2205 Duplex Stainless Steel Plate	0.077	0.083	0.068	0.066	0.035	0.035
17-4 PH Stainless Steel Plate	0.057	0.09	0.063	0.049	0.034	0.035
Type 316L Stainless Steel	0.084	0.08	0.064	0.054	0.025	0.032
A53 Gr. B Steel	0.077	0.066	0.093	0.054	0.027	0.022
A240 Type 410 Stainless Steel Plate	0.053	0.054	0.057	0.054	0.029	0.026
A105 Carbon Steel Forging	0.072	0.079	0.059	0.049	0.029	0.026
A515-70- A515 Gr. 70 Norm. Plate	0.065	0.061	0.06	0.042	0.035	0.033
Alloy 625 Plate	0.057	0.08	0.067	0.054	0.041	0.03
Solid Stellite 6b	0.013	0.015	0.019	0.017	0.014	0.018
Solid Stellite 12	0.001	0.009	0.006	0.001	0.003	0.006

APPENDIX D

Table D 1: Erosion resistance rankings of 11 candidate materials for high particle velocity (130 $m.s^{-1}$) erosion rate experiments for large particle size (30.4 μm). Erosion rates under each condition are dimensionless.

Material	Impingement Angle(α), and Erosion Rate (g/g)					
	15°	**30°**	**45°**	**60°**	**75°**	**90°**
A1018 Carbon Steel Nickel Plating	0.000605	0.000864	0.001161	0.001113	0.001285	0.001545
A240 Type 2205 Duplex Stainless Steel Plate	0.000686	0.000833	0.000714	0.000712	0.000616	0.000417
17-4 PH Stainless Steel Plate	0.000621	0.000872	0.000787	0.000769	0.000645	0.000596
Type 316L Stainless Steel	0.000340	0.000848	0.000894	0.000848	0.000732	0.000642
A53 Gr. B Steel	0.000817	0.000882	0.000687	0.000759	0.000610	0.000396
A240 Type 410 Stainless Steel Plate	0.000786	0.000677	0.000661	0.000685	0.000487	0.000462
A105 Carbon Steel Forging	0.000629	0.000740	0.000770	0.000611	0.000494	0.000474
A515-70- A515 Gr. 70 Norm. Plate	0.000300	0.000710	0.000739	0.000655	0.000534	0.000435
Alloy 625 Plate	0.000677	0.000595	0.000699	0.000774	0.000634	0.000593
Solid Stellite 6b	0.000022	0.000249	0.000239	0.000344	0.000251	0.000174
Solid Stellite 12	0.000023	0.000049	0.000077	0.000128	0.000074	0.000060

Table D 2: Erosion resistance rankings of 11 candidate materials for high particle velocity (90 m.s^{-1}) erosion rate experiments for large particle size (30.4 μm). Erosion rates under each condition are dimensionless.

Material	Impingement Angle(α), and Erosion Rate (g/g)					
	15°	30°	45°	60°	75°	90°
A1018 Carbon Steel Nickel Plating	0.000301	0.000389	0.000618	0.000510	0.000583	0.000537
A240 Type 2205 Duplex Stainless Steel Plate	0.000162	0.000274	0.000353	0.000306	0.000294	0.000262
17-4 PH Stainless Steel Plate	0.000304	0.000402	0.000418	0.000345	0.000304	0.000191
Type 316L Stainless Steel	0.000325	0.000396	0.000328	0.000323	0.000215	0.000221
A53 Gr. B Steel	0.000223	0.000203	0.000202	0.000178	0.000196	0.00014
A240 Type 410 Stainless Steel Plate	0.000128	0.000252	0.000290	0.000273	0.000242	0.000158
A105 Carbon Steel Forging	0.000300	0.000404	0.000395	0.000299	0.000163	0.000104
A515-70- A515 Gr. 70 Norm. Plate	0.000261	0.000353	0.000282	0.000262	0.000182	0.000088
Alloy 625 Plate	0.000277	0.000270	0.000270	0.000324	0.000333	0.000301
Solid Stellite 6b	0.000034	0.000059	0.000056	0.000045	0.000076	0.000098
Solid Stellite 12	0.000005	0.000051	0.000056	0.000038	0.000022	0.000010

Table D 3: Erosion resistance rankings of 11candidate materials for high particle velocity (130 m.s^{-1}) erosion rate experiments for large particle size (6.9 µm). Erosion rates under each condition are dimensionless.

Material	Impingement Angle(α), and Erosion Rate (g/g)					
	15°	**30°**	**45°**	**60°**	**75°**	**90°**
A1018 Carbon Steel Nickel Plating	0.002687	0.003114	0.002484	0.001915	0.001894	0.002410
A240 Type 2205 Duplex Stainless Steel Plate	0.000899	0.001503	0.001260	0.001013	0.000778	0.000626
17-4 PH Stainless Steel Plate	0.001392	0.001500	0.001288	0.001013	0.000509	0.000677
Type 316L Stainless Steel	0.002094	0.001732	0.001333	0.001170	0.000970	0.000752
A53 Gr. B Steel	0.001528	0.001461	0.001262	0.001127	0.000930	0.000992
A240 Type 410 Stainless Steel Plate	0.002026	0.001337	0.001234	0.001056	0.000787	0.000688
A105 Carbon Steel Forging	0.001276	0.001405	0.001162	0.001032	0.000731	0.000601
A515-70- A515 Gr. 70 Norm. Plate	0.001491	0.001497	0.001150	0.000990	0.000793	0.000592
Alloy 625 Plate	0.001544	0.001536	0.001315	0.001155	0.000884	0.000870
Solid Stellite 6b	0.000281	0.000393	0.001398	0.000827	0.000755	0.000446
Solid Stellite 12	0.000163	0.000225	0.000218	0.000285	0.000242	0.000205

Table D 4: Erosion resistance rankings of 11 candidate materials for high particle velocity (90 m.s^{-1}) erosion rate experiments for large particle size (6.9 µm). Erosion rates under each condition are dimensionless.

Material	Impingement Angle(α), and Erosion Rate (g/g)					
	15°	30°	45°	60°	75°	90°
A1018 Carbon Steel Nickel Plating	0.001139	0.001216	0.001449	0.000912	0.000715	0.000712
A240 Type 2205 Duplex Stainless Steel Plate	0.000635	0.000687	0.000566	0.000522	0.000417	0.000311
17-4 PH Stainless Steel Plate	0.000693	0.000653	0.000482	0.000439	0.000331	0.000299
Type 316L Stainless Steel	0.000618	0.000667	0.000558	0.000491	0.000271	0.000255
A53 Gr. B Steel	0.000586	0.000585	0.000607	0.000392	0.000279	0.000231
A240 Type 410 Stainless Steel Plate	0.000476	0.000482	0.000418	0.000400	0.000254	0.000219
A105 Carbon Steel Forging	0.000645	0.000525	0.000540	0.000496	0.000285	0.000237
A515-70- A515 Gr. 70 Norm. Plate	0.000633	0.000561	0.000489	0.000387	0.000258	0.000242
Alloy 625 Plate	0.000879	0.000714	0.000654	0.000439	0.000392	0.000311
Solid Stellite 6b	0.000030	0.000133	0.000159	0.000142	0.000039	0.000152
Solid Stellite 12	0.000016	0.000066	0.000088	0.000056	0.000070	0.000055

APPENDIX E

Table E 1: Normalized Erosion resistance rankings of 11 candidate materials for high particle velocity (130 $m.s^{-1}$) erosion rate experiments for large particle size (30.4 μm). Erosion rates under each condition are dimensionless.

Material	Impingement Angle(α), and Erosion Rate (g/g)					
	15°	30°	45°	60°	75°	90°
A1018 Carbon Steel Nickel Plating	0.391586	0.559223	0.751456	0.72038835	0.831391586	1
A240 Type 2205 Duplex Stainless Steel Plate	1.645084	1.997602	1.71223	1.707434053	1.477218225	1
17-4 PH Stainless Steel Plate	1.041946	1.463087	1.32047	1.290268456	1.082214765	1
Type 316L Stainless Steel	0.529595	1.320872	1.392523	1.320872274	1.140186916	1
A53 Gr. B Steel	2.063131	2.227273	1.734848	1.916666667	1.54040404	1
A240 Type 410 Stainless Steel Plate	1.701299	1.465368	1.430736	1.482683983	1.054112554	1
A105 Carbon Steel Forging	1.327004	1.561181	1.624473	1.289029536	1.042194093	1
A515-70-A515 Gr. 70 Norm. Plate	0.689655	1.632184	1.698851	1.505747126	1.227586207	1
Alloy 625 Plate	1.141653	1.003373	1.178752	1.305227656	1.069139966	1
Solid Stellite 6b	0.126437	1.431034	1.373563	1.977011494	1.442528736	1
Solid Stellite 12	0.383333	0.816667	1.283333	2.133333333	1.233333333	1

Table E 2: Normalized Erosion resistance rankings of 11 candidate materials for high particle velocity (90 m.s^{-1}) erosion rate experiments for large particle size (30.4 μm). Erosion rates under each condition are dimensionless.

Material	Impingement Angle(α), and Erosion Rate (g/g)					
	15°	**30°**	**45°**	**60°**	**75°**	**90°**
A1018 Carbon Steel Nickel Plating	0.560521	0.724395	1.150838	0.94972067	1.08566108	1
A240 Type 2205 Duplex Stainless Steel Plate	0.618321	1.045802	1.347328	1.167938931	1.122137405	1
17-4 PH Stainless Steel Plate	1.591623	2.104712	2.188482	1.806282723	1.591623037	1
Type 316L Stainless Steel	1.470588	1.791855	1.484163	1.461538462	0.972850679	1
A53 Gr. B Steel	1.592857	1.45	1.442857	1.271428571	1.4	1
A240 Type 410 Stainless Steel Plate	0.810127	1.594937	1.835443	1.727848101	1.53164557	1
A105 Carbon Steel Forging	2.884615	3.884615	3.798077	2.875	1.567307692	1
A515-70-A515 Gr. 70 Norm. Plate	2.965909	4.011364	3.204545	2.977272727	2.068181818	1
Alloy 625 Plate	0.920266	0.89701	0.89701	1.07641196	1.106312292	1
Solid Stellite 6b	0.346939	0.602041	0.571429	0.459183673	0.775510204	1
Solid Stellite 12	0.53	5.1	5.6	3.8	2.2	1

Table E 3: Normalized Erosion resistance rankings of 11 candidate materials for high particle velocity (130 $m.s^{-1}$) erosion rate experiments for large particle size (6.9 μm). Erosion rates under each condition are dimensionless.

Material	Impingement Angle(α), and Erosion Rate (g/g)					
	15°	30°	45°	60°	75°	90°
A1018 Carbon Steel Nickel Plating	1.114938	1.292116	1.030705	0.794605809	0.785892116	1
A240 Type 2205 Duplex Stainless Steel Plate	1.436102	2.400958	2.01278	1.618210863	1.242811502	1
17-4 PH Stainless Steel Plate	2.05613	2.215657	1.902511	1.496307238	0.751846381	1
Type 316L Stainless Steel	2.784574	2.303191	1.772606	1.555851064	1.289893617	1
A53 Gr. B Steel	1.540323	1.472782	1.272177	1.13608871	0.9375	1
A240 Type 410 Stainless Steel Plate	2.944767	1.943314	1.793605	1.534883721	1.143895349	1
A105 Carbon Steel Forging	2.123128	2.33777	1.933444	1.717138103	1.216306156	1
A515-70-A515 Gr. 70 Norm. Plate	2.518581	2.528716	1.942568	1.672297297	1.339527027	1
Alloy 625 Plate	1.774713	1.765517	1.511494	1.327586207	1.016091954	1
Solid Stellite 6b	0.630045	0.881166	3.134529	1.85426009	1.692825112	1
Solid Stellite 12	0.795122	1.097561	1.063415	1.390243902	1.180487805	1

Table E 4: Normalized Erosion resistance rankings of 11 candidate materials for high particle velocity (90 m.s^{-1}) erosion rate experiments for large particle size (6.9 µm). Erosion rates under each condition are dimensionless.

Material	Impingement Angle (α), and Erosion Rate (g/g)					
	15°	30°	45°	60°	75°	90°
A1018 Carbon Steel Nickel Plating	1.599719	1.707865	2.035112	1.280898876	1.004213483	1
A240 Type 2205 Duplex Stainless Steel Plate	2.041801	2.209003	1.819936	1.678456592	1.340836013	1
17-4 PH Stainless Steel Plate	2.317726	2.183946	1.61204	1.468227425	1.107023411	1
Type 316L Stainless Steel	2.423529	2.615686	2.188235	1.925490196	1.062745098	1
A53 Gr. B Steel	2.536797	2.532468	2.627706	1.696969697	1.207792208	1
A240 Type 410 Stainless Steel Plate	2.173516	2.200913	1.908676	1.826484018	1.159817352	1
A105 Carbon Steel Forging	2.721519	2.21519	2.278481	2.092827004	1.202531646	1
A515-70-A515 Gr. 70 Norm. Plate	2.615702	2.318182	2.020661	1.599173554	1.066115702	1
Alloy 625 Plate	2.826367	2.29582	2.102894	1.411575563	1.260450161	1
Solid Stellite 6b	0.197368	0.875	1.046053	0.934210526	0.256578947	1
Solid Stellite 12	0.290909	1.2	1.6	1.018181818	1.272727273	1

APPENDIX F

Table F 1: Constraints on curve fit parameters n1, n2, n3 and C

Parameter	Lower Bound	Upper Bound
n1	0	2
n2	0	1
n3	1.5	3
C	$-\infty$	∞

Table F 2: Constraints on curve fit parameter HV for 11 candidate materials and the measured as-received HV

Material	As-received (HV)	Lower bound (HV)	Upper bound (HV)
A1018 Carbon Steel With Ni-Plate	746	671.4	1119
A240 Type 2205 Duplex Stainless Steel Plate	262	235.8	393
17-4 PH Stainless Steel Plate	352	316.8	528
Type 316L Stainless Steel	164	147.6	246
A53 Gr. B Steel	157	141.3	235.5
A240 Type 410 Stainless Steel Plate	152	136.8	228
A105 Carbon Steel Forging	161	144.9	241.5
A515 Gr. 70 Norm. Plate	164	147.6	246
Alloy 625 Plate	227	204.3	340.5
Solid Stellite 6b	492	324.9	541.5
Solid Stellite 12	361	324.9	738

Table F 3: Coefficients and Exponents of 11 candidate materials generated by Oka model for all experimental conditions

Materials:	Exponents and Coefficients.	Experiment Cond.			
		V= 130(m/s), d= 30.4 (µm)	**V= 90 (m/s), d= 30.4(µm)**	**V= 130(m/s), d= 6.9 (µm)**	**V= 90 (m/s), d= 6.9 (µm)**
A1018 Carbon Steel Nickel Plating	n_1	0.8249	0.5824	$2.23*10^{-14}$	0.03551
	n_2	$1.31*10^{-10}$	0.03245	0.007469	0.0925
	HV	671.4	671.4	671.4	676.4
	n_3	2.25	2.25	2.25	2.25
	C	$2.51*10^{-8}$	2.15*10-08	$4.11*10^{-8}$	$2.81*10^{-8}$
A240 Type 2205 Duplex Stainless Steel Plate	**Exponents and Coefficients.**	**V= 130(m/s), d= 30.4 (µm)**	**V= 90 (m/s), d= 30.4(µm)**	**V= 130(m/s), d= 6.9 (µm)**	**V= 90 (m/s), d= 6.9 (µm)**
	n_1	0.2123	0.6421	0.3412	0.03944
	n_2	0.1458	0.09528	0.1895	0.1544
	HV	361.7	235.8	235.8	235.8
	n_3	2.25	2.25	2.25	2.25
	C	$7.31*10^{-9}$	$1.04*10^{-8}$	$1.08*10^{-8}$	$1.24*10^{-8}$
17-4 PH Stainless Steel Plate	**Exponents and Coefficients.**	**V= 130(m/s), d= 30.4 (µm)**	**V= 90 (m/s), d= 30.4(µm)**	**V= 130(m/s), d= 6.9 (µm)**	**V= 90 (m/s), d= 6.9 (µm)**
	n_1	0.2348	0.414	$8.66*10^{-12}$	$2.04*10^{-10}$
	n_2	0.08135	0.1948	0.1325	0.1362
	HV	316.8	316.8	316.8	316.8
	n_3	2.25	2.25	2.25	2.25
	C	$1.04*10^{-8}$	$7.63*10^{-9}$	$1.15*10^{-8}$	$1.17*10^{-8}$

Table F 4 (continued): Coefficients and Exponents of 11 candidate materials generated by Oka model for all experimental conditions

	Exponents and Coefficients.	**V= 130(m/s), d= 30.4 (µm)**	**V= 90 (m/s), d= 30.4(µm)**	**V= 130(m/s), d= 6.9 (µm)**	**V= 90 (m/s), d= 6.9 (µm)**
Type 316L Stainless Steel	n_1	0.7888	0.09149	$3.48*10^{-10}$	0.06197
	n_2	0.1506	0.1213	0.1917	0.214
	HV	147.6	147.6	147.6	147.6
	n_3	2.25	2.25	2.25	2.25
	C	$1.11*10^{-8}$	$8.73*10^{-9}$	$1.30*10^{-8}$	$1.01*10^{-8}$
A53 Gr. B Steel	**Exponents and Coefficients.**	**V= 130(m/s), d= 30.4 (µm)**	**V= 90 (m/s), d= 30.4(µm)**	**V= 130(m/s), d= 6.9 (µm)**	**V= 90 (m/s), d= 6.9 (µm)**
	n_1	0.1151	$1.63*10^{-5}$	$1.41*10^{-12}$	0.08795
	n_2	0.1718	0.08603	0.07721	0.2301
	HV	235.5	235.5	141.3	141.3
	n_3	2.25	2.25	2.25	2.25
	C	$6.97*10^{-9}$	$5.66*10^{-9}$	$1.70*10^{-8}$	$9.15*10^{-9}$
A240 Type 410 Stainless Steel Plate	**Exponents and Coefficients.**	**V= 130(m/s), d= 30.4 (µm)**	**V= 90 (m/s), d= 30.4(µm)**	**V= 130(m/s), d= 6.9 (µm)**	**V= 90 (m/s), d= 6.9 (µm)**
	n_1	$2.34*10^{-13}$	0.9445	$1.46*10^{-10}$	0.052769
	n_2	0.104	0.2493	0.1889	0.1862
	HV	136.8	136.8	136.8	136.8
	n_3	2.25	2.25	2.25	2.25
	C	$8.05*10^{-9}$	$6.33*10^{-9}$	$1.18*10^{-8}$	$8.72*10^{-9}$

Table F 5 (continued): Coefficients and Exponents of 11candidate materials generated by Oka model for all experimental conditions

	Exponents and Coefficients.	**V= 130(m/s), d= 30.4 (µm)**	**V= 90 (m/s), d= 30.4(µm)**	**V= 130(m/s), d= 6.9 (µm)**	**V= 90 (m/s), d= 6.9 (µm)**
A105 Carbon Steel Forging	n_1	0.1684	0.5499	0.06657	$2.33*10^{-8}$
	n_2	0.1192	0.3941	0.1879	0.2075
	HV	144.9	144.9	144.9	144.9
	n_3	2.25	2.25	2.25	2.25
	C	$8.19*10^{-9}$	$4.13*10^{-9}$	$1.05*10^{-8}$	$9.47*10^{-9}$
A515 Gr. 70 Norm. Plate	**Exponents and Coefficients.**	**V= 130(m/s), d= 30.4 (µm)**	**V= 90 (m/s), d= 30.4(µm)**	**V= 130(m/s), d= 6.9 (µm)**	**V= 90 (m/s), d= 6.9 (µm)**
	n_1	0.7841	0.4605	$1.20*10^{-10}$	$4.63*10^{-10}$
	n_2	0.2005	0.3596	0.1954	0.1911
	HV	147.6	174.9	147.6	147.6
	n_3	2.25	2.25	2.25	2.25
	C	$7.50*10^{-9}$	$3.53*10^{-9}$	$1.03*10^{-8}$	$9.51*10^{-9}$
Alloy 625 Plate	**Exponents and Coefficients.**	**V= 130(m/s), d= 30.4 (µm)**	**V= 90 (m/s), d= 30.4 (µm)**	**V= 130(m/s), d= 6.9 (µm)**	**V= 90 (m/s), d= 6.9 (µm)**
	n_1	0.133	0.1366	$6.98*10^{-1}$	$3.44*10^{-10}$
	n_2	0.04549	0.008698	0.1076	0.1833
	HV	340.5	340.5	204.3	204.3
	n_3	2.25	2.25	2.25	2.25
	C	$1.04*10^{-8}$	$1.22*10^{-8}$	$1.50*10^{-8}$	$1.22*10^{-8}$

Table F 6 (continued): Coefficients and Exponents of 11 candidate materials generated by Oka model for all experimental conditions

Solid Stellite 6b	**Exponents and Coefficients.**	**V= 130(m/s), d= 30.4 (µm)**	**V= 90 (m/s), d= 30.4(µm)**	**V= 130(m/s), d= 6.9 (µm)**	**V= 90 (m/s), d= 6.9 (µm)**
	n_1	1.491	1.102	1.541	0.6084
	n_2	0.215	$3.43*10^{-10}$	0.2837	$2.41*10^{-114}$
	HV	324.9	472.1	324.9	324.9
	n_3	2.25	2.25	2.25	2.25
	C	$3.02*10^{-9}$	$3.35*10^{-9}$	$7.68*10^{-9}$	$5.40*10^{-9}$
Solid Stellite 12	**Exponents and Coefficients.**	**V= 130(m/s), d= 30.4 (µm)**	**V= 90 (m/s), d= 30.4(µm)**	**V= 130(m/s), d= 6.9 (µm)**	**V= 90 (m/s), d= 6.9 (µm)**
	n_1	1.688	1.336	0.4776	0.8891
	n_2	0.1965	0.4239	0.06508	0.1112
	HV	442.8	442.8	735.8	442.8
	n_3	2.25	2.25	2.25	2.25
	C	$1.02*10^{-9}$	$3.91*10^{-10}$	$3.59*10^{-9}$	$2.18*10^{-9}$

REFERENCES

[1] Y. I. Oka, K. Okamura, and T. Yoshida, "Particle Estimation of erosion damage caused by Solid Particle Impact, Part 1: Effects of Impact Parameters on a Predictive Equation", Wear, 259 (2005), pp. 95-101.

[2] R.M. Baldwin, "Black powder in the gas industry sources, characteristics and treatment", GMRC, Report No TA97-4, May (1998).

[3] R.M. Baldwin, "Black powder control starts locally, works back to source", pipeline and gas industry, April (1999), pp. 81-87.

[4] R.M. Baldwin, "Black powder problem will yield to understanding, planning", pipeline and gas industry, March (1999), pp. 109-112.

[5] Tsochatzidis, N.A. and Maroullis, K.E.: "Methods help remove black powder from gas pipelines" Oil and gas journal, (2007), vol.105, No. 10, pp. 52-58.

[6] S. Arrington, "Pipeline debris removal requires extensive planning" pipeline and gas Journal, November (2006), pp. 61-62.

[7] M. Ali, and M Trablusi, Black powder in sales-gas transmission pipelines, The Journal of Pipeline Engineering, Pipelines Department, Saudi Aramco, Dharan, Saudi Arabia, vol. 3, n(8), (2007), pp. 245-250.

[8] ASTM Standard G76-07, "Standard Test Method for Conducting Erosion Tests by Solid Particle Impingement Using Gas Jets,", ASTM International (2007), West Conshohocken, PA, www.astm.org.

[9] M.S. Abdelmounam, Saudi Aramco Journal of technology, fall 2007 pp. 3-8.

[10] J. Smart "Movement of Black powder in gas pipeline by", John smart consulting

Engineer Houston, Pipeline and Gas Journal, October (2007), pp. 82-85.

[11] F.F. Lyle, "Carbon Dioxide/Hydrogen Sulphide Corrosion under wet low flow gas pipeline conditions in the presence of bicarbonate, chloride and Oxygen", PRCI final report PR-15-9313, (1997).

[12] J. Smart, and R. Winters., "Black powder migration in gas pipeline and associated problems" The pipeline pigging and integrity management conference. Feb. (2008), Houston, Texas pp. 3.

[13] I.M. Hutchings, R.E. Winter, "Particle Erosion of Ductile Metals: A Mechanism of Material Removal", Wear, (1974), 27/1, pp. 121-128.

[14] D.S. Park, "Micro-grooving of glass using micro-abrasive jet machining", Journal of Materials Processing Tech., vol. 146, (2004), pp. 234-240.

[15] R. Balasubramaniam, J. Krishnan, and N. Ramakrishnan, "A study on the shape of the surface generated by abrasive jet machining", Journal of Materials Processing Tech., vol. 121, (2002), pp. 102-106.

[16] P. Tangestanian, M. Papini, and J.K. Spelt, "Starch media blast cleaning of artificially aged paint films", Wear, vol. 248, Mar. (2001), pg. 128-139.

[17] A. Raykowski, "Blast cleaning of gas turbine components: deposit removal and substrate deformation," Wear, vol. 249, (2001), pp. 126-131.

[18] G.I. Parslow, "Investigation of solid particle erosion in components of complex geometry", Wear, vol. 233-235, Dec. (1999), pp. 737-745.

[19] A. Forder, M. Thew, and D. Harrison, “A numerical investigation of solid particle erosion experienced within oilfield control valves”, Wear, vol. 216, Apr. (1998), pp. 184-193.

[20] B. McLaury, “Solid particle erosion in long radius elbows and straight pipes”, Proceedings - SPE Annual Technical Conference and Exhibition, vol. Pi, (1997), pp. 977-986.

[21] A. Campos-Amezcua, “Numerical investigation of the solid particle erosion rate in a steam turbine nozzle,” Applied Thermal Engineering, vol. 27, Oct. (2007), pp. 2394-2403.

[22] X. Chen, “Foreign object damage on the leading edge of a thin blade”, Mechanics of Materials, vol. 37, Apr. (2005), pp. 447-457.

[23] M. Gustavsson and A.E. Almstedt, “Two-fluid modeling of cooling-tube erosion in a fluidized bed”, Chemical Engineering Science, vol. 55, Feb. (2000), pp. 867-879.

[24] I. Finnie, “Erosion of surfaces by solid particles”, Wear, vol. 3, (1960), pp. 87-103.

[25] S. Dhar, “Erosion mechanisms due to impact of single angular particles”, Wear, vol. 258, (2005), pp. 567-579.

[26] G. Sundararajan, “A comprehensive model for the solid particle erosion of ductile materials”, Wear, vol. 149, (1991), pp. 111-127.

[27] R. Winter and I. Hutchings, “Solid particle erosion studies using single angular particles”, Wear, vol. 29, Aug. 1974, pp. 181-194.

[28] I. Hutchings and R. Winter, “Particle Erosion of Ductile Metals: A Mechanism of Material Removal”, Wear, vol. 27, (1974), pp. 121-128.

[29] Nelson, and Stacy A.; Baker, Michael J.; Deans, William F.”, The effect of surface roughness on the erosion of mild steel**”,** *IPC*, vol. 1, (2004), pp. 803-810.

[30] Q. Chen, and D. Y. Li, "Computer simulation of solid particle erosion", Wear vol. 254, Issues 3-4, Feb. 2003, pp. 203-210.

[31] D.J. O'Flynn, "A model to predict the solid particle erosion rate of metals and its assessment using heat-treated steels", Wear, vol. 248, Mar. (2001), pp. 162-177.

[32] Z. Feng and A. Ball, "The erosion of four materials using seven erodents towards an understanding", Wear, vol. 233-235, Dec. (1999), pp. 674-684.

[33] Y. Oka and T. Yoshida, "Practical estimation of erosion damage caused by solid particle impact: Part 2: Mechanical properties of materials directly associated with erosion damage", Wear, vol. 259, (2005), pp. 102-109.

[34] Y. Ballout, J. Mathis, and J. Talia, "Solid particle erosion mechanism in glass", Wear, vol. 196, (1996), pp. 263-269.

[35] A. Levy, "Solid Particle Erosion and Erosion-Corrosion of Materials", ASM International, (1995).

[36] A.V. Levy and G. Hickey, "Liquid-solid particle slurry erosion of steels", Wear, vol. 117, (1987), pp. 129-46.

[37] I. M. Hutchings, "Thermal Effects in the Erosion of Ductile Metals", Wear, vol.131, (1989) pp. 105–121.

[38] R. E. Winter and I. M. Hutchings, "The Role of Adiabatic Shear in Solid Particle Erosion", Wear, vol.34, (1975), pp. 141- 148.

[39] M.A. Meyers, Dynamic Behavior of Materials, Wiley-Interscience, (1994).

[40] S. Malkin, “Correlation Between Solid Particle Erosion of Metals and Their Melting Energies:, Wear, vol. 68, (1981), pp. 391-396.

[41] J.F. Molinari, and M. Ortiz, “A study of solid-particle erosion of metallic targets”, International Journal of Impact Engineering, vol. 27, (2002), pp. 347–358.

[42] I. Finnie, “Erosion of surfaces by solid particles”, Wear, vol. 3, (1960), pp. 87-103.

[43] J.G.A. Bitter, “A study of erosion phenomena, Part I”, Wear, vol. 6, (1963), pp. 5-21.

[44] J.G.A. Bitter, “A study of erosion phenomena: Part II”, Wear, vol. 6, (1963), pp. 169-190.

[45] I. Hutchings, “Deformation of metal surfaces by the oblique impact of square plates”, International Journal of Mechanical Sciences, vol. 19, (1977), pp. 45-52.

[46] T. Christman and G. Shewmon, “Erosion of a Strong Aluminum Alloy”, Wear, vol. 52, 1979, pp. 57-70.

[47] M. Liebhard and A. Levy, “The effect of erodent particle characteristics on the erosion of metals”, Wear, vol. 151, Dec. (1991), pp. 381-390.

[48] T. Deng, M.S. Bingley, and M.S.A. Bradley, “The influence of particle rotation on the solid particle erosion rate of metals”, Wear, vol. 256, Jun. (2004), pp. 1037-1049.

[49] G.W. Stachowiak, “Numerical characterization of wear particles morphology and angularity of particles and surfaces”, Tribology International, vol. 31, (1998), pp. 139-157.

[50] D.V. De Pellegrin and G.W. Stachowiak, “Assessing the role of particle shape and scale in abrasion using sharpness analysis': Part I. Technique development”, Wear, vol. 253, Nov. (2002), pp. 1016-1025.

[51] G.R. Desale, B.K. Gandhi, and S. Jain, “Slurry erosion of ductile materials under normal impact condition”, Wear, vol. 264, Feb. (2008), pp. 322-330,

[52] I. Finnie, J. Wolak, and Y. Kabil, “Erosion of metals by solid particles”, Journal of Materials, vol. 2, 1967, pp. 682-700.

[53] M. Dundar, O.T. Inal, and J. Stringer, “Erratum to "The effect of particle size on the erosion of a ductile material at the low particle size limit"Wear, vol. 240, May. (2000), pp. 235-244.

[54] A. Misra, and I. Finnie, “On the size effect in abrasive and erosive wear”, Wear, vol. 65, (1981), pp. 359–373.

[55] A.N.J. Stevenson, and I.M. Hutchings, “Scaling laws for particle velocity in the gas-blast erosion test”, Wear, vol. 181-183, Feb. (1995), pp. 56-62.

[56] G. Sheldon, “Similarities and Differences in the Erosion Behavior of Materials”, ASME, vol. 92, (1970), pp. 619-626.

[57] J. Goodwin, W. Sage, and G. Tilly, “Study of Erosion by Solid Particles”, Proc. Inst Mechanical Eengineering, vol.15, (1968), pp. 279-292.

[58] G. Tilly, “Erosion Caused by Airborne Particles,” Wear, vol. 14, 1969, pg. 63-79.

[59] T. Christman and P. Shewman, “Adiabatic shear localization and erosion of strong aluminum alloys”, Wear, vol. 54, (1979), pp. 145-155.

[60] F. Jianren, “Numerical simulation of tube erosion by particle impaction”, Wear, vol. 142, Feb. 1991, pp. 171-184.

[61] M. Papini and J.K. Spelt, “Impact of rigid angular particles with fully-plastic targets Part II: Parametric study of erosion phenomena”, International Journal of Mechanical Sciences, vol. 42, May. (2000), pp. 1007-1025.

[62] F. Jianren, “Numerical simulation of tube erosion by particle impaction”, Wear, vol. 142, Feb. (1991), pp. 171-184.

[63] A.V. Levy, “Platelet mechanism of erosion of ductile metals”, Wear, vol. 108, (1986), pp. 1-21.

[64] P.H. Shipway and I.M. Hutchings, “A method for optimizing the particle flux in erosion testing with a gas-blast apparatus”, Wear, vol. 174, May. (1994), pp. 169-175.

[65] N. Shafiei; H. Getu; A. Sadeghian; and M. Papini, “Computer simulation of developing abrasive jet machined profiles including particle interference”, Journal of Materials Processing Tech. May (2009), vol. 209 (9), pp. 4366-4378.

[66] T. Burzynski; and M. Papini, “Analytical model of particle interference effects in divergent erosive jets”, Tribology International March (2010), vol. 43 (3), pp. 554-567.

[67] D. Ciampini, J.K. Spelt, and M. Papini, “Simulation of interference effects in particle streams following impact with a flat surface Part I. Theory and analysis”, Wear 254, (2003) , pp. 237–249.

[68] D. Ciampini, J.K. Spelt, and M. Papini, “Simulation of interference effects in particle streams following impact with a flat surface Part II. Parametric study and implications for erosion testing and blast cleaning”, Wear 254 (2003), pp. 250–264.

[69] L.R. Pope and C. W. Ward, Manual on test sieving methods: guideline for establishing sieve analysis procedures, prepared by ASTM Committee E29, Ed., ASTM, West Conshohocken, PA, (1998), ISBN 0-8031-2495-3.

[70] A. Ghobeity, T. Krajac, T. Burzynski, M. Papini, and J. K. Spelt, "Surface evolution models in abrasive jet micromachining", Wear, 264 (3-4), (2008), pp. -198.

[71] D. Tabor, The Hardness of Metals, Oxford University Press, (2000).

[72] G.W. Stachowiak and A.W. Batchelor, Engineering Tribology, 3rd ed., Elsevier Butterworth-Heinemann, (2005), pp. 518-519.

[73] Matlab software manual, R2009b, "Least square method in Curve fitting", MathWorks inc., Version# 7.9.0.529.

[74] F. Jianren et al., "Numerical simulation of tube erosion by particle impaction." Wear, vol. 142, Feb. (1991), pp. 171-18.

[75] Habib, H.M. Badr, S.A.M. Said, R. Ben-Mansour, and S.S Al-Anizi, Solid-particle erosion in the tube end of the tube sheet of a shell-and-tube heat exchanger, International Journal for Numerical Methods in Fluids, March (2006), vol. 50, n (8), pp. 885-909.

[76] Jong Jip Kim, and Seong Khil Park, Solid Particle erosion of SiC and SiC-TiB_2 composite hot-pressed with Y_2O_3, Wear, vol. 222, (1998), pp. 114-119.

[77] B.F. Levin, K.S. Vecchio, J.N. Dupont, and A.R. Marder, "Modeling Solid-Particle Erosion of Ductile Alloys", Journal of Metallurgical and Materials Transactions A, vol. 30A, July 1999-1763.

[78] ASTM standard B912-02, "Standard Specification for Passivation of Stainless Steels Using Electropolishing", ASTM International (2007), West Conshohocken, PA, www.astm.org.

[79] ASTM standard A380-06, "Standard Practice for Cleaning, Descaling, and Passivation of Stainless Steel Parts, Equipment, and Systems", ASTM International (2007), West Conshohocken, PA, www.astm.org.

[80] Jong Jip Kim, and Seong Khil Park, "Solid particle erosion of SiC and SiC–TiB_2 composite hot-pressed with Y_2O_3",Wear, vol. 222, Issue 2, November (1998), pp. 114-119.

[81] S. Soderberg, S. Hogmark, H. Swahn, "Mechanisms of material removal during erosion of a stainless steel", *ASLE Transactions*, v 26, n 2, 161-72, April 1983.